

MIXING AND TURBULENCE IN FLOATING FLEXIBLE PHOTOBIOREACTORS

KÉLAN NAIDOO



UNIVERSITY OF TM
KWAZULU-NATAL

INYUVESI
YAKWAZULU-NATALI



Submitted in partial fulfilment of the requirements for the degree of
Master of Sciences in Engineering

School of Civil Engineering, Surveying, and Construction
College of Agriculture, Engineering and Science
University of KwaZulu-Natal
Durban
2021

DECLARATION

I Kèlan Naidoo confirm that the information presented in the following report is of my own work and has not been plagiarised in any way. Where the intellectual property of other authors and researchers has been used, it has congruently been referenced and acknowledged. This research was done under the supervision of Professor Derek D. Stretch and Dr. Justin J. Pringle at the school of engineering, University of KwaZulu-Natal, Howard College. I further acknowledge the rules and regulations of the University of KwaZulu-Natal and accept the consequences of any transgressions of my own doing.

Signed:  _____

Date: 03/12/21

Signed: Kèlan Naidoo – 213533950

As the candidate's supervisor I agree to the submission of this research:

Signed:  _____

Date: 03/12/21

Professor Derek D. Stretch

Signed:  _____

Date: 03/12/21

Dr. Justin J. Pringle

ACKNOWLEDGEMENTS

I would like to thank my parents: Visvanathan Naidoo and Rozanne Naidoo for constantly inspiring me and granting me the opportunities that I've been given. I will forever be grateful for the knowledge, strength, and guidance you have given me unconditionally. I want to thank Rebekah-Leigh Naidoo for always motivating me to do great things; and Aishwarya Bedessy for being my pillar of strength and guidance. I would like to thank Dr. Justin Pringle for his invaluable mentorship and assistance in making this research possible; and Professor Derek Stretch for his supervision and trust in giving me the opportunity to better my academic career.

ABSTRACT

Renewable energy initiatives aim to advance global efforts toward a sustainable bio-economy. The power generation industry is the most crucial sector requiring strategic planning to achieve economic and environmental sustainability. Biodiesel production utilising microalgae as a feedstock yields a $\pm 400\%$ larger production range compared to traditional feedstocks. Floating flexible photobioreactors (FPBs) aim to provide large-scale microalgae enclosures and promote biofuel production's commercial application. FPBs are placed off-shore, where they naturally accelerate microalgae growth by harnessing wave energy, sunlight, waste carbon dioxide and wastewater discharge (as a nutrient source). Microalgae production requires explicit physical and chemical conditions to achieve optimal growth rates. In this study, a physical FPB model is constructed within a laboratory wave flume where the change in the internal fluid motion within the FPB is observed under an idealised wave pressure constriction. Under the influence of an idealised wave, the flexible tube experiences a reduction and expansion in its cross-sectional area, which deforms the internal fluid flow. The fluid's flow structure is analysed using particle image velocimetry (PIV). PIVlab was used to analyse the data. The fluid moves backwards (or towards constriction) when placed under direct tube constriction; however, under unrestricted tube expansion, the fluid is propelled forward in the original direction of the idealised wave, in the form of a bulge wave. Relative to the constriction, the fluid moves negatively on the left-hand side of the peak and positively on the right-hand side. Regions of strong shear in which there was a rapid change in the velocity were identified as potential mixing zones.

TABLE OF CONTENTS

DECLARATION.....	i
ACKNOWLEDGEMENTS	ii
ABSTRACT	iii
LIST OF FIGURES.....	v
LIST OF TABLES.....	viii
NOMENCLATURE:	viii
ACRONYMS:	ix
CHAPTER 1: INTRODUCTION.....	1
1.1 PROJECT DESCRIPTION:.....	1
1.2 RESEARCH BACKGROUND:.....	3
1.3 RESEARCH QUESTIONS:	3
1.4 AIMS:.....	4
1.5 OBJECTIVES:.....	4
1.6 RESEARCH OUTLINE:.....	4
1.7 RESEARCH APPROACH:	4
CHAPTER 2: LITERATURE REVIEW.....	6
2.1 BIOENERGY THROUGH MICROALGAE EXTRACTION.....	6
2.2 OFFSHORE MEMBRANE ENCLOSURES FOR GROWING ALGAE.....	7
2.3 BIOFUEL PRODUCTION FROM MICROALGAE BIOMASS	9
2.4 MIXING OF MICROALGAE CELLS	10
2.5 PERISTALTIC MOTION IN FLEXIBLE PHOTOBIOREACTORS.....	13
2.6 MEASURING FLUID-STRUCTURE INTERACTIONS	17
2.7 WAVE SPECTRUM DECOMPOSITION	20
2.8 PARTICLE IMAGE VELOCIMETRY	21
CHAPTER 3: METHODOLOGY:.....	29
3.1 FLOATING FLEXIBLE BIOREACTOR MODEL	37
3.2 NON-INVASIVE OPTICAL TESTING.....	40
3.3 OPTIMAL FIELD OF VIEW CALIBRATION	43
3.4 PIV PARTICLE PARAMETERS	44
CHAPTER 4: RESULTS AND DISCUSSION:.....	51
CHAPTER 5: REVIEW AND CONCLUSIONS	87

5.1 FUTURE APPROACH AND RECOMMENDATIONS:.....	89
REFERENCES:.....	90
APPENDIX A: VELOCITY CROSS-SECTIONS.....	96
APPENDIX B: SHEAR RATE.....	106
APPENDIX C: STRAIN RATE.....	116
APPENDIX D: VORTICITY.....	126

LIST OF FIGURES

Figure 2-1: Microalgae produces more oil per acre in comparison to its rival terrestrial plants (Trent 2012).....	6
Figure 2-2: Conceptualized OMEGA scheme including aquaculture housing, solar panels and wind turbines (Trent 2012).....	8
Figure 2-3: Simulated growth pattern in a bioreactor with a deep optical depth (0.5m) under constant illumination for a 15 day period (Flynn 2019).....	11
Figure 2-4: Simulated growth pattern in a bioreactor with a shallow optical depth (0.05m) under constant illumination for a 15 day period (Flynn 2019).....	11
Figure 2-5: Relating $P - P_e$ to cross-sectional area. Where P is the internal pressure and P_e is the external pressure (Grotberg and Jensen 2004).....	14
Figure 2-6: Geometry for the two-dimensional peristaltic flow on a cylindrical tube wall (Muthu, Kumar, and Chandra 2001).....	16
Figure 2-7: PIVlab workflow and implemented features (Thielicke and Stamhuis 2014).....	22
Figure 2-8: Correlation matrices of DCC and DFT investigate a single particle displacement (Thielicke and Stamhuis 2014).....	24
Figure 2-9: The window deformation technique for two passes (Thielicke and Stamhuis 2014).....	25
Figure 2-10: Gaussian 3 point fit. One-dimensional Gaussian function (solid line), Integer distribution of the correlation matrix (dots) (Thielicke and Stamhuis 2014).....	26
Figure 2-11: Performance of popular interpolation methods (Thielicke and Stamhuis 2014).....	28

Figure 3-1: Piston paddle wave generator indicating the volume displaced by the paddle in relation to the volume of water in the crest (Dean and Dalrymple 1991)	29
Figure 3-2: Piston paddle wave generator laboratory setup	30
Figure 3-3: Non-Dimensional Relationship of H/S vs Kph for the piston paddle wave generator.....	30
Figure 3-4: Python graphic interface tracking the pixel co-ordinates of the centroid of the buoy mechanism.	31
Figure 3-5: Experiment 1: Varying the Wave Height (H). The wave spectrum per experiment (Time (s) vs. Vertical position (Y (mm)). FFT data displayed as the wave period (T (s)) vs. magnitude/power.	33
Figure 3-6: Experiment 2: Varying the wave period (T) The wave spectrum per experiment (Time (s) vs. Vertical position (Y (mm)). FFT data displayed as the wave period (T (s)) vs. magnitude/power.....	34
Figure 3-7: An extract from the establishment of a corrective wave of $T = 1$ $H = 60$ mm in the wave flume	36
Figure 3-8: Experimental FPB model configuration within a wave flume.....	37
Figure 3-9: FPB model showing the continuous flow direction assuming a wave moves from left to right	38
Figure 3-10: FPB model with the roller mechanism attachment. The roller moves from left to right.	39
Figure 3-11: Visual monitoring method used by (Yousif, Holdsworth, and Poepping 2010) to investigate the effects of matching refractive indices between the liquid and tube mediums.....	41
Figure 3-12: Air-bubble impurities present before (A) and after (B) optically enhancing the experimental conditions. Amsler grid placed behind the FPB tube.	42
Figure 3-13: Pixel image information derived from MATLAB Image viewer	46
Figure 3-14: control volumes 1-10 of the PIVlab masked regions (red) as the roller mechanism moves from left to right.....	47
Figure 3-15: Setting velocity limits within PIVlab	49
Figure 3-16: Blender GUI: Tracking the roller speed	50

Figure 4-1: Mean fluid flow pattern over CVs 1-10 due to the direct influence of the roller on the tube's lower boundary	51
Figure 4-2: Mean flow vector per CV	52
Figure 4-3: Mean velocity parameters of the flow over CVs 1-10	53
Figure 4-4: Non-dimensionalised velocity profiles in relation to the roller-peak position	56
Figure 4-5: Instantaneous streamline plot per CV	58
Figure 4-6: Fluid motion under the influence of the rollers pressure profile. The roller moves from left to right. The fluid is displaced along the curved profile	58
Figure 4-7: Reynolds stresses per CV in relation to the roller-peak profile.....	60
Figure 4-8: Standard deviations per CV in relation to the roller-peak profile across the FOV	62
Figure 4-9: Velocity distribution around the mean (red marker) per CV	62
Figure 4-10: Detailed velocity magnitudes across each CV under direct contact with the tube profile.	63
Figure 4-11: Mean velocity profiles per CV	64
Figure 4-12: Cross-sections taken across the FOV per CV.....	65
Figure 4-13: CV1: Velocity profiles at cross-sections	66
Figure 4-14: CV2: Velocity profiles at cross-sections	67
Figure 4-15: CV3: Velocity profiles at cross-sections	68
Figure 4-16: CV4: Velocity profiles at cross-sections	69
Figure 4-17: CV5: Velocity profiles at cross-sections	70
Figure 4-18: CV6: Velocity profiles at cross-sections	71
Figure 4-19: CV7: Velocity profiles at cross-sections	72
Figure 4-20: CV8: Velocity profiles at cross-sections	73
Figure 4-21: CV9: Velocity profiles at cross-sections	74
Figure 4-22: CV10: Velocity profiles at cross-sections	75
Figure 4-23: Shear rate at CV1 and the U velocity cross-sections along corresponding cross-sectional lines. U profiles hold a negative velocity gradient (Circled)	77
Figure 4-24: Shear rate at CV10 and the U velocity cross-sections along corresponding cross-sectional lines. U profiles hold a negative velocity gradient (Circled)	80
Figure 4-25: Strain rate at CV1	81

Figure 4-26: Strain rate at CV10. Condensed pockets of positive and negative strain which correspond in position to the strong negative shear layer.	82
Figure 4-27: Vorticity at CV1	83
Figure 4-28: Vorticity at CV10	85
Figure 4-29: Mean velocity components relative to the roller speed	86
Figure 4-30: Mean U and V velocity across CVs 1-10.....	86

LIST OF TABLES

Table 2-1: Output mass of bio-oil per ton of dry biomass [kg/t] (Bwapwa, Anandraj, and Trois 2017)	9
Table 3-1: Analytically derived parameters to provide sufficient pixel resolution per particle vs measured parameters.....	44
Table 3-2: Manually set PIVlab’s image pre-processing settings	47
Table 3-3: Manually set PIVlab’s Image-evaluation settings	48
Table 3-4: Vector Validation Settings	48
Table 4-1: Mean velocity relations in reference to Figure 4-3 (TP: Turning point).....	54
Table 4-2: Location of minimum and maximum Reynolds stresses across the FOV for CVs 1-10 in reference to Figure 4-7	61

NOMENCLATURE:

h	Water Depth
H	Wave Height
L	Wave length
g	Gravitational acceleration

ACRONYMS:

FPB	Floating flexible photobioreactors
PB	Photobioreactors
OMEGA	Offshore Membrane Enclosures for Growing Algae
CCS	Carbon Capture and Sequestration
KE	Kinetic Energy
PIV	Particle Image Velocimetry
FFT	Fast Fourier Transform
SNR	Signal to Noise Ratio
FOV	Field of View
LED	Light Emitting Diode
GUI	Graphic User Interface
CLAHE	Contrast Limited Adaptive Histogram Equalization
IA	Interrogation Area
DCC	Direct cross-correlation
DFT	Discrete Fourier Transform
C	Carbon
N	Nitrogen
SWL	Still Water Level

CV Control Volume

TP Turning Point

CHAPTER 1: INTRODUCTION

1.1 PROJECT DESCRIPTION:

The world is expected to experience a global energy crisis due to its continued dependency on non-renewable fossil fuels (IEA World Energy Outlook 2009). Society requires an adaptive response to cope with dominating global issues such as global warming, population increases, and environmental degradation. A global economy that functions on sustainable methods can be used to mitigate the effects of climate change. Emerging sustainability practices require transitioning from a fossil-based economy to a biobased one (European Commission and Innovation 2012). The power generation industry is the most crucial sector requiring strategic planning to achieve economic and environmental sustainability (Maulud and Saidi 2012). Initiatives within the bioenergy industry, such as large-scale microalgae cultivation, offer technological advances in biomass conversion and support carbon neutrality.

Microalgae have attracted global interest due to their extensive application potential in renewable energy, biopharmaceutical, and nutraceutical industries (Khan, Shin, and Kim 2018). Microalgae feedstocks offer economically sustainable and renewable sources of biofuels, bioactive medicinal products, and food ingredients. Growing economic and environmental concerns within the aviation sector have caused an ever-growing recognition to the demand for alternative emerging fuels; and a shift towards “green aviation” (Chisti 2007). Currently, the aviation sector relies largely on petroleum jet fuel as it is the most economically efficient energy carrier (Bwapwa, Anandraj, and Trois 2018). Globally unsteady fluctuations in the price of oil have generated an opportunity for a sustainable fuel supply; the establishment of which would strengthen the economies for fuel users (Bwapwa, Anandraj, and Trois 2017).

Biodiesel production from traditional feedstocks such as oil crops and animal oils cannot realistically and sustainably compete with the transport fuel demand due to their inefficient growth rates and reliability on essential resources such as arable land, water, and energy (Chisti 2007). Whereas under optimal conditions, the typical growth of microalgae

biomass can double daily (Flynn 2019). Bio-oil derived from micro-algal biomass has proven to be ideal for jet fuel based on its similarity to petroleum crude oil. This is due to its high percentage of short-chain fatty acids that can reach a high number of carbon chain lengths (Bwapwa, Anandraj, and Trois 2017). Biofuel production from microalgae feedstock has proven a larger biofuel yield than traditional feedstocks (Trent 2012). This is due to their high photosynthetic efficiencies and growth rate potentials (Trent 2012).

NASA has proposed an innovative biomass production scheme that exploits mass microalgae cultivation. The scheme is called The Offshore Membrane Enclosures for Growing Algae (OMEGA) initiative and comprises floating flexible photobioreactors (FPBs) (Trent 2012). FPBs act as microalgae cultivation enclosures. The initiative aims to collaboratively grow algae, purify wastewater, aid in carbon sequestration and ultimately produce microalgae biomass for biofuel production (Trent 2012).

FPBs are deployed offshore, and are seeded with potential coastal wastewater discharge as a microalgae nutrient source (Trent 2012). Under the influence of sunlight and ocean wave-induced pressures, FPBs aim to accelerate microalgae production at a zero-energy input cost. The pumping and mixing within FPBs are driven by external oceanic wave-induced pressures that drive an internal collapsible flow within the flexible tubes. The expansion and contraction of the FPB tubes can be related to the peristaltic motion in vascular systems due to transmural pressures (Grotberg and Jensen 2004) but at higher Reynolds numbers.

Microalgae require explicit physical and chemical conditions to achieve optimal growth rates (Flynn 2019). Mixing is an essential physical parameter required for effective microalgae production. Mixing allows microalgae cells to be equally exposed to sunlight and nutrients and improves the aeration and chemical reaction exchange. The suspension and re-suspension of algal cells prevent sedimentation and the generation of dead zones due to algal clumping.

An internal flow within the FPB tube is produced when the external wave pressure exceeds the internal pressure. The magnitude of the tube deformation is dependent on

the intensity of the influencing wave profile. Deformations in the tubes cross-sectional area drive an internal collapsible flow. The magnitude of the internal flow is therefore dependent on the parameters governing the influencing wave.

1.2 RESEARCH BACKGROUND:

Offshore microalgae cultivation enclosures can be provided through floating flexible photobioreactors (FPBs) placed offshore. The pumping and mixing within FPBs are driven by an internal collapsible flow due to fluctuating external ocean wave pressures (Trent 2012). The magnitude of the internal flow is dependent on the parameters of the influencing wave. Mixing allows for microalgae cells to be equally exposed to sunlight, nutrients and leads to improved aeration and chemical exchanges (Ugwu, Aoyagi, and Uchiyama 2008).

The expansion and contraction of the FPB tube under an external wave pressure can be related to the peristaltic motion in vascular systems due to transmural pressures (Grotberg and Jensen 2004); in which the external pressure differs from internal tube pressure causing either an expansion or contraction in the tubes cross-sectional area. In this study, an FPB model is tested under idealised conditions in a laboratory wave flume. The internal fluid flow structure is analysed under a fixed induced wave pressure and frequency. Observations are made for high Reynolds number values, i.e. turbulent flow conditions. The FPB is seeded with neutrally buoyant micro-balloon particles (of average 60-80 μm), which are used to trace fluid flow. The tracer particles are illuminated under a concentrated LED light stream and are observed by a high-resolution monochromatic camera. The flow structure is quantified and analysed using particle image velocimetry (PIV). The fluid flow pattern is observed under the influence of a constricting wave profile. This research aims to identify the effect of pressure on the internal flow pattern within an FPB.

1.3 RESEARCH QUESTIONS:

- How does the external pressure affect the characteristics of the internal fluid flow structure and the location of the turbulent/mixing zones within the FPB?

1.4 AIMS:

- Analyse and depict the internal fluid-structure within the FPB due to peristaltic motion at a high Reynolds number.

1.5 OBJECTIVES:

- Generate idealised wave conditions on a FPB model and monitor fluid flow.
- Characterize small scale flow fields using PIV and establish a flow pattern configuration.
- Identify how fluid velocity, vorticity and shear stress arrangements vary under varying wave parameters.
- Quantify average flow rates and establish an average flow direction per control volume.
- Identify regions of strong turbulence/mixing

1.6 RESEARCH OUTLINE:

This research aims to investigate the internal flow structure at high Reynolds numbers within flexible tubes for a simulated wave-induced pressure. Fluid flow velocities are calculated using particle image velocimetry (PIV). Particle pixel displacement data is captured using a high-resolution monochromatic camera and is processed using PIVlab. Results of this experiment show the effect of external pressure on the internal fluid motion within the FPB. The results of this research aim to investigate/identify and build a better understanding of how a fluids structure alters under the influence of an induced wave profile.

1.7 RESEARCH APPROACH:

The approach adopted for the following research is as follows:

1. A literature review (Chapter 2) acknowledges the relevant background information, relationships and governing experimental parameters required to conduct the study.

2. The experimental methodology (Chapter 3) provides a detailed approach for each experimental setup and chosen method, how experiments were conducted and how results were gathered.
3. Results and discussion (Chapter 4) provides a review of the data under investigation for this research. Data is analysed and depicted to identify the relationships found and the observations made.
4. Conclusion and recommendations (Chapter 5) highlights the observations made from the results and provides additional suggestions for future research.

CHAPTER 2: LITERATURE REVIEW

2.1 BIOENERGY THROUGH MICROALGAE EXTRACTION

The consumption of liquid fuel is the largest contributor to global energy use (U.S. EIA 2010). Bio-economies are enriched through the advancements in bioenergy production which promote food security, climatic and environmental protection, and positive economic shifts (European Commission and Innovation 2012). Large-scale biomass production and cultivation aims to eradicate the global dependency on non-renewable fossil fuels. The bioenergy industry continuously aims to pursue efforts toward carbon neutrality by ensuring the technological advancement of biomass conversion.

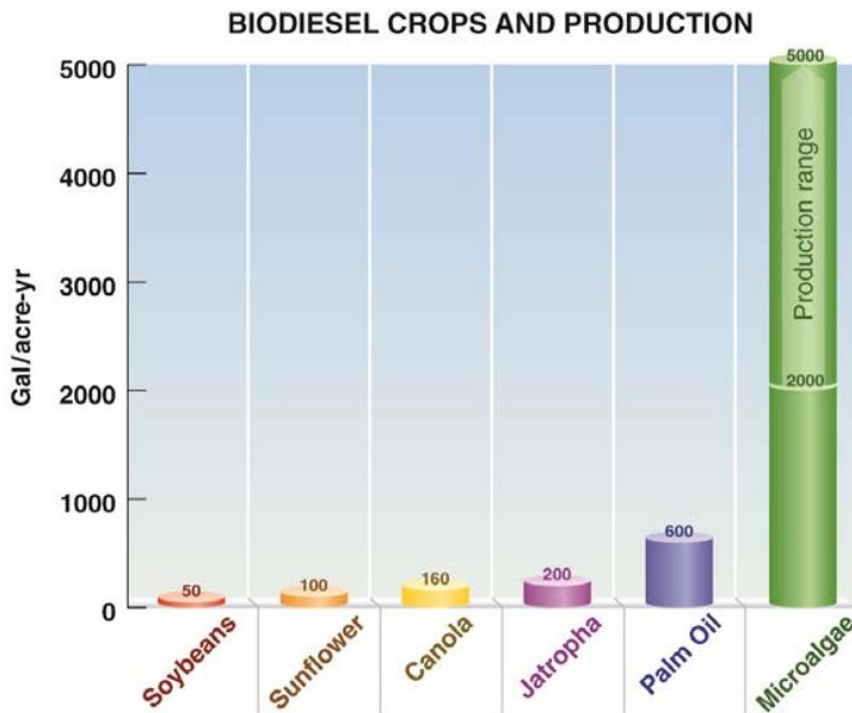


Figure 2-1: Microalgae produces more oil per acre in comparison to its rival terrestrial plants (Trent 2012)

Biomass is utilised to produce biofuels (e.g. biodiesel, bioethanol and biogas). Success within the bioenergy industry is based on its ability to provide a high energy return on investment (EROI). The most significant concern within the future of the bioenergy industry however is that modern infrastructure should not compete with arable land or

water resources (Trent 2012). Predominant biomass cultivation practices still pose a strain on these valuable resources and demand a high total operating energy demand (Trent 2012). In order to maintain a high EROI these areas of concern need to be addressed; and initiatives towards large-scale biomass cultivation must positively compete with modern dominating biofuel crop practices.

Microalgae provides a solution to the future of the bioenergy industry; as it is the fastest growing biomass and best oil producer (Figure 1). Microalgae provides a high yield potential feedstock for biofuel production; due to its high photosynthetic growth rates and high lipid content (Trent 2012). Due to their single-cellular structure and large surface area per unit mass; microalgae yields higher metabolic efficiencies in comparison to traditional feedstocks (e.g. animal fats, palm oil and vegetable oils). The microalgae species is versatile as it does not require freshwater, grows rapidly, can grow in marine water or wastewater, does not require arable land and produces oil that is not a threat to food security (Bwapwa, Anandraj, and Trois 2017). Biofuels extracted from microalgae (third generation biofuels) therefore require less valuable resources in comparison to traditional feedstocks; most notably water and agricultural land.

2.2 OFFSHORE MEMBRANE ENCLOSURES FOR GROWING ALGAE

Large-scale microalgae cultivation through photobioreactors (PBs) are currently perceived as uneconomical due to their short life span and high operating costs (Trent 2012). The offshore membrane enclosures for growing algae (OMEGA) is a NASA based initiative aimed at providing an environmentally compatible and economical solution to large-scale microalgae cultivation with a high EROI. OMEGA aims to utilise flexible photobioreactors (FPBs) as potential large-scale microalgae cultivation enclosures. Global environmental concerns have been placed on coastal cities due to rising sea-levels; the OMEGA system aims to harness coastal wave energy by housing flexible photobioreactors placed offshore (Trent 2012).

The system comprises an array of clear and inexpensive plastic FPBs which are richly seeded with freshwater oleaginous microalgae. Oleaginous microalgae is a species of

microalgae which can accumulate lipids >20% of the biomass (Trent 2012). The OMEGA modules are deployed offshore where the FPBs float just below the surface of the ocean. The initiative aims to collaboratively combine wastewater treatment with microalgae cultivation for the production of biofuel feedstock. Microalgae cultivation is supplemented with wastewater and carbon dioxide (CO_2) as a culture nutrient source and utilises natural sunlight for growth. Under the influence of natural wave energy, sunlight and CO_2 supplementation; microalgae cultures within FPBs are given favourable conditions to grow rapidly. Wave energy drives chemical exchanges between algal cells and accelerates microalgae production. The system further aids in the advanced treatment of wastewater by utilising municipal wastewater discharge disposed of from coastal cities (Trent 2012) while dually not competing with agricultural land use. The initiative thus promotes the mitigation of 'dead-zones' in coastal regions (Grotberg and Jensen 2004).

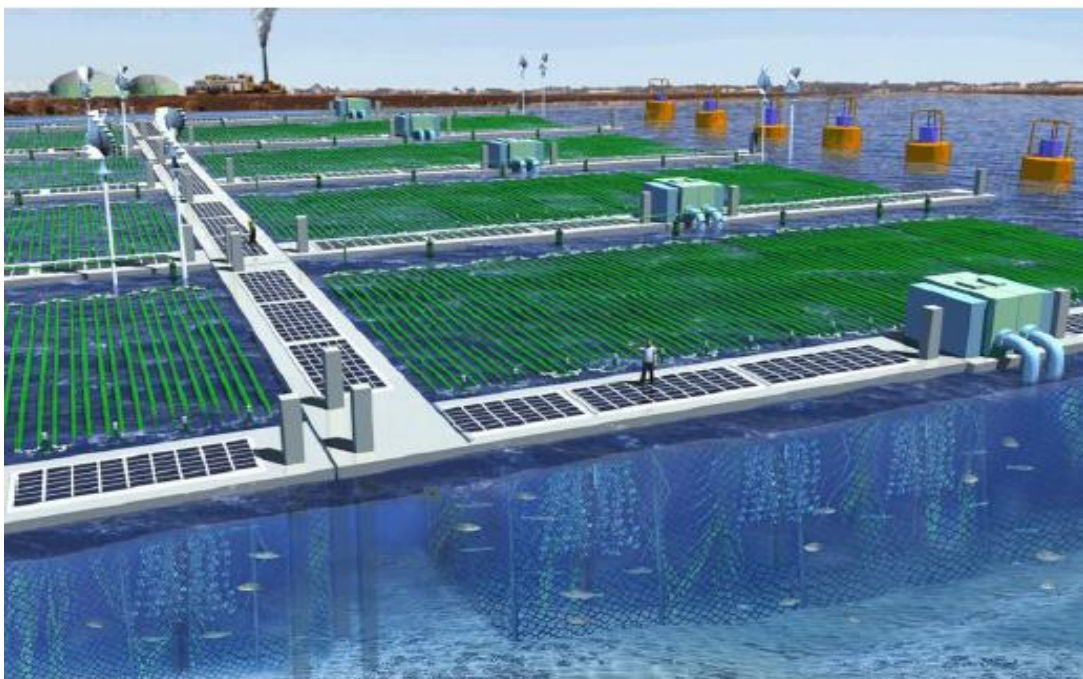


Figure 2-2: Conceptualized OMEGA scheme including aquaculture housing, solar panels and wind turbines (Trent 2012)

The OMEGA project aims to provide the commercial infrastructure needed for large-scale microalgae cultivation; where the future of the OMEGA project aims to create self-sustaining, multifunctional offshore platforms. OMEGA platforms aim to become self-efficient by integrating localised electricity generation through solar panels, wind turbines

and wave-energy generation; and by utilising waste carbon dioxide and wastewater discharge to thus produce high yields of biomass. The OMEGA initiative greatly reduces the reliance on water, energy and fertilizer inputs needed in traditional bioenergy production and leads to significant reductions in carbon emissions through carbon capture and sequestration (CCS) (Trent 2012). Isolated stations further aim to produce food crops by housing aquaculture beneath its floating dock.

2.3 BIOFUEL PRODUCTION FROM MICROALGAE BIOMASS

The OMEGA initiative aims to harness the accelerated growth rate efficiencies and high lipid contents of microalgae (ideal for biofuel production) to provide an economically sustainable market solution to large-scale microalgae cultivation and biofuel production. The utilisation of microalgae feedstocks ensure a high output rate of high-quality bio-oil. Biodiesel is produced by utilising fatty acids which are synthesised by the microalgae (Kenny and Flynn 2017). The large-scale production of biofuel from mass microalgae cultivation ensures no threat to food crops, does not require arable land, and does not pose a threat to valuable water resources. Dewatered by-product biomass can also be converted into high-demand consumer products such as fertilizer, animal feed, and higher value-added algal products within the biopharmaceutical and nutraceutical industries (Trent 2012). According to (Ren et al. 2018), *Botryococcus braunii* of the microalgae species showed an oil yield as high as 68%. The oil yield potential was also notably highlighted for *Nannochloropsis* and *Schizochytrium* in (Bwapwa, Anandraj, and Trois 2017) (Table 2-1).

Table 2-1: Output mass of bio-oil per ton of dry biomass [kg/t] (Bwapwa, Anandraj, and Trois 2017)

Microalgae Species	Output: Mass of bio-oil per ton of dry biomass [kg/t]
<i>Botryococcus Braunii</i>	250-750
<i>Nannochloropsis sp.</i>	310-680
<i>Schizochytrium sp.</i>	500-770

Other than primary biofuel production; there is also an opportunity for a smoother transition into the market by blending algae oil with petroleum oil. This would minimise the carbon footprint on petroleum products as blended compositions slow down the speed of depletion (Bwapwa, Anandraj, and Trois 2017).

2.4 MIXING OF MICROALGAE CELLS

Microalgae are grown in liquid suspension where organisms are free-floating. A microalgal culture typically grows through a process of binary fission or multiple forking, both of which are a process of cell division (Flynn 2019). An increase in cell abundance causes microalgae cultures to shield the surface of a waterbody and limit light penetration to surrounding cells. This is referred to as self-shading in which cell growth becomes self-limiting due to the increasing density of the microalgal biomass. Growth rates consequently deplete due to the restriction of both light photons and nutrient exchange potential to underlying and neighbouring cells (Flynn 2019). Self-shading becomes more prominent within systems where movement is limited or restricted as culture growth is non-agitated and cells are prone to clumping.

To maximise the production of high-quality lipid quantities for biodiesel production, the system must optimise the output of fatty acids. According to (Flynn 2019), fatty acids are synthesised primarily when the system enters N-deplete growth (is in Nitrogen depleting/restricting conditions). When the N-nutrient is exhausted, C-biomass growth continues where it is deposited as starch and/or lipid (Flynn 2019). The optimization of the system is dependent on a balance between light availability and nutrient cell exchange. This requires a balance between nutrient limitation and the continued growth of microalgae in optically thin suspensions (Kenny and Flynn 2017). Some degree of turbulence is essential to ensure that cells are habitually exposed to light and to promote chemical exchange potential through mixing (Carlozzi 2002)..

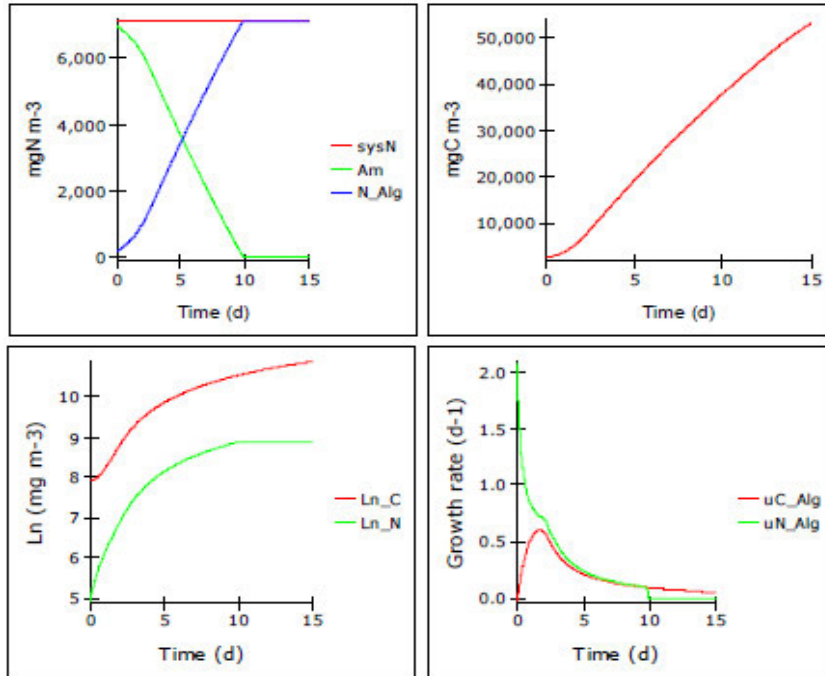


Figure 2-3: Simulated growth pattern in a bioreactor with a deep optical depth (0.5m) under constant illumination for a 15 day period (Flynn 2019)

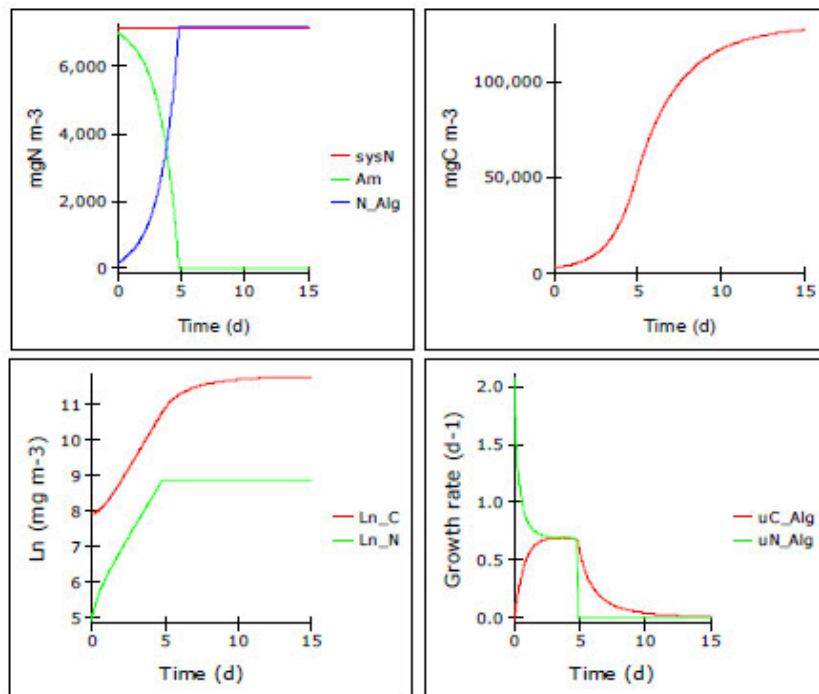


Figure 2-4: Simulated growth pattern in a bioreactor with a shallow optical depth (0.05m) under constant illumination for a 15 day period (Flynn 2019)

In more optically thin suspensions i.e. less dense suspensions (where cells have more photon availability) the N-deplete stage is achieved more rapidly over time (comparison of Figures 2-3 and 2- 4). There is consequently an increase in the carbon-to-nitrogen ratio (C: N). Harnessing higher C: N ratios optimize the production of the fatty acid content in the biomass (Singhasuwan et al. 2015). In a shallow system growth is exponential and ideal for high fatty acid products (shown by the linear section of the Ln plot in Figure 2-4); whereas in a deeper system growth is linear as cells are never in a steady growth state due to increased self-shading (Ln plot in Figure 2-3) (Flynn 2019). In darkness there is also a loss in the portion of biomass previously accumulated during phototrophic growth.

Light availability is an essential parameter for microalgal growth and productivity. When cells are placed under stress they release metabolites into the growth medium which further contaminate the value of the algal crop by promoting bacterial and fungal activity (Flynn 2019). Increased productivity and crop quality can be achieved through mixing. Induced turbulence promotes chemical nutrient interactions, improved aeration and increased photon absorption through enhanced cell circulation. Shear drives turbulence due to unsteady velocity fluctuations. However, excessive shear can increase cell mortality and therefore decrease the growth rate potential and cell viability (Wang and Lan 2018). Microalgae species therefore hold a shear sensitivity factor, whose tolerance is based on the strength of the cell wall and cell morphology (Wang and Lan 2018). Cultures grown in laminar flow systems are prone to photo inhibition and light limitations which suppress algal growth productivity (Qiang, Guterman, and Richmond 1996). Microalgae therefore requires explicit physical conditions to ensure optimal growth under mixing.

Microalgae cells that are starved of light and nitrogen nutrients tend to reach smaller volumetric sizes; and those limited by phosphorous become sticky and clump together (Flynn 2019). Algal clumping can be motile or non-motile; where cells may congregate either on the surface or the bed of a waterbody respectively (Flynn 2019). Cell sedimentation occurs when flocs of algae settle under the influence of gravity this quiescent process is referred to as cell sedimentation (Zhu, Li, and Hiltunen 2018). To

limit cell sedimentation within FPBs; cultures must be forced into suspension (Trent 2012).

Optimum microalgae growth rates are dependent on explicit physical and chemical conditions. Mixing is an essential parameter in the design of a photobioreactor (Ugwu, Aoyagi, and Uchiyama 2008). Physical mixing drives the suspension and re-suspension of algal cells. By ensuring mixing in the micro-algal liquid suspension; cell sedimentation becomes limited (Trent 2012). Optimized mixing ensures a high cell concentration, enforces algal cells into suspension, aids in nutrient distribution and improves gas exchange, limits thermal stratification, and reduces self-shading which lowers the probability of photo inhibition (Javanmardian and Palsson 1991). According to (Carlozzi and Torzillo 1996), an increase in turbulence improves both nutrient exchange rates and light exposure in photobioreactor cultures; where induced turbulent mixing results in a higher yield of algal biomass (Ugwu, Aoyagi, and Uchiyama 2008) .

A common problem for bioreactor cultivation is the micro-algal growth on the inner walls (biofouling) of the bioreactor (Trent 2012); the accompanying biofilm is also not readily harvestable and contaminates the quality of the biomass crop (Flynn 2019). Biofouling decreases light penetration and reduces diffusion gradients which limit nutrient acquisition. Mixing reduces/limits biofouling, algal clumping and the generation of 'dead zones' by improving mass transfer (Huang et al. 2017).

2.5 PERISTALTIC MOTION IN FLEXIBLE PHOTOBIOREACTORS

Typically closed volume photobioreactors require a pumping mechanism to induce turbulent mixing into the system (Flynn 2019). Trent (2012) used, swirl vanes to circulate micro-algal cultures and increase mixing within the OMEGA FPBs. This study aims to examine the turbulent motion within an FPB system under the influence of an external wave force; by investigating how the magnitude of the external wave energy influences the internal flow within the FPB.

Under the influence of naturally occurring wave-driven currents, wave energy is transferred to the flexible tube which propels a complex internal flow within the FPB. The

flexible tube deforms, expanding and contracting under variations in external pressure. This is an essential process that drives mass transfer within FPBs further promoting nutrient exchange, aeration and light availability to the microalgal cells.

The flexible tube will maintain a circular cross-section when the internal pressure (P) is greater than the external pressure (P_e) (Figure 2-5). As P_e approaches P the tube shape becomes more elliptical. When P_e exceeds P , the tube begins to buckle and flatten; experiencing a larger reduction in its cross-sectional area; forcing an internal collapsible flow (Grotberg and Jensen 2004). Peristaltic pumping can be characterised by the dynamic interaction of fluid flow with a flexible boundary (Hung and Brown 1976). The rapid expansion and contraction of the tube walls provide a pumping motion which enforces the suspension and resuspension of an enclosed algal medium. Under tube expansion the resultant internal flow moves in the direction of the propagating external wave. This movement can be compared to peristaltic motion in vascular systems under transmural pressures (Grotberg and Jensen 2004).

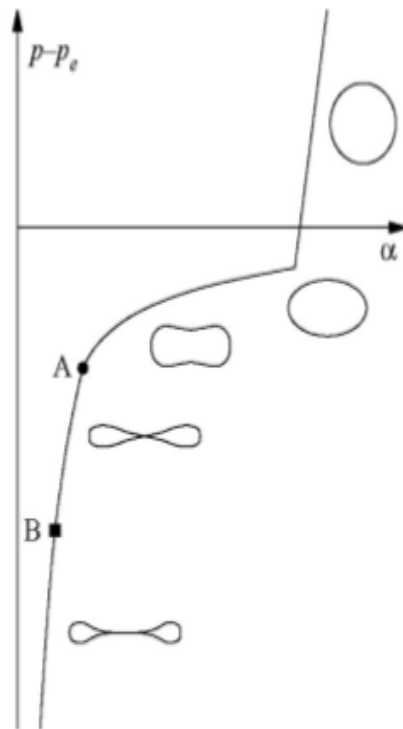


Figure 2-5: Relating $P - P_e$ to cross-sectional area. Where P is the internal pressure and P_e is the external pressure (Grotberg and Jensen 2004)

Variations in the external wave pressure on the flexible tube have a direct effect on the degree of growth (more circular shape) or reduction (more elliptical shape) of the tubes cross-sectional area. Although the cross-sectional area is conserved, the oscillations in the wall shape cause a repetitive pumping action which drives an internal flow within the FPB. The magnitude and frequency of the fluctuations in the cross-sectional area, are directly related to the magnitude of the induced internal flow (Pedley and Pihler-Puzovic 2015). The total applied pressure is a combination of the overbearing water volume and the subsurface pressure, dependent on the depth of the tube. The subsurface pressure (P) under a breaking wave is a summation of the dynamic (P_d) and hydrostatic pressure (P_h) such that according to Dean and Dalrymple 1991:

$$P = P_d + P_h \quad (1)$$

whence

$$P_d = \rho g \eta K_p(z) \quad (2)$$

$$K_p(z) = \frac{\cosh k(h+z)}{\cosh kh} \quad (3)$$

$$P_h = -\rho g z \quad (4)$$

Where ρ is the fluid density, g is the force of gravity, K_p is the pressure coefficient, η is the overbearing external wave profile, h is the still water level, and z is the water surface elevation from h . The external wave pressure force on the distensible tube causes pulse ring waves on the tube wall that move transversely to the net average fluid flow (Barton and Raynor 1968). Fluctuations in the tube profile generate variations in the internal fluid pressure which drives a complex flow.

The radial displacement $\zeta(Z, t)$ of a two-dimensional tube wave profile (Figure 2-6) enclosing an incompressible, homogenous, viscous Newtonian fluid can be described according to Muthu, Kumar, and Chandra 2001 as:

$$\zeta(Z, t) = a \cos \frac{2\pi}{\lambda} (Z - ct) \quad (5)$$

$$k = \frac{2\pi}{\lambda} \quad (6)$$

$$\epsilon = \frac{a}{d} \quad (7)$$

$$R = d + \zeta(Z, t) \quad (8)$$

where a is the amplitude, c is the wave velocity, λ is the wavelength, d is the radius of the flexible tube, t is the time, k is the wavenumber, ϵ is the amplitude ratio and R is the radial coordinate. R is defined as the fluid boundary condition (Muthu, Kumar, and Chandra 2001). $\zeta(Z, t)$ is taken from the mean axial coordinate (Z) of the inextensible and impermeable tube.

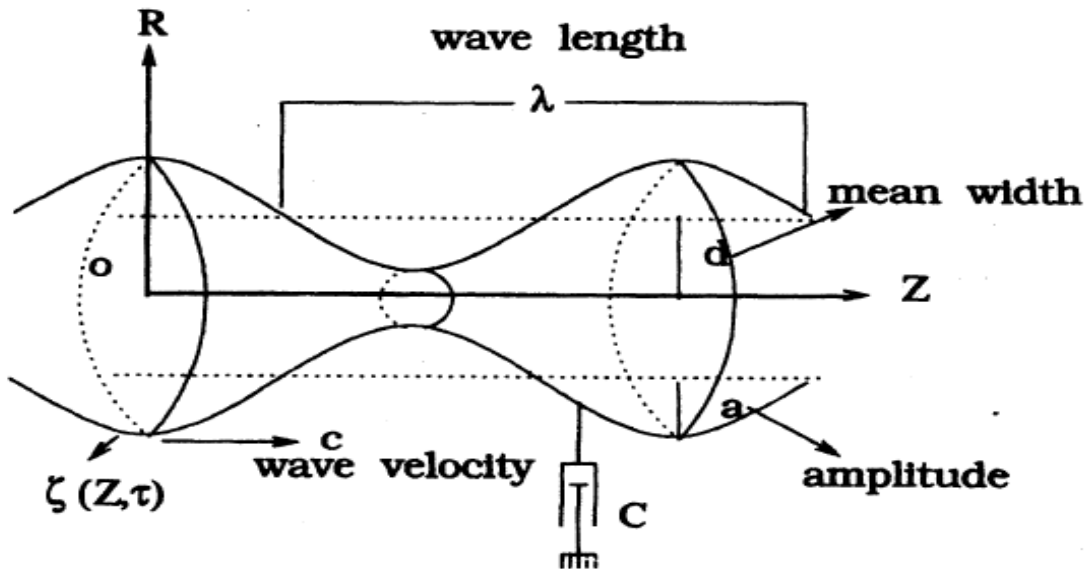


Figure 2-6: Geometry for the two-dimensional peristaltic flow on a cylindrical tube wall (Muthu, Kumar, and Chandra 2001)

Equation 5 is based on the assumption that the flow is axisymmetric and the wavelength is larger than the wave amplitude (or $\lambda \gg a$) (Yin and Fung 1971). It is assumed that particles on the wall of the tube have no longitudinal displacements (F. Yin and Fung 1969). Due to the no slip conditions the tube is therefore assumed to have only transverse displacements. The velocity components of the fluid particles on the tube wall, according to F. Yin and Fung 1969, can be denoted as:

$$V_R = \frac{\partial \zeta}{\partial t} \quad (9)$$

$$V_Z = 0 \quad (10)$$

where V_r is the radial velocity and V_z is the axial velocity.

2.6 MEASURING FLUID-STRUCTURE INTERACTIONS

Turbulence originates due to instabilities in laminar flow; due to variations in the velocity gradients. These instabilities can be interpreted by using the governing equations of motion and the interaction between the viscous and nonlinear inertia terms (Tennekes et al. 1972). In turbulent flow, fluid particles of different momentum collide and exchange kinetic energy. The chaotic interaction of turbulence promotes mixing. Turbulent flows are characterized as highly unsteady, irregular and random. Therefore deterministic analysis of these fluid flows are difficult and a statistical approach is often the simplest approach (Tennekes et al. 1972). Dimensional analysis provides a relation between both dependent and independent variables, making it one of the most powerful tools in the study of turbulence. Scaling laws are therefore the heart of turbulent research. The characteristics of turbulent flow can be described using mathematical models of the flow's diffusivity, and dissipation rate. (Tennekes et al. 1972).

Large scale eddies are responsible for most momentum and particle transport. Small eddies have very short time scales which tend to make them statistically independent to the mean flow (Tennekes et al. 1972). Turbulent flows are often independent of viscosity with the exception of very small scales of motion. Viscosity becomes increasingly more effective in dissipating velocity fluctuations for very small scales of motion by converting small scale energy into heat. Small scale motion is therefore dependent on the rate at which energy is supplied by large scale motion and on the kinematic viscosity. The net rate of change of small scale energy is related to the time scale; therefore the rate of energy supply should be equal to the rate of dissipation (Tennekes et al. 1972). The mean transport of turbulent energy or the dissipation rate (ε) can be described as:

$$\varepsilon \sim \frac{u^3}{l} \quad (11)$$

where l represents the width of the largest eddies or the width of the flow and u is the characteristic velocity scale or the rms amplitude of the velocity fluctuations; ν is the kinematic viscosity. Large scale eddies decay at a time scale of $\frac{l^3}{\nu}$ where their viscous energy loss proceeds at a rate of $\frac{\nu u^2}{l^2}$ (Bernard and Handler 1990). This is small in comparison to ε if the Reynolds number (R) is large. Turbulent momentum exchange is represented by an eddy viscosity. Large scale eddies continue to dissipate into smaller scales of motion until eddy sizes become small enough for the viscous dissipation of kinetic energy to become instantaneous.

The Kolmogorov scales are the smallest scales of motion at which the viscous dissipation of turbulence occurs. This describes an energy cascade of eddy length scales, where the energy of large eddies is converted to smaller eddies. This continues until the energy is dissipated directly to heat the fluid (molecular-scale jiggling) due to the fluid's viscosity. The Kolmogorov length and time scales decrease with increasing dissipation rates. The dissipation rate (ε) can be related to the Kolmogorov scales, where:

$$\eta = \left(\frac{\nu^3}{\varepsilon}\right)^{\frac{1}{4}} \text{ Is the Kolmogorov length scale} \quad (12)$$

$$\tau = \left(\frac{\nu}{\varepsilon}\right)^{\frac{1}{2}} \text{ Is the Kolmogorov time scale} \quad (13)$$

$$U = (\nu\varepsilon)^{\frac{1}{4}} \text{ Is the Kolmogorov velocity scale} \quad (14)$$

$$\text{The Reynolds number } (R) \text{ formed for } \frac{\eta U}{\nu} = 1 \quad (15)$$

$$\frac{\eta}{l} \sim \left(\frac{\nu l}{\varepsilon}\right)^{-\frac{3}{4}} = R^{-\frac{3}{4}} \quad (16)$$

$$\frac{\tau u}{l} \sim \frac{\tau}{t} = \left(\frac{\nu l}{\varepsilon}\right)^{-\frac{1}{2}} = R^{-\frac{1}{2}} \quad (17)$$

$$\frac{U}{u} \sim \left(\frac{ul}{\nu}\right)^{-\frac{1}{4}} = R^{-\frac{1}{4}} \quad (18)$$

Reynolds stresses refer to fluctuations in velocity that generate momentum fluxes/stress. Normal stresses contribute very little to the transport of mean momentum. The dominant role of mean momentum transfer is characterised by the “off-diagonal” components of the mean stress tensor (τ_{ij}), termed the shear stresses.

$$\tau_{ij} = -\rho u_i u_j \quad (19)$$

where ρ is the fluid density and i and j refer to the horizontal and vertical components within a Cartesian plane. The most powerful eddies are therefore those which can absorb energy from the shear flow most effectively (Tennekes et al. 1972). The application of the Reynolds stress decomposition requires velocity fluctuations u_i and u_j to be correlated as the energy of eddies must be maintained in shear flow; as there is a continuous loss in energy to smaller eddies. The most powerful eddies are those whose vortices’ principal axis is roughly aligned with that of the mean strain rate. These are the most effective in maintaining a strong correlation between u_i and u_j and in extracting energy from the mean flow (Tennekes et al. 1972).

The nature of turbulent flow can be characterised by high levels of fluctuating vorticity. In most turbulent flow the contribution of turbulence to the dynamic pressure is insignificant as $\frac{1}{2} \overline{u_j u_j} \ll \frac{1}{2} U_j U_j$ (the mean kinetic energy of turbulent velocity fluctuations is significantly small in comparison to the kinetic energy of the mean flow). The significance of shear stress therefore lies between the interaction of velocity and vorticity, this includes particle transport and vortex stretching (Tennekes et al. 1972). The length scale of an eddy decreases as the strain rate increases. The energy dissipation from large scale to small scale eddies is termed vortex stretching; in which vortices lengthen/stretch due the conservation of angular momentum. It is important to note that a two-dimensional flow is unable to turn or stretch the vorticity vector. Turbulent eddies transfer momentum away from the boundary layer. The fluid therefore slows down within the boundary layer region. Boundary layers generate the largest degree of turbulence due to the no-slip condition

(Tennekes et al. 1972). Velocity gradients are consequently stronger near the boundaries and decrease away from a boundary layer. Fluctuations in the velocity gradient generate regions of strong shear. Shear stresses drive turbulent mixing and the formation of eddies. The shear layer acts as a source of energy towards turbulent fluctuations and is therefore observed as a mixing layer. The viscosity near the wall is important parameter for the formulation of flow within the boundary layers.

Kolmogorov hypothesized that the amount of kinetic energy ($K.E$) in a turbulent flow carried by eddies of diameter (D): Within a range of length scales known as the inertial subrange.

$$K.E \propto D^{\frac{5}{3}}$$

Quantifying energy at different length scales is typically defined in terms of an energy spectrum involving the Fourier transform of a function measuring the correlations between the fluids velocities at different points in space.

2.7 WAVE SPECTRUM DECOMPOSITION

A uni-directional wave spectrum can be described as a composition of an infinite series of sine waves of varying amplitudes and frequencies (Reeve, Chadwick, and Fleming 2012). Spectral analysis can be used to analyse noise-like signals and provide the frequency decomposition in harmonics. Solving the spectral energy density histogram is a technique commonly termed the Fast Fourier Transform (FFT) method (Reeve, Chadwick, and Fleming 2012).

In Airy waves, the potential energy (E_p) is equal to the kinetic energy (E_k).

$$E_p = E_k = \frac{1}{16}(pgLH^2) \quad [J/m^2] \quad (20)$$

Where L is the wave length and H is the wave height. Surface tension is ignored as it is negligible for ocean waves. Hence according to Dean and Dalrymple 1991 the total energy per unit area (E_T) of sea surface can be expressed as:

$$E_T = \frac{1}{8}(\rho g H^2) \quad [\text{J}/\text{m}^2] \quad (21)$$

$$E \propto H^2$$

2.8 PARTICLE IMAGE VELOCIMETRY

Particles within a fluid are in constant motion undergoing collisions between each other. Matter therefore becomes discontinuous or discrete at microscopic scales. However it is possible to ignore the discrete molecular structure by observing the fluid within a continuum (Kundu 2003). Particle image velocimetry (PIV) is an optical measurement technique used to quantify the parameters of fluid flow visualisation; and is used to measure fluid velocity (Handapangoda, Galindo-Torres, and Scheuermann 2015). In PIV fluid flow is monitored by seeding the fluid medium with neutrally buoyant particles which trace fluid motion. PIV is non-invasive to fluid motion and is therefore applicable over a vast range of length and time scales; under both laminar and turbulent flow conditions (Xue, Charonko, and Vlachos 2014). Tracer particles provide a non-intrusive medium that immerses itself within the fluid and is assumed to move with the local flow velocity (Sokoray-Varga and Józsa 2008). Tracer particles are assumed to move homogeneously within a fluid between consecutive image pairs (Sokoray-Varga and Józsa 2008). The PIV method is governed by an Eulerian approach focusing on spatial parameters. Independent variables of the fluid motion are therefore based on both displacement (x) and time (t). The fluid flow is derived between the rates of change of $f(x, t)$ at each point following the displacement of the particles. The fluid pattern is recorded using a high-resolution digital camera. From consecutive image sets tracer particle pixel displacement information is captured. This provides a spatial distribution of the instantaneous velocity field even in highly unsteady flow conditions (Sokoray-Varga and Józsa 2008). Particle visibility (a sufficient particle to pixel ratio) is essential in optimizing the signal to noise ratio (SNR) and therefore enhances the measurement of the fluid flow structure. The effective illumination of tracer particles is therefore essential for PIV rendering.

A light-emitting diode (LED) improves particle visibility by providing a light sheet over a field of view (FOV) thus illuminating particles in the fluid. The high-powered LED emits repetitive light pulses which pulse at a frequency equivalent to the camera's frame acquisition rate. This ensures particles are effectively illuminated for each frame recorded. The effective illumination of particles improves the quality of the particle pixel displacement information between consecutive image pairs. The instantaneous particle velocity is extrapolated through the statistical cross-correlation of the particle displacement per interrogation area over a time step.

2.9 PIV ANALYSIS TOOLS

PIVlab is a MATLAB toolbox extension used to analyse the particle pixel displacement information over a recorded image sequence in order to quantify the flow (Thielicke and Stamhuis 2014). PIVlab analysis comprises of three main stages: image pre-processing, evaluation and post-processing (Figure 2-7). PIVlab's image pre-processing phase enhances the PIV measurement quality before image correlation. This phase focuses on enhancing the images' light conditions to enhance the particles' visibility within the field of view (FOV).

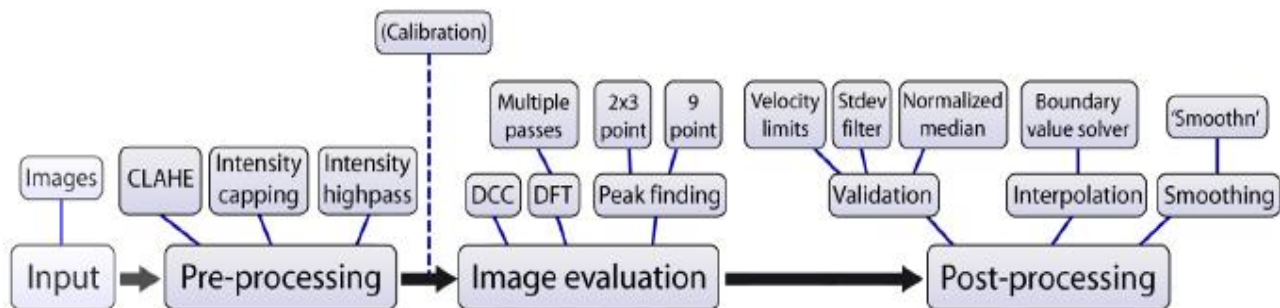


Figure 2-7: PIVlab workflow and implemented features (Thielicke and Stamhuis 2014)

Pre-processing steps include setting the:

Contrast limited adaptive histogram equalization (CLAHE):

CLAHE is targeted at small regions of the image. For each region the most recurrent intensities are spread over the images colour spectrum histogram for the full range of data. Areas of either low or high exposure are thus optimized independently. CLAHE

drastically increases the probability of detecting valid vectors by 4.7 ± 3.2 % (Thielicke and Stamhuis 2014).

Intensity High-pass:

The High-pass filter aims to improve the signal to noise ratio (SNR) of the data by minimizing the presence of low-frequency displacement data. A High-pass filter removes low-frequency background information caused by inhomogeneous lighting while conserving high-frequency information.

Intensity capping:

Image bright spots contribute more to the cross-correlation signal. An intensity cap aims to provide an upper limit for greyscale information in which all pixel's intensities that exceed the threshold are replaced by the designated upper limit. Intensity capping improves the probability of detecting valid vectors by 5.2 ± 2.5 % (Thielicke and Stamhuis 2014) by improving the pixel intensity and limiting the negative impacts caused by image modifications.

Weiner2 Denoise Filter:

The Wiener filter applies a smaller filter size to local image variance. Wiener2 aims to remove any further background noise (Thielicke and Stamhuis 2014). For cases of large or small image variance Wiener2 performs data smoothing while preserving image edges and high-frequency pixel information.

In deep PIV (DPIV) analysis the most sensitive aspect of computational rendering is the cross-correlation algorithm. Original input images are sub-divided into interrogation areas (IAs). Within each IA a cross-correlation is executed between image pairs. The cross-correlation algorithm is a statistical pattern matching technique that aims to calculate the particle displacement pattern between an IA pair (Thielicke and Stamhuis 2014). The resultant correlation matrix is used to determine the most probable pixel-displacement within each IA.

The image-evaluation phase focuses on the statistical algorithm applied to solving the cross-correlation matrix. The discrete cross-correlation function which computes the

cross-correlation matrix (C) aims to provide the most probable particle displacement between IAs A and B (representative of an IA pair).

PIVlab showcases two applicable approaches to solve the correlation matrix (C) equation:

- The discrete Fourier transform (DFT) method: where the correlation matrix is computed in the frequency domain (by using a circular cross-correlation) utilizing a fast Fourier transform (FFT).
- The direct cross-correlation (DCC) method: where the correlation matrix is computed in the spatial domain.

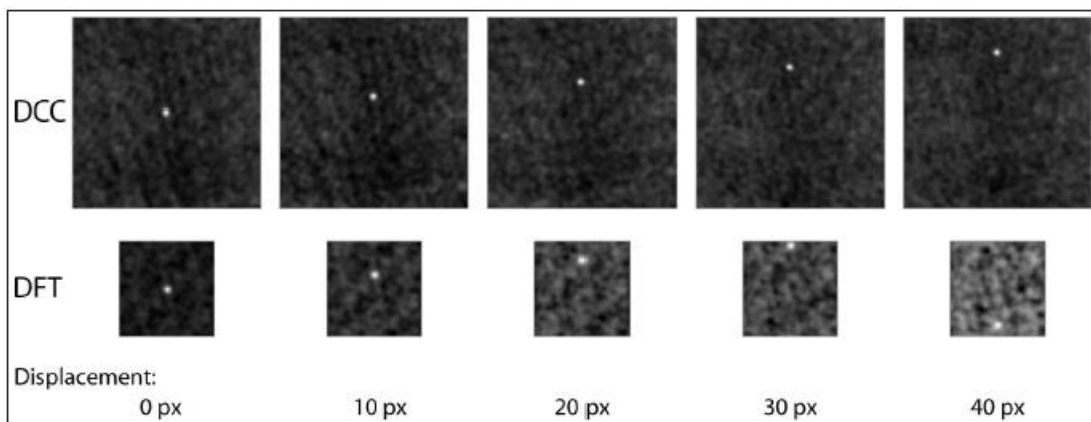


Figure 2-8: Correlation matrices of DCC and DFT investigate a single particle displacement (Thielicke and Stamhuis 2014).

The DFT method utilizes IAs of equal size which results in an increase of background noise in the correlation matrix and a consequent loss in pixel-displacement information (Figure 2-8). A loss in pixel data weakens the measurement of the pixel-displacement data due to the diminished accuracy of the cross-correlation matrix. To minimise the loss in pixel information PIVlab's DFT mode allows a user to instead run several DFT algorithms over the same set of data. This allows for a more refined set of data. Each DFT run is referred to as a 'pass'; in which the IA window size must decrease with every DFT pass run to further refine the vector.

For each DFT pass, displacement information is provided at nine separate positions inside an IA A (Figure 2-9 left). This is achieved by utilising either bilinear interpolation (faster) or spline interpolation (slower, more precision) with a direct effect on the correlations robustness (Thielicke and Sonntag 2021). The pixel information is

interpolated to derive the displacement of every pixel within the IA. The overall displacement vector is shown in the center of the IA (Figure 2-9).

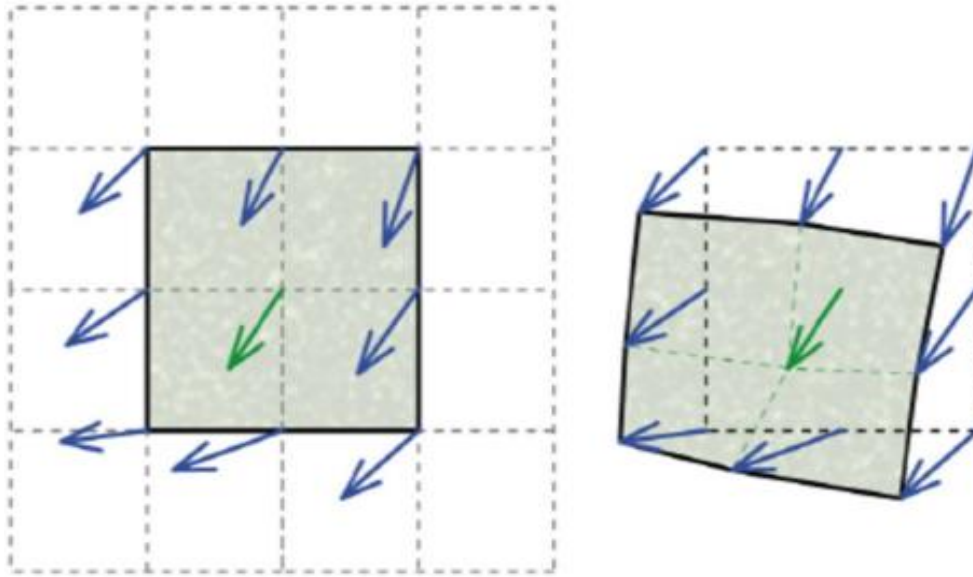


Figure 2-9: The window deformation technique for two passes (Thielicke and Stamhuis 2014)

The integer results of the first pass are used to offset the IA of the following pass B (Figure 2-9 right). IA B is subsequently deformed, and the successive displacement information is accumulated, resulting in a new matrix with less noise (Thielicke and Sonntag 2021). Between each pass, velocity information is smoothed and validated; and missing displacement information is interpolated. Deteriorating effects of interpolation and smoothing are corrected in the correlation of each pass. This process continues with the addition of every pass applied. Each IA grid is therefore refined with every pass. An increase in the number of applied passes minimises the potential loss of information, thus, increasing the overall accuracy of the displacement measurement (Thielicke and Stamhuis 2014). A displacement step of roughly a quarter of the IA is advisable in order to retain low background noise in the correlation matrix (Thielicke and Stamhuis 2014). For particle displacement greater than 50% of the original IA size, the correlation peak

will flip to the opposite side of the correlation matrix and thus makes the correct measurements impossible (Thielicke and Stamhuis 2014). Quality tests revealed that DFT using multiple window deformations outperformed DCC especially under challenging conditions (Thielicke and Stamhuis 2014).

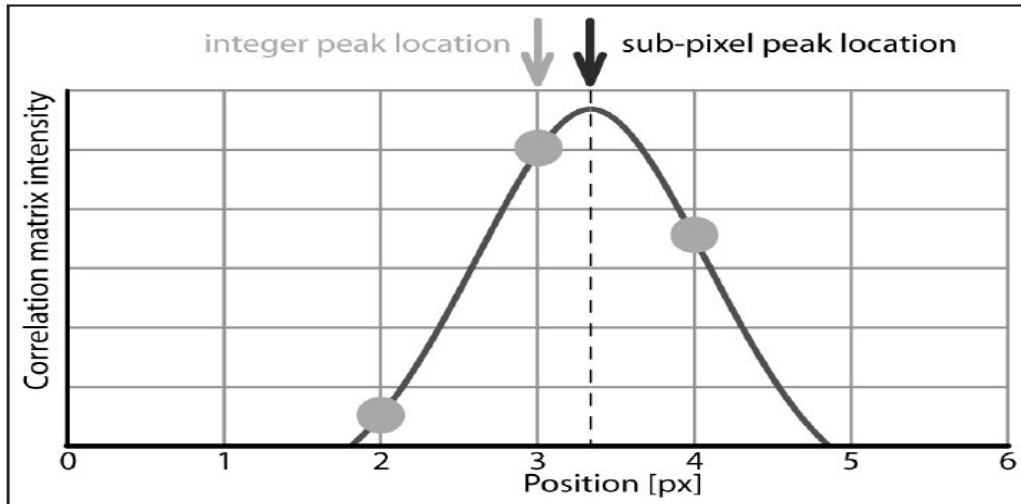


Figure 2-10: Gaussian 3 point fit. One-dimensional Gaussian function (solid line), Integer distribution of the correlation matrix (dots) (Thielicke and Stamhuis 2014).

The integer displacement value between two IAs is extracted at the location of the intensity peak of the correlation matrix (Figure 2-10). The 'peak finding' technique can be refined by utilizing the Gaussian function to fit to the integer intensity distribution (Thielicke and Stamhuis 2014). The peak of the fitted function is used to define the particle displacement with sub-pixel precision (Figure 2-10). A standard 3 point Gaussian fit utilizes only the adjacent vertical and horizontal pixels to evaluate the x and y axis separately. Sub-pixel precision is achieved by fitting a one-dimensional Gaussian function to the integer intensity distribution of the correlation matrix for both axes independently (Figure 2-10). In scenarios prone to shear and rotation, and images that suffer from excessive motion blur, the displacement peak may be an elliptical shape. A two-dimensional Gaussian function (9 point) performs better in such cases.

The data post-processing stage is required to refine the computational results. The initial approach is to manually allocate velocity limits to filter out vector outliers. Velocity

thresholds can also be implemented semi-automatically by comparing each vector with a lower and upper threshold:

$$t_{lower} = \bar{u} - n * \sigma_u \quad (22)$$

$$t_{upper} = \bar{u} + n * \sigma_u \quad (23)$$

Where \bar{u} is the mean velocity, σ_u is the standard deviation of u and n is the user define strictness of the filter. This filter adapts well to the nature of the flow (Thielicke and Stamhuis 2014). A local median filter evaluates the velocity fluctuation with respect to the median around a central vector. The median of this fluctuation is used as a normalization. With the removal of outliers, missing vector information is replaced with interpolated data. The standard interpolation utilizes a 3-3 neighborhood technique (3-3 mean) however two-dimensional linear and spline interpolation are alternatives. For large amounts of missing data, the boundary layer solver outperforms popular interpolators (Figure 2-11). A boundary layer solver is implemented in PIVlab, which is generally relatively smooth as the interpolation tends towards the average of the boundary velocities.

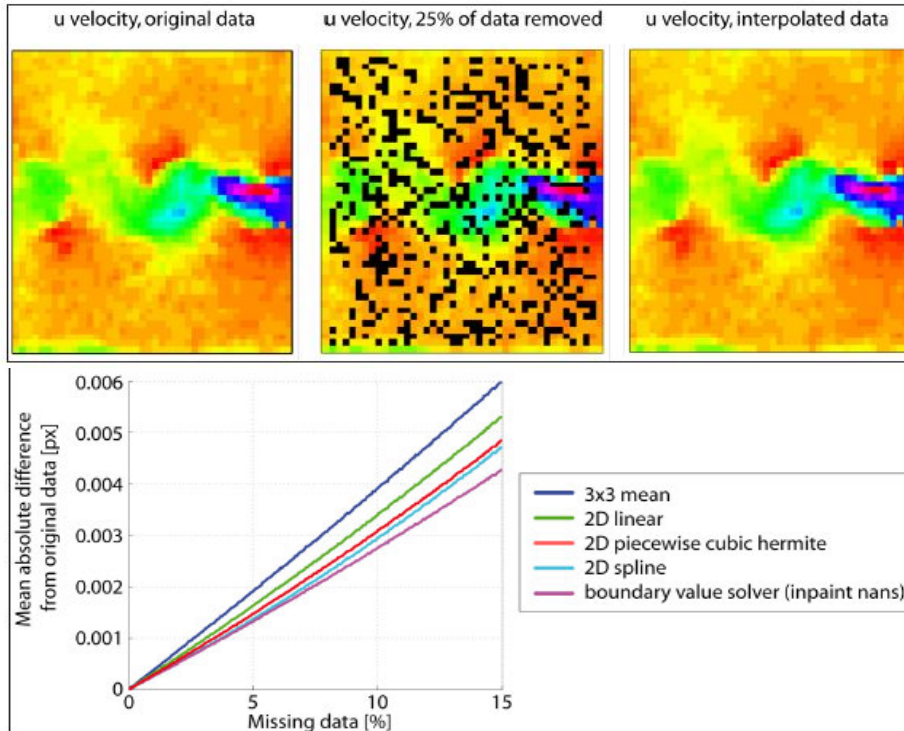


Figure 2-11: Performance of popular interpolation methods (Thielicke and Stamhuis 2014).

Measurement noise is inevitable; however, this can be reduced by data smoothing. A common and effective method of median filtering is used in PIVlab. Data smoothing, regardless of the algorithm used, always decreases residual noise introduced by the PIV cross-correlation algorithm (Thielicke and Stamhuis 2014). Data smoothing increases the quality of the velocity estimation by reducing the difference between the analysis and the true velocities. A data smoothing algorithm is implemented in PIVlab in order to further enhance the accuracy of the velocity estimation. Data noise can be further minimized by ensuring adherence to PIVlab's optimal conditions (Thielicke and Stamhuis 2014b): Particle image diameter of at minimum 3 pixels, IA density of 5-15 minimum, no particle pair loss and no motion blur.

CHAPTER 3: METHODOLOGY:

Laboratory wave generators are used to simulate natural wave propagation in a wave flume by relating non-dimensional ratios such as wave steepness, shallow wave ratio, flow rate and amplitude ratios, as well as both Reynold and Froude numbers (Dean and Dalrymple 1991). A piston paddle wave generator is used to generate waves in a laboratory wave flume. To maintain a level of confidence in preceding experimental investigations the wave generator is tested to prove the accuracy between the analytical wave inputs to real-life wave outputs. An experiment is done to ensure that the waves generated within the flume are applicable for this study. This ensures that the volume of water displaced by the paddle is equal to the volume of the crest of the propagating wave (Dean and Dalrymple 1991) (Figure 3-1). The stroke of the piston paddle in relation to the wave height (for sinusoidal waves) can be expressed in the following equation:

$$\frac{H}{S} = \frac{2(\cosh 2K_p h - 1)}{\sinh 2K_p h + 2K_p h} \quad (24)$$

$$\text{Wave Number } (K_p) = \frac{2\pi}{L} \quad (25)$$

Where the paddle stroke length (S) is therefore directly proportional to the wave height (H). L is the wave length and h is the water depth.

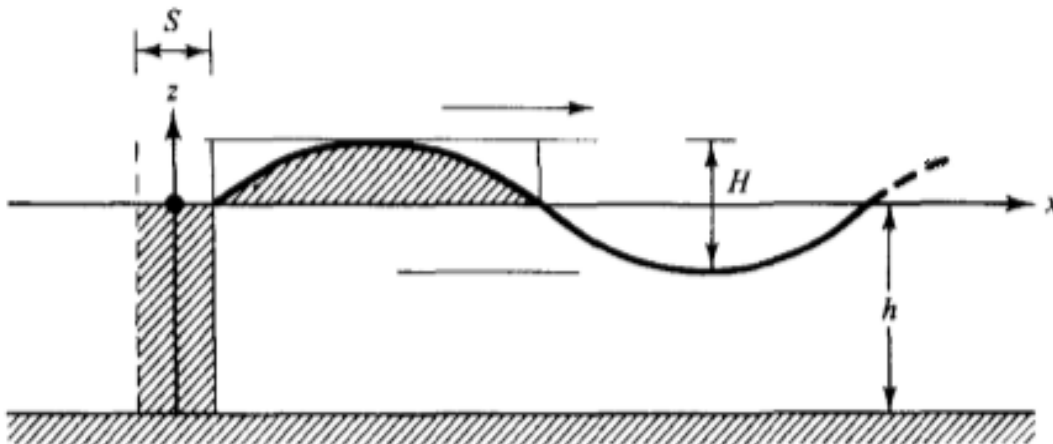


Figure 3-1: Piston paddle wave generator indicating the volume displaced by the paddle in relation to the volume of water in the crest (Dean and Dalrymple 1991)

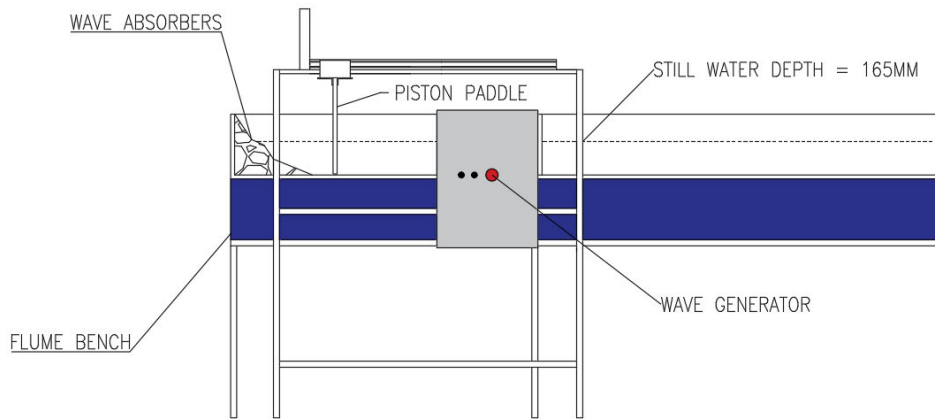


Figure 3-2: Piston paddle wave generator laboratory setup

For shallow water conditions: $\left(\frac{H}{S}\right)_{Piston} = K_p h$ (Dean and Dalrymple 1991). $\left(\frac{H}{S}\right)_{Piston} / K_p h$ is therefore governed by a linear relationship and is approximately equal to 1. H is therefore dependent on the stroke length (S), water depth (h) and the wave number (K_p). The S length was measured from the center of the piston paddle to the maximum displacement point from the paddle's starting position. H and L were measured manually in the lab by analyzing passing waves.

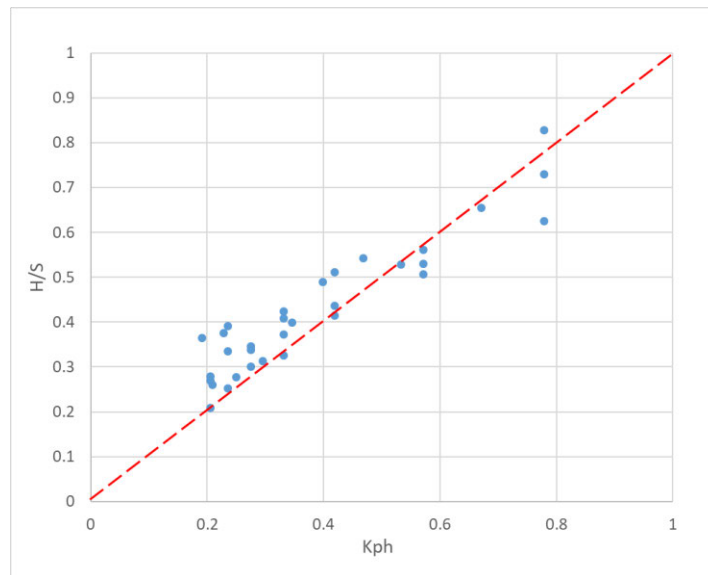


Figure 3-3: Non-Dimensional Relationship of H/S vs $K_p h$ for the piston paddle wave generator

The level of error between $\frac{H}{S} / K_p h$ was found to increase with an increasing wave height (H) (Figure 3-3). The data was sporadic and spread over the desired linear

relationship. It was further observed that increased levels of H led to higher degrees of reflection at either ends of the flume. Reflection either produces constructive or destructive interference within the flume due to seiche conditions. The effects of reflection are therefore undesirable for experimental conditions. The constructive and/or destructive wave interactions within the wave flume were observed further for varying wave heights (H) and wave periods (T).

A buoy-type mechanism was constructed to accurately measure the profiles of the waves produced by the wave generator within the flume (Figure 3-4). A high-resolution experimental camera was fixed to a tripod stand to record the artificial buoy movement. The camera recorded at 24 frames per second (Fps). A Python script was written to automate the acquisition and storage of the wave profiles pixel-displacement information. The OpenCV Python library was utilised to process image and video data in real time. Figure 3-4 displays the graphic user interface (GUI) output from the written Python script.

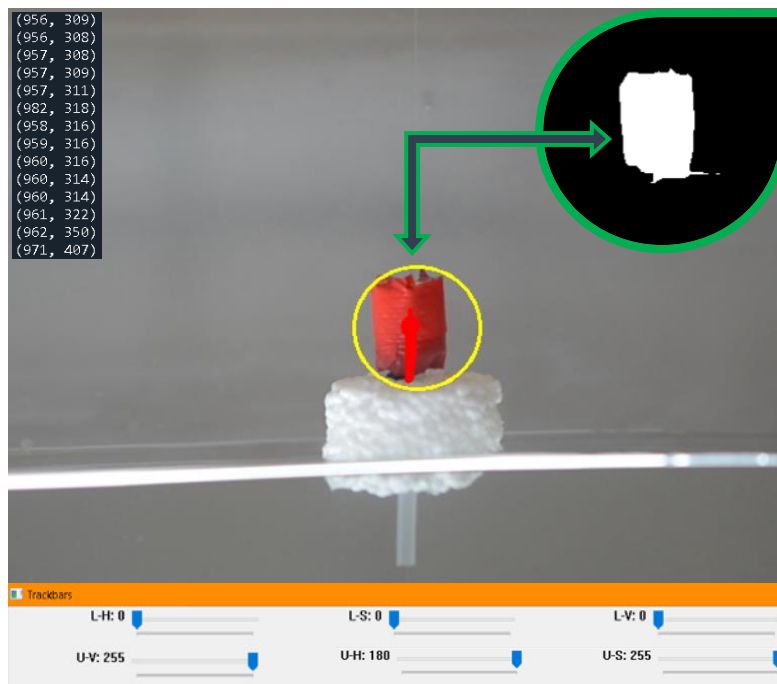


Figure 3-4: Python graphic interface tracking the pixel co-ordinates of the centroid of the buoy mechanism.

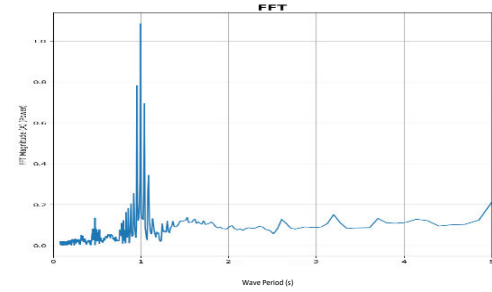
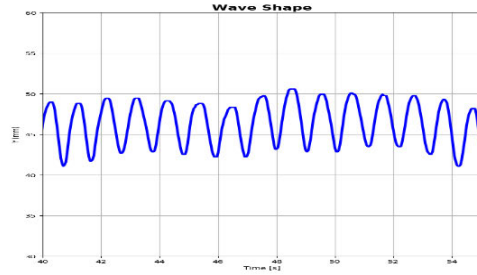
The script allowed a user to manually calibrate colour track-bars to trace the pixel coordinates (Figure 3-4: bottom) of the centroid of an object based on a desired colour.

Figure 3-4 (top right) indicates the masked Python output of the red buoy mechanism. Particle pixel-displacement information is recorded based on the centroid of this object. A calibration image was recorded to determine a conversion ratio between the displacement (mm) and the pixel coordinates (px). The conversion was implemented within the Python script. The center of the buoy mechanism was enclosed with a thin PVC pipe. Fine clear gut was laced through the center of the PVC pipe. The gut was tied to a clamp stand above the flume and weighed down at the bottom of the flume with an iron weight. The angle of the gut to the flume base remained perpendicular. The buoy mechanism remained suspended at the surface of the still water level (SWL). The model configuration allowed the buoy mechanism to move only vertically; with minimum friction between the buoy mechanism and the gut.

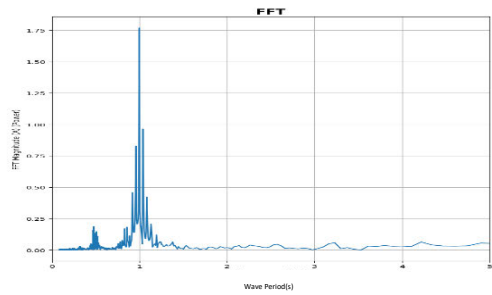
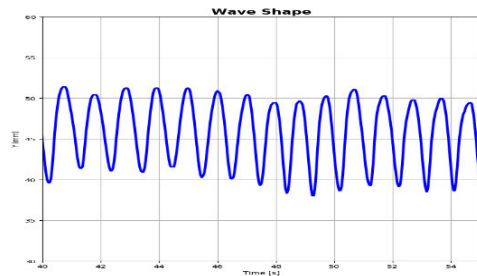
The wave generator was controlled remotely using Codesys. Codesys is a programmable logic controller (PLC) software tool that provides a platform to control automated technology in real-time. Codesys provided a graphic user interface (GUI) for the manual inputs of the wave period (T) and wave height (H) to the wave generator. The wave generator produces waves by automatically adjusting the paddle stroke length and duration of the paddle pulses/oscillations. Experiments were carried out for varying wave heights (Figure 3-5) and varying wave periods (Figure 3-6). The following experiments were carried out to test the validity of the waves produced in the flume; and how the inputted wave parameters (T and H) differ from the ones measured.

A uni-directional wave spectrum can be described as a composition of an infinite series of harmonic sine waves of varying amplitudes and frequencies (Reeve, Chadwick, and Fleming 2012). Spectral analysis can be used to analyze noise-like signals and provide the frequency decomposition in harmonics. The spectral density function for a discrete time record can be described mathematically through the Fourier series by utilizing the fast Fourier transform (FFT) algorithm. FFT converts wave form data in the time domain into a frequency domain. The FFT function diverges/spikes to indicate the location of the wave period from analyzed waveform data (Figures 3-5 and 3-6). The wave amplitude (a) can be derived from the FFT magnitude/power spectrum.

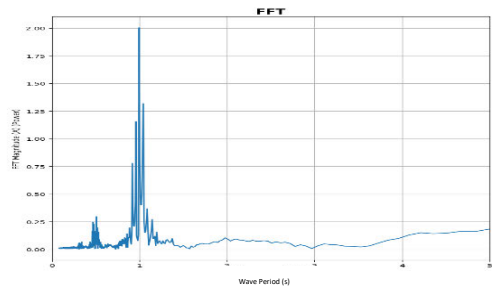
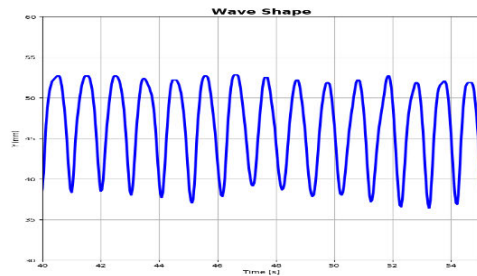
A)
 H = 20 mm
 T = 1 second



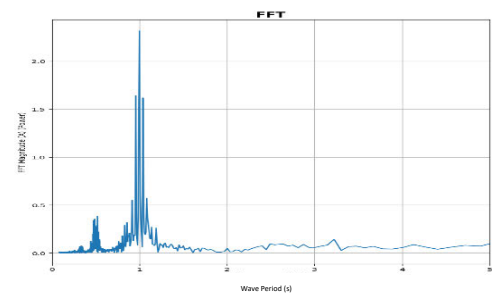
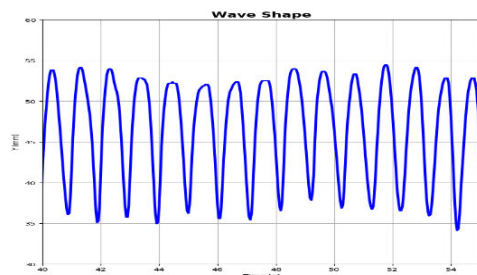
B)
 H = 30 mm
 T = 1 second



C)
 H = 40 mm
 T = 1 second



D)
 H = 50 mm
 T = 1 second



E)
 H = 60 mm
 T = 1 second

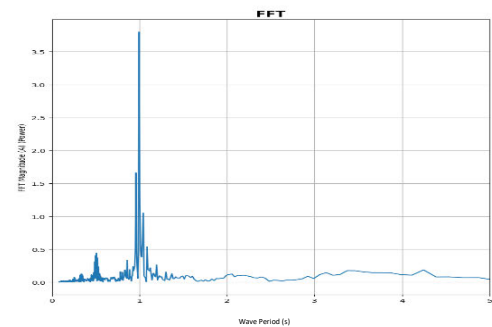
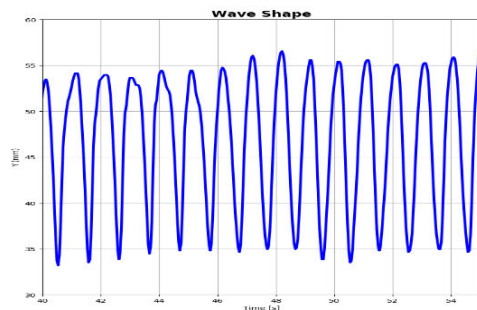
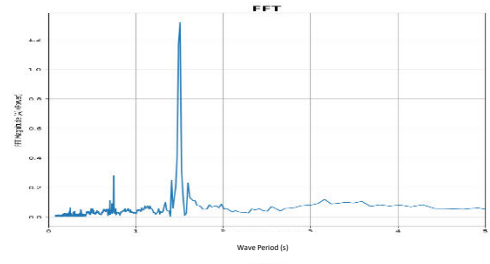
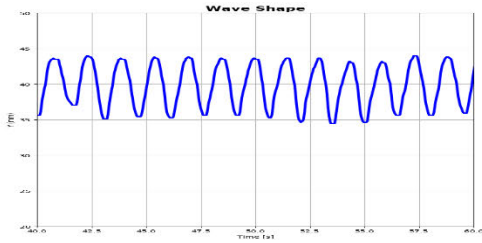
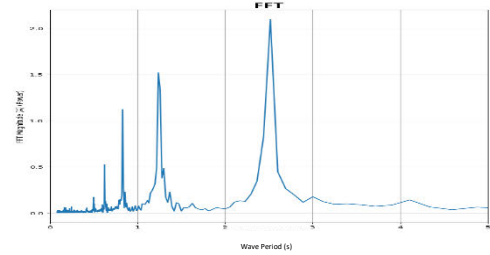
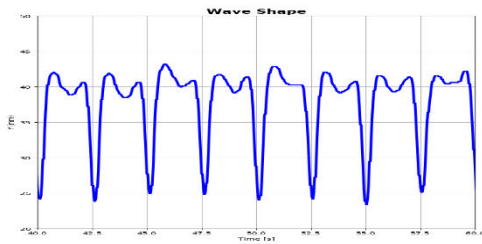


Figure 3-5: Experiment 1: Varying the Wave Height (H). The wave spectrum per experiment (Time (s) vs. Vertical position (Y (mm)). FFT data displayed as the wave period (T (s)) vs. magnitude/power.

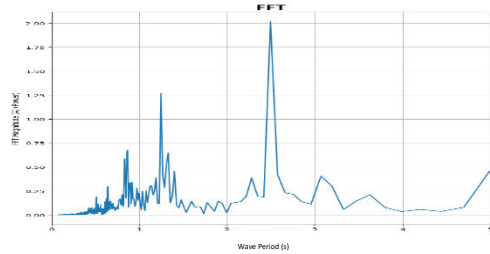
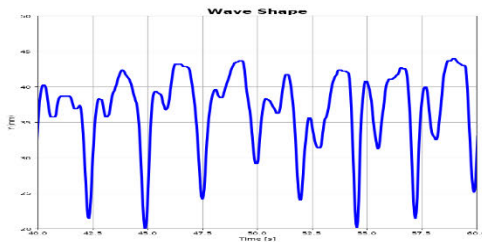
A)
T 1.5 seconds
H30mm



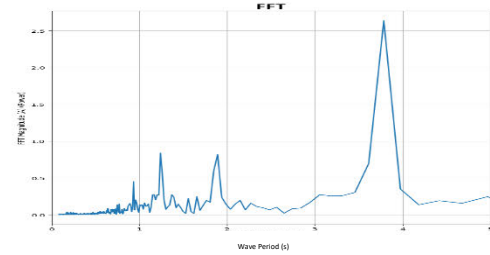
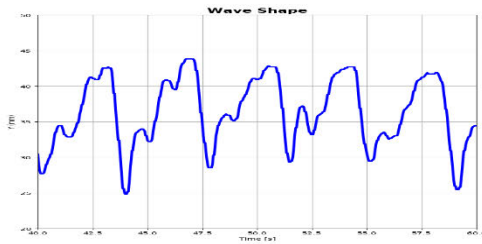
B)
T 2 seconds
H30mm



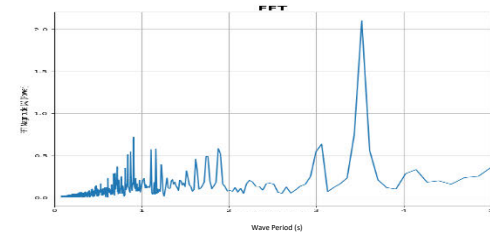
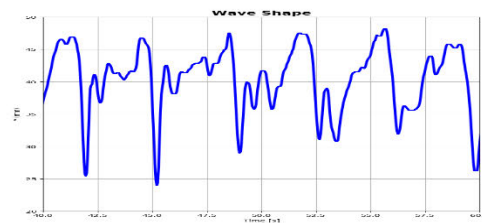
C)
T 2.5 seconds
H30mm



D)
T 3 seconds
H30mm



E)
T 3.5 seconds
H30mm



F)
T 4 seconds
H30mm

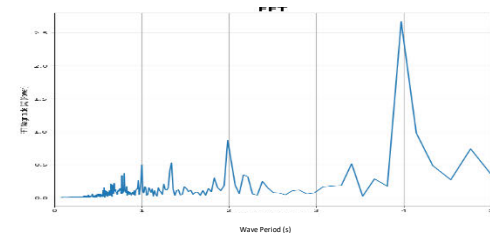
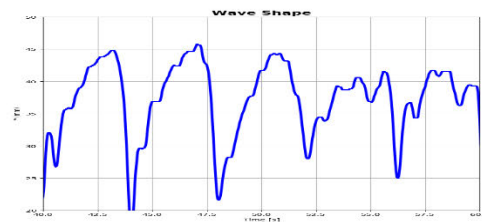


Figure 3-6: Experiment 2: Varying the wave period (T) The wave spectrum per experiment (Time (s) vs. Vertical position (Y (mm)). FFT data displayed as the wave period (T (s)) vs. magnitude/power.

The buoy mechanism was placed 2 meters away from the incident wave paddle to maintain a close proximity over the 15 meter wave flume and to minimise the immediate effects of wave reflection. To restrict the loss of wave energy through seepage the paddle was sealed around its perimeter to ensure no leakages.

For Experiment 1 (Figure 3-5), the wave period (T) remained fixed and the wave height (H) was varied. The wave profiles (A-E) are observed to remain relatively sinusoidal; however, the desired wave height input was not achieved. As waves propagate downstream in the flume wave energy is lost due to gravity and friction from the flume walls. Low period waves were found to decay substantially as they propagated downstream. For Experiment 2 (Figure 3-6), the wave period (T) was varied and the wave height (H) remained fixed. It is observed that with a gradual increase in the wave period the wave profile becomes less sinusoidal. Under shallow water conditions waves produced in a flume give rise to both cnoidal and sinusoidal waves. Sinusoidal waves will have equal trough to crest lengths and heights; whereas cnoidal waves will have longer, and shallower troughs in comparison to their crest. Variations in the wave profiles can be further attributed to a secondary wave present within the flume. The effects of the secondary wave became more influential with an increase in the wave period (Figure 3-6). The secondary wave condition could be due to either constructive or destructive wave interference due to seiche conditions; or to pre-existing errors in the automated Codesys PLC program in which wave reflection was not considered.

Investigation into a corrective wave equation was investigated in Python (Figure 3-7). This investigation aimed to provide a wave equation which could be applied to Codesys in order to achieve the desired sinusoidal wave outputs. However the approach became more stringent under the effects of the secondary wave at varying wave periods. From experiments 1 and 2, the wave generator inputs did not match the measured wave outputs which was undesirable for future experiments. Due to these experimental limitations, the results of this experiment led to the formation of an idealised FPB model. An idealised physical FPB model was designed and built to measure the effect of an idealised wave pressure over the length of the flexible tube to simulate a single pulse sinusoidal wave.

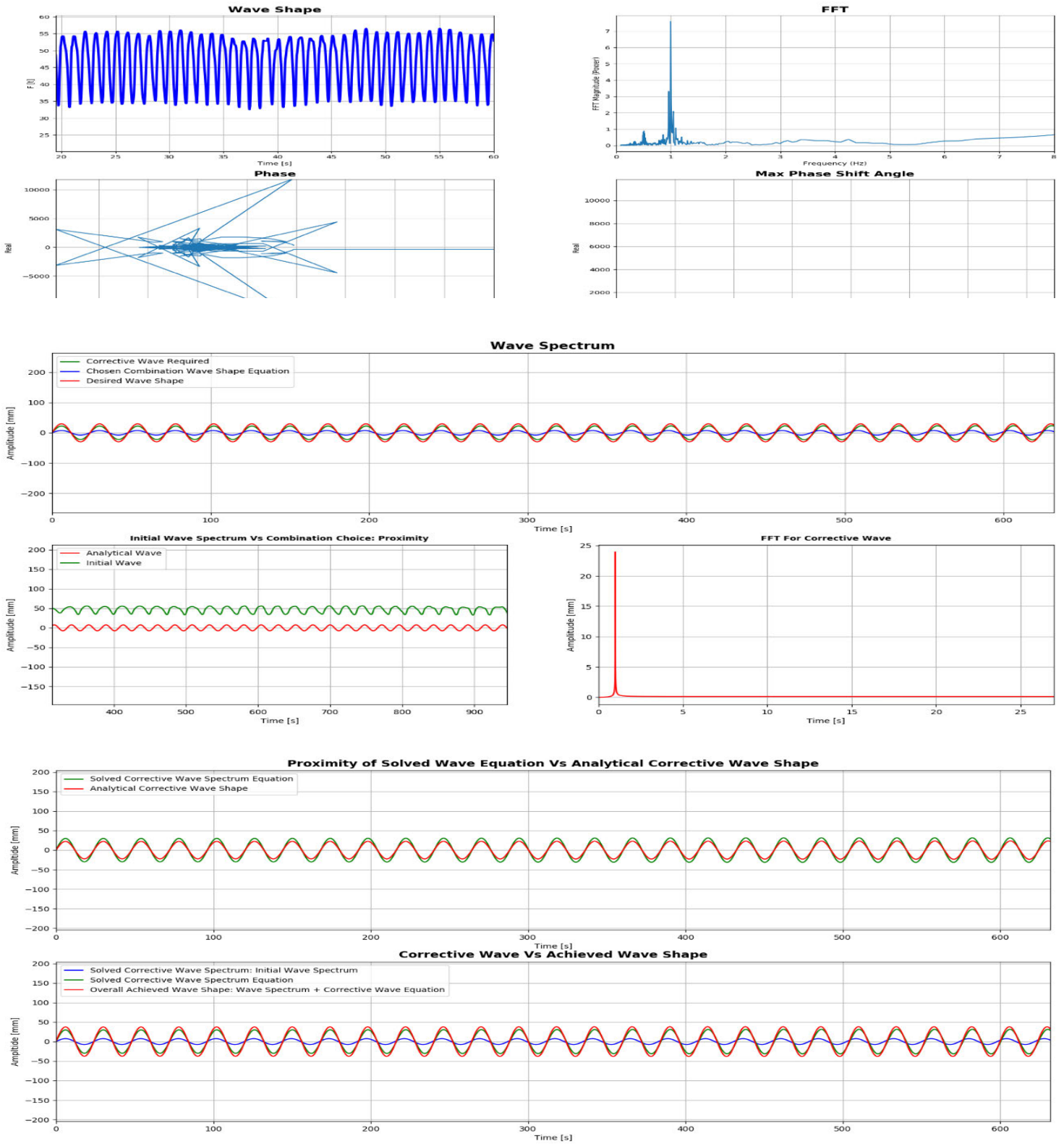


Figure 3-7: An extract from the establishment of a corrective wave of $T = 1$ H = 60 mm in the wave flume

3.1 FLOATING FLEXIBLE BIOREACTOR MODEL

In a typical FPB system wave pumping creates a continuous flow in the tube. A boundary layer develops that interacts with the transient flow pulses driven by the waves. The boundary layer profile depends on the degree of pumping. An idealised FPB model is designed and constructed to generate a repeatable sinusoidal pulse wave within the flexible tube. The idealised FPB model further mitigates/minimises the effects of constructive and/or destructive wave reflection within the flume; and limits the flexible tube length to minimise the effects of tube-sway/energy loss on the internal flow. An idealised pulse wave is able to retain its energy downstream and ignores the effects of downstream wave energy decay present in a wave flume FPB model. The idealised experimental model can be repeated for future experimental research.

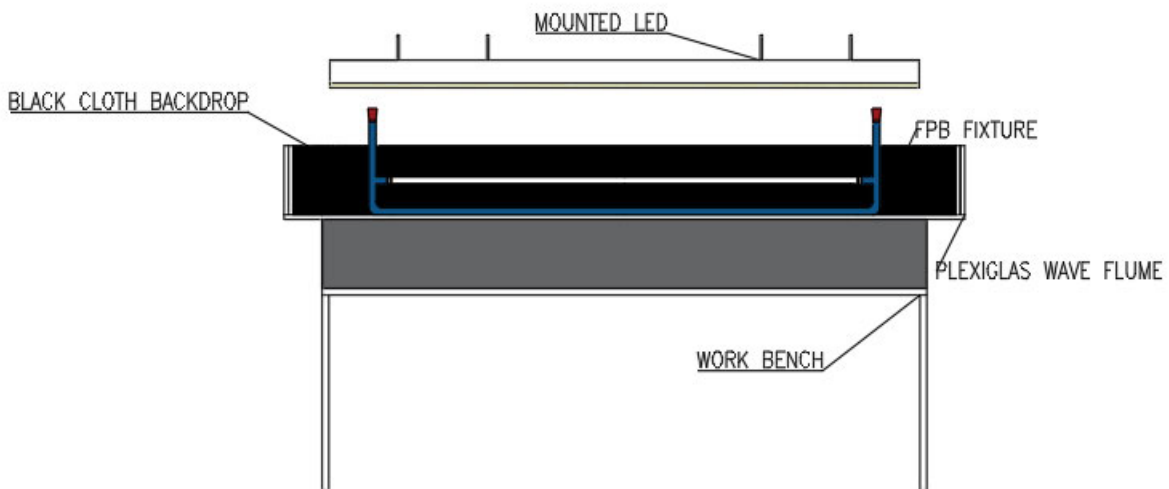


Figure 3-8: Experimental FPB model configuration within a wave flume

Experiments were conducted in a laboratory flume. The flume is comprised of a clear Plexiglas material with an internal height of 450mm, a width of 400mm and a length of 3000mm. For the purpose of PIV monitoring; a high powered light-emitting diode (LED) is mounted above the wave flume and remains fixed at the center of the flume throughout all experiments. This ensures a continuous light stream (20mm thick) over the experimental field of interest. The LED is run using Drew Lear software which allows for the manual inputs of the LED pulse rate, light intensity, and pulse strobe pattern.

A flexible photobioreactor (FPB) model is constructed and placed centrally within the wave flume to directly lie below, and inline to the LED fixture (Figure 3-8). The light stream therefore overlays and illuminates the transparent flexible tube generating a large potential investigative area. A black cloth backdrop is placed behind the flume to ensure limited light reflection.

The FPB model consists of a rigid and clear PVC system (Figure 3-9). Attached to its center is a clear flexible polyethylene tube. The flexible tube is used to mimic a flexible photobioreactor (FPB). Transparent materials were used to construct the FPB model to limit the light absorption and refraction from the LED. The FPB model lies on the bed of the flume. The still water level (SWL) of the flume is fixed at 100mm, this is equal to the height of the polyethylene tube on the FPB fixture. The FPB model is filled to match the SWL; thus ensuring a zero pressure gradient. A zero pressure gradient limits potential restrictive forces and allows for a smooth and continuous flow within the FPB model.

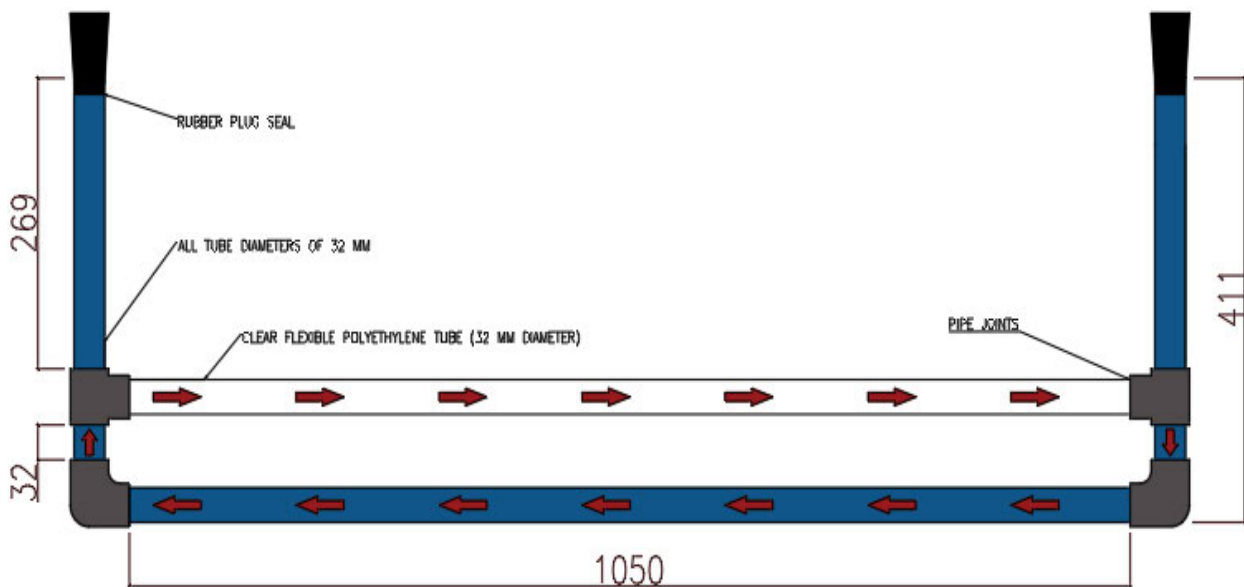


Figure 3-9: FPB model showing the continuous flow direction assuming a wave moves from left to right

Comparable to peristaltic motion; the flexible tube will expand and contract under induced external pressures. A change in the cross-sectional area of the flexible tube walls causes the fluid to be displacement resulting in an internal fluid motion. The FPB model is designed to enclose and isolate the flow within the FPB fixture (Figure 3-9). This allows

for the independent and continuous flow between the FPB's internal fluid flow and the motion of the wave flume's medium. The FPB enclosure thus allows for the internal flow to remain continuous and isolated.

To simulate an external wave pressure, a transparent roller system is fixed to the FPB model in which the roller profile aims to mimic a propagating waveform along the length of the tube by inducing a pressure constriction (Figure 3-10). The roller is manually moved laterally at a constant speed to simulate a single and idealised propagating pulse wave moving along a single boundary of the flexible tube.

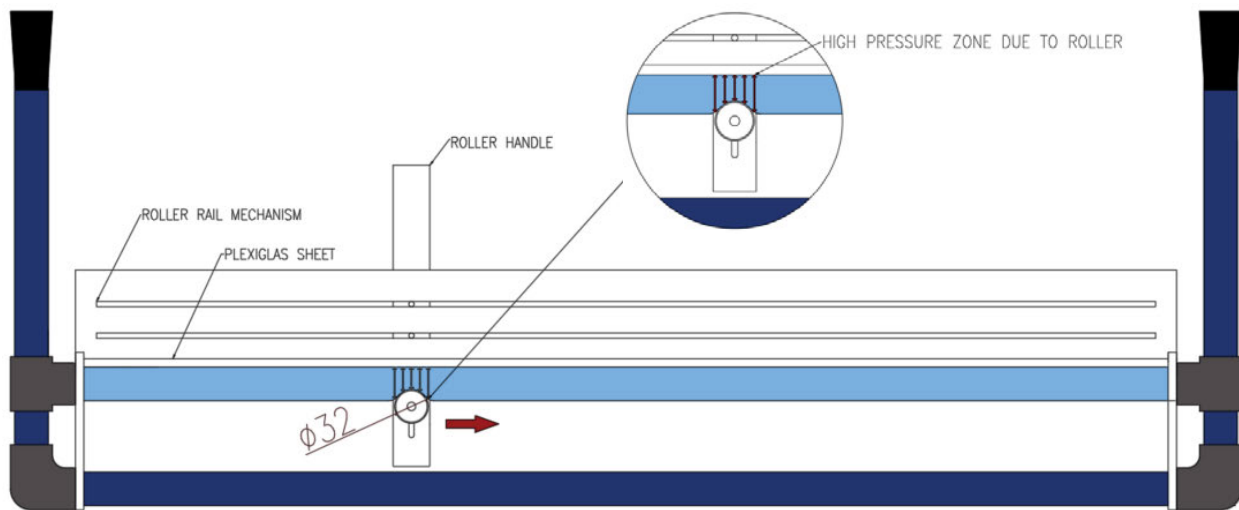


Figure 3-10: FPB model with the roller mechanism attachment. The roller moves from left to right.

The roller mechanism is comprised of a clear and smooth PVC roller. This was done to limit the level of friction between the flexible tube and the roller mechanism. A flat sheet of Plexiglas is fixed to the upper end of the roller stand to restrict the upward swaying of the flexible tube (Figure 3-10). The upper boundary layer of the FPB sits against this sheet thus, restraining the flexible tube to any transverse motion (in the direction of the applied force). This limits the potential loss in energy by confining any tube movement to the isolated roller pressure. The roller mechanism is attached to a Plexiglas roller handle which slides along a rail system acting parallel to the length of the flexible tube. The Plexiglas handle ensures the mechanism is optically noninvasive. The roller mechanism is designed to apply a constant/fixed vertical constricting force on the flexible tube; and

moves horizontally applying a constant pressure force along the length of the tube's lower boundary layer.

Under an induced roller pressure, the upper boundary of the flexible tube pushes against the Plexiglas sheet. The roller applies a pressure directly to the flexible tubes lower boundary layer causing a deformation in the tubes cross-sectional area. The roller moves along the length of the flexible tube simulating one pulse wave per tube length. The roller mechanism idealises an external wave pressure force on the bottom layer of the tube's boundary. This investigation aims to observe the flow characteristics within the FPB as a result of the applied localised roller force.

Clamps were designed to attach the FPB model to the flume walls. This rigid structure ensures that, under the effects of the roller motion, the FPB model does not shift or jerk and therefore limits potential energy losses. The FPB system is positioned centrally to align with the light stream from the overhanging LED. This is to ensure that the flexible tube remains illuminated throughout all experimental processes. The flexible tube succumbs to both expansion and contraction. The diameter of the flexible tube therefore varies in the X and Y direction under an external pressure force. The diameter ratio (D_R) can be represented by:

$$D_R = \frac{D_x}{D_y} \quad (26)$$

Where D_x is the diameter on the X-plane, from the axial center; and D_y is the diameter on the Y-plane from the axial center.

3.2 NON-INVASIVE OPTICAL TESTING

Experimental conditions must be optically non-invasive to ensure the effective illumination of micro-balloon fluid tracer particles (Steenbergen 1996). The experimental configuration must therefore aim to limit the potential light refraction between the FPB tube and water medium due to the LED intensity. By restricting the level of light refraction one can improve the quality of the PIV pixel information recorded, and thus improve the overall accuracy of the flow visualisation. The refraction of light between liquid-solid interfaces of

model section walls is a common difficulty (Budwig 1994). Light distortion is further enhanced due to the curvature of pipe walls (Steenbergen 1996).

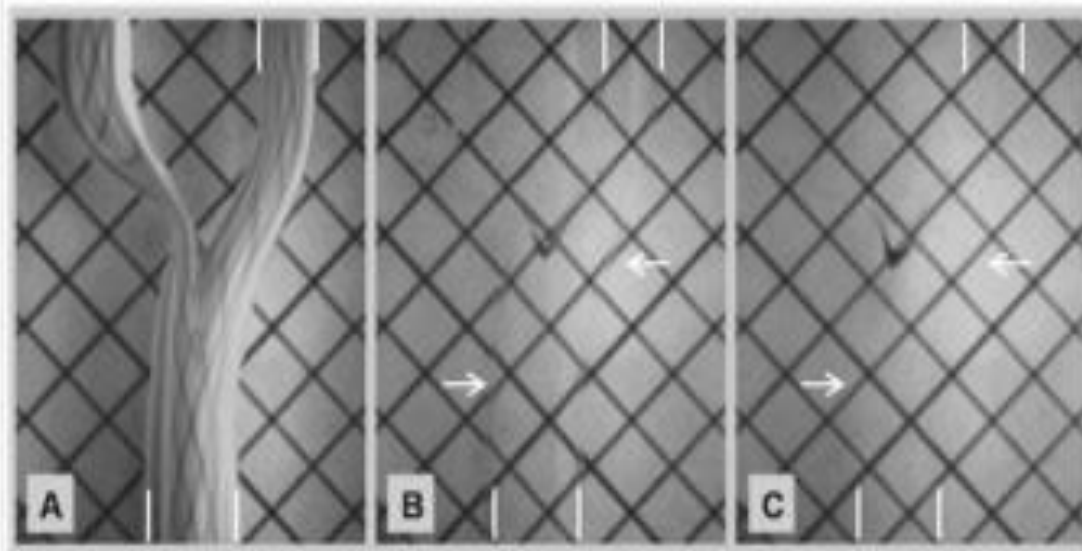


Figure 3-11: Visual monitoring method used by (Yousif, Holdsworth, and Poepping 2010) to investigate the effects of matching refractive indices between the liquid and tube mediums

A method of limiting light refraction includes refractive index matching between the test fluid and the flexible tube medium (Yousif, Holdsworth, and Poepping 2010). Investigation into the effects of light refraction between the FPB and the water medium is determined by following the Amsler grid method used by (Yousif, Holdsworth, and Poepping 2010) (Figure 3-11). The grid is used as a visual diagnostic tool to aid in the detection of optical density changes. The Amsler grid comprises of a grid of vertical lines which are used to monitor imperfections in the visual field. The FPB is made of polyethylene with a general refractive index (n) of 1.49979 and is fully submerged in a water medium with a n of 1.33 ($20^{\circ} C$). The Amsler grid is used to determine whether there is a visual distortion problem due to the variance in refractive indices.

The FPB model is placed in a wave flume. The model is filled with the water medium to an equal level as the SWL of the flume. The FPB tube is positioned directly under the LED light sheet. The Amsler grid is placed behind the tube. A monochromatic experimental camera filming at 5120 x 2500 pixels was used to monitor the tube's motion.

A camera acquisition rate of 120 frames per second (Fps) was chosen to limit the likelihood of blurred images due to the tubes motion. The tube is manually swayed up and down. It was observed that the grid lines remained undistorted and visually stable. The refractive index difference between the polyethylene tube and the water was therefore noted to be optically non-invasive.

Upon inspection of the experimental image sets it was found that numerous impurities were present within the tube's enclosure (Figure 3-12 A). It was observed that air-bubbles attached themselves to the boundary layer of the tube's walls.

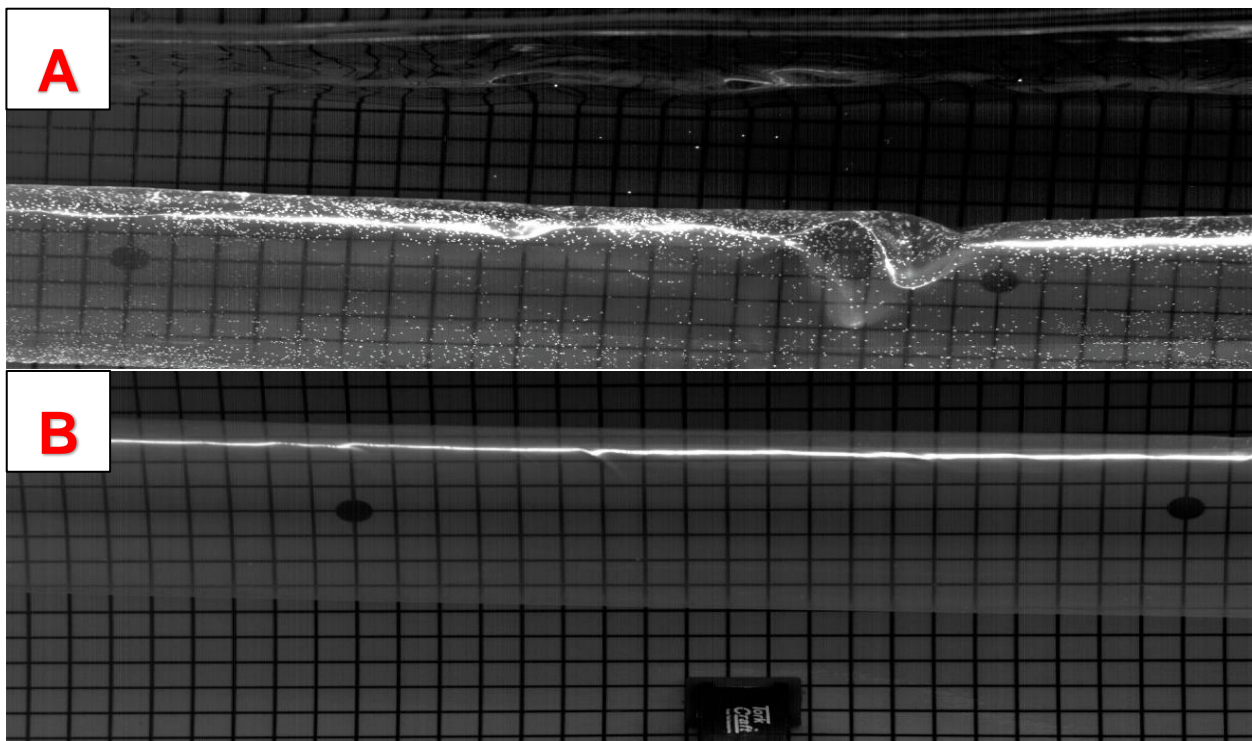


Figure 3-12: Air-bubble impurities present before (A) and after (B) optically enhancing the experimental conditions. Amsler grid placed behind the FPB tube.

Variations between the refractive indices of both air and water, 1.003 and 1.49979 respectively, generated increased light refraction within the flexible tube. Light refraction was further enhanced in regions of tube deformation due to the clumping of air-bubble impurities within these zones. The presence of impurities therefore posed a high risk toward masking particle displacement information and ultimately decreasing the overall accuracy of PIV rendering.

To limit the presence of optically invasive impurities the water was boiled before being poured into the FPB enclosure. The boiled water allowed for the air-bubbles to rise and dissipate before entering the FPB model. The FPB was filled using a funnel attached to a long flexible tube. The tube was pushed to the bottom of the FPB fixture. A foam layer was placed over the opening of the funnel to further dissipate the force of the pouring flow and to limit the formation of air-bubbles. The FPB tube was further tapped to ensure that any residual air bubbles would rise to the surface and dissipate when exposed to the open atmosphere. This approach greatly reduced the presence of air-bubbles impurities within the FPB enclosure (Figure 3-12 B).

3.3 OPTIMAL FIELD OF VIEW CALIBRATION

Fluid particle motion was filmed using a Mikrotron 25CXP monochromatic EoSens camera. The camera has a maximum resolution of 5120 x 5120 pixels. The cameras acquisition rate varies based on the desired resolution. Manual decreases in the resolution allow for increases in the applicable acquisition rates. To improve the accuracy of the PIV measurement, the cameras acquisition rate must be higher than the maximum observed particle displacement in order to avoid potential particle blur streaks. Blurred images decrease the accuracy of the instantaneous velocity measurement in PIV.

PIV is heavily reliant on the efficient illumination of the tracer particles within the fluid flow field. An optimal particle size in relation to the camera resolution must be established. Lowering the particle size improves flow tracking while increasing its size improves light scattering under illumination (Hadad and Gurka 2013). To enhance the accuracy of velocity measurements, both the type and size of the particles are crucial. A uniform particle size is required to provide a high signal to noise ratio (SNR); thus enhancing the accuracy of the velocity field measurement (Hadad and Gurka 2013). Tracer particles should be spherical to minimize the effects of drag, and be of similar density to the fluid to ensure neutral buoyancy; this increases the particles ability to follow the flow. Particles should further have a higher refractive index than the fluid medium to ensure that light will be efficiently refracted. Available microspheres were measured using a master sizer 2000. The average diameter was determined to range between 60-80 μm .

3.4 PIV PARTICLE PARAMETERS

To determine the optimal resolution conditions for the experimental set-up an analytical investigation was done (Table 3-1). The investigated parameters aimed to prescribe the optical experimental conditions required to provide sufficient pixel information for PIV rendering. According to (Kompenhans et al. 1999) optimizing spatial resolution techniques include:

- Using the smallest possible working distance
- Allocating a high-quality objective lens with a low aperture number
- Allocating a small pixel size and large frame rate

The experimental field of view (FOV) must capture the full range of fluid motion within the tube under roller compression. The maximum vertical FOV is therefore chosen to exceed the diameter of the flexible tube (32mm) in Table 3-1. The corresponding maximum horizontal FOV is established based on the allowable camera resolution limit corresponding to a 120 Fps acquisition rate. The camera was subsequently allocated a 3000 x 5120 pixel resolution, allowing for a 26 x 45 mm FOV respectively. Analytically this provided a sufficient pixel resolution for a microballoon size of 70.31 μm which fell between the average microballoon diameters of 60-80 μm (Table 3-1). The experimental camera was setup under the prescribed conditions and the image sequence was recorded.

MATLABs image inspection tool was used to extract the 'Measured Parameters' (Table 3-1 and Figure 3-13). Pixel measurements were taken in the image viewer tool to validate whether the analytical parameters matched the measured ones (Table 3-1 and Figure 3-13). It was observed that the actual pixel resolution became 2992 x 5120, which corresponded to a 22.54 x 38.57 (mm) FOV.

Table 3-1: Analytically derived parameters to provide sufficient pixel resolution per particle vs measured parameters. Recommended particle sizes and FOVs are highlighted in green.

CAMERA PROPERTIES:	Analytical Parameters:	Measured Parameters:
Vertical (px):	5120	5120
Horizontal (px):	3000	2992
Field of View Properties:		
Corresponding vertical FOV (mm):	45	38.57
Corresponding Horizontal FOV (mm)	26.37	22.54
Vertical Ratio: 1 px : ___ mm	0.009	0.008
Vertical Ratio: 1 mm: ___ px	113.78	131.28
Horizontal Ratio: 1 px: ___ mm	0.009	0.008
Horizontal Ratio: 1 mm ___ px	113.78	131.28
Outputs:		
Allocated pixels per particle image requirement (Inputted):	8	+3
Required microballoon diameter per pixel requirement (μm):	70.31	68.56
Final Field of View Parameters:		
Vertical FOV (mm):	45	39
Horizontal FOV (mm):	26.37	22.79
Required Microballoon Size per pixels per Particle Size (μm):	70.31	68.56

Analytically a 9 pixel per particle resolution was allocated (Table 3-1). However, upon the manual measurement of particle information, in MATLABs image viewer, the majority of particles were given a 3 pixel per particle resolution (Figure 3-13). According to Thielicke and Sonntag 2021 the minimum allowable particle image diameter is 3 ± 1 pixels and a particle density of 5-15 particles per interrogation area is recommended. For the optimal fluid flow acquisition in PIV, at least 6-8 particle images are required per interrogation area, this limits false vectors to a minimum error (Kompenhans et al. 1999). The measured particle sizes proved applicable as they lied within the minimum requirements for PIVlab (Thielicke and Stamhuis 2014b). At a 3 pixel particle diameter the seeding concentration must be $\geq 25\%$ the total medium volume and consist of an interrogation window of no smaller than 14 x 14 pixels (Kompenhans et al. 1999).

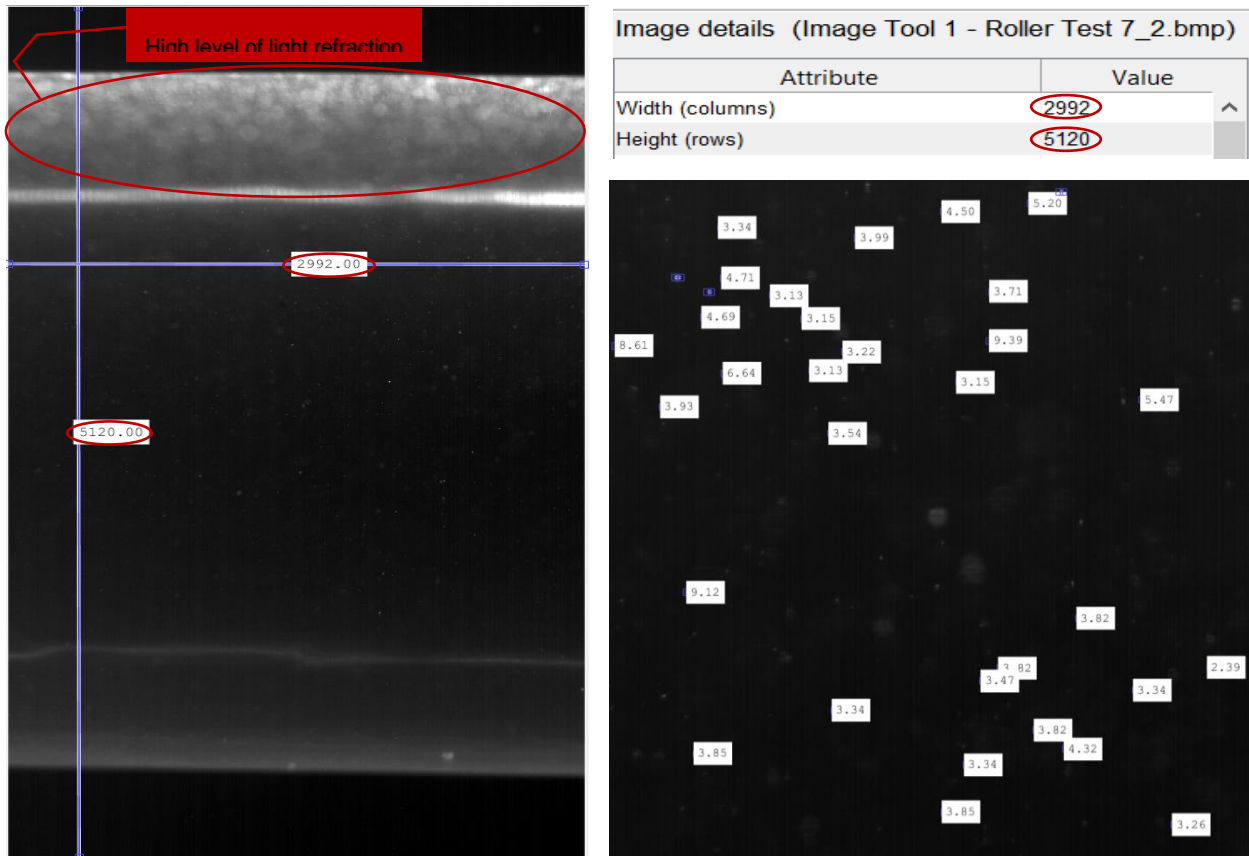


Figure 3-13: Pixel image information derived from MATLAB Image viewer

Based on the maximum allowable pixel resolution the camera's acquisition rate was set to 120 Fps. This allowed for a clearer image sequence of the flow; as particle displacement becomes more observable at smaller intervals. Increases in the acquisition rate further reduces the susceptibility of image motion blur thus providing a clearer representation of fluid pattern. By using Drew Lear (LED software tool), the laboratory's high powered LED was set to an auto-correlation function. The LED strobe pulse rate was calibrated to match the camera's acquisition rate at 120 Hz. This ensured that particles were effectively illuminated at every consecutive image capture. The LED was further set to a light intensity of 100% to ensure particles are subject to sufficient light refraction between image sequences.

The accuracy of PIV rendering is heavily reliant on the effective illumination of particle tracers. The curvature of the tube walls generated high-intensity light refraction zones

(Figure 3-13). High contrast regions hide illuminated particle movement, thus making particle displacement information in these zones unobservable for PIV rendering. Light refraction was found to be more prominent in the upper region of the tube boundary layer (Figure 3-13). This could be due to tracer particles not being truly neutrally buoyant and rising to the tube's upper boundary layer. To negate these regions for PIV rendering, a mask filter is applied within PIVlab (Figure 3-14).

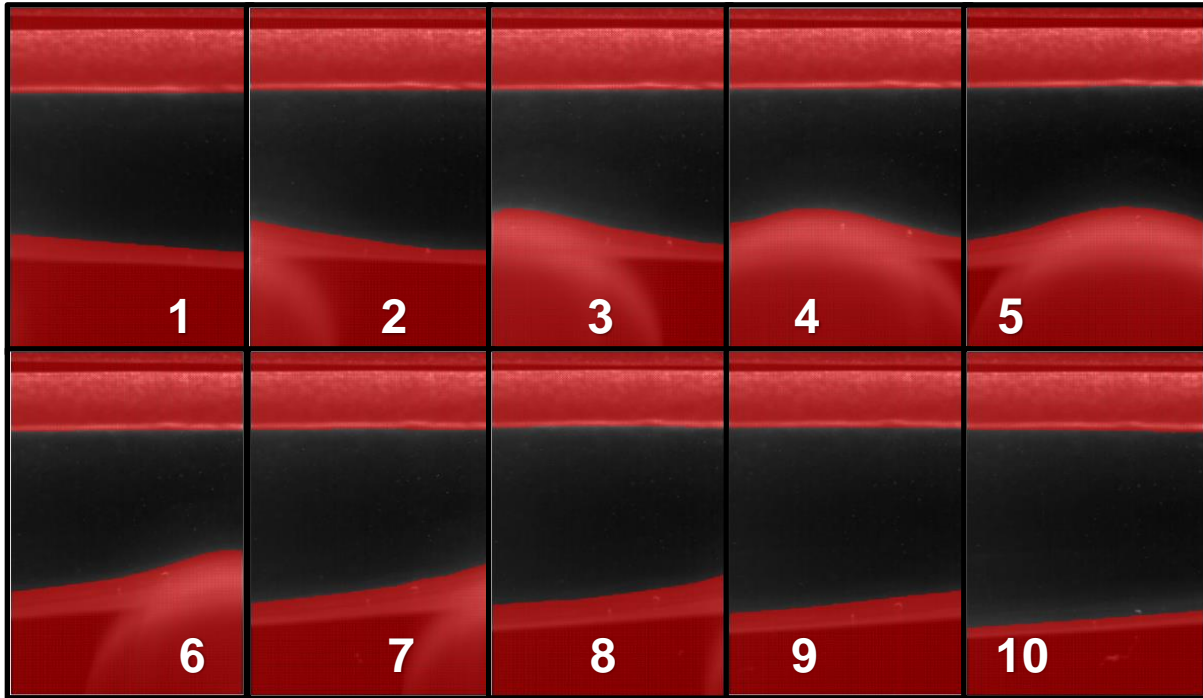


Figure 3-14: control volumes 1-10 of the PIVlab masked regions (red) as the roller mechanism moves from left to right.

A region of interest (ROI) is established where the roller mechanism and upper tube boundary layer are masked (Figure 3-14). This allowed for the independent analysis of the flow within the tube and limited the susceptibility of invalid vectors.

Table 3-2: Manually set PIVlab's image pre-processing settings

Image Pre-processing Settings:	
CLACHE (Window size [px]):	20 px
Highpass (Kernel size [px]):	15 px

Intensity Capping:	Enabled
Wiener2 Denoise and low pass (Window size [px]):	10 px
Auto contrast stretch	Enabled between 0-0.702

Table 3-3: Manually set PIVlab's Image-evaluation settings

Image-Evaluation Settings:	
PIV Algorithm:	FFT Window deformation
Pass 1 and step [px]:	256 [px] with 128 [px] step
Pass 2 and step [px]:	128 [px] with 64 [px] step
Pass 3 and step [px]:	64 [px] with 32 [px] step
Pass 4 and step [px]:	32 [px] with 16 [px] step
Sub-pixel Estimator:	2D Gaussian (9 point)
Correlation Robustness:	Standard
Calibration Ratio:	1 [px]: 7.53×10^{-6} [m]
Time step [ms]:	8.33

Table 3-4: Vector Validation Settings

Vecotor Validation Settings:	
Velocity scatter distribution limits refined	Manually inspected
Standrad deviation filter threshold [n*stdev]	7
Local median filter threshold	5
Missing Data	Interpolated

Image pre-processing calibrations were investigated visually (Table 3-2). Each aspect was applied individually and the image enhancements were observed. Final settings were allocated based on the effectiveness of enhancing particle clarity and the overall optimal lighting conditions within the FOV.

Image-evaluation settings were assigned in accordance PIVlab's validations. The Pass 1 interrogation window and step size allocation are based on achieving an initial

interrogation window size of at least four times the size of the largest particle displacement (Thielicke and Sonntag 2021); a horizontal and vertical offset (step) of 50% further confines any possible rapid particle displacement to the same interrogation area under the FFT algorithm (Thielicke and Stamhuis 2014). Four passes were run to improve the overall quality of the velocity flow measurement; as each interrogation area is refined under each pass applied, thus yielding a high spatial resolution, dynamic velocity range and signal to noise ratio (Thielicke and Stamhuis 2014). A Gaussian 2D sub-pixel estimator proves to work better under flow conditions subject to shear and rotation as well as possible motion blur (Thielicke and Stamhuis 2014). Based on computational power, a bilinear interpolation (standard correlation robustness) proved the best option for PIV rendering.

Outliers are common within PIVlab. Resultant vectors maps are therefore recommended to be evaluated manually in order to set velocity limits to better refine the data set and to interpolation of valid data. Velocity limits can be set by confining grouped regions of data to eliminate velocity outliers (Figure 3-15).

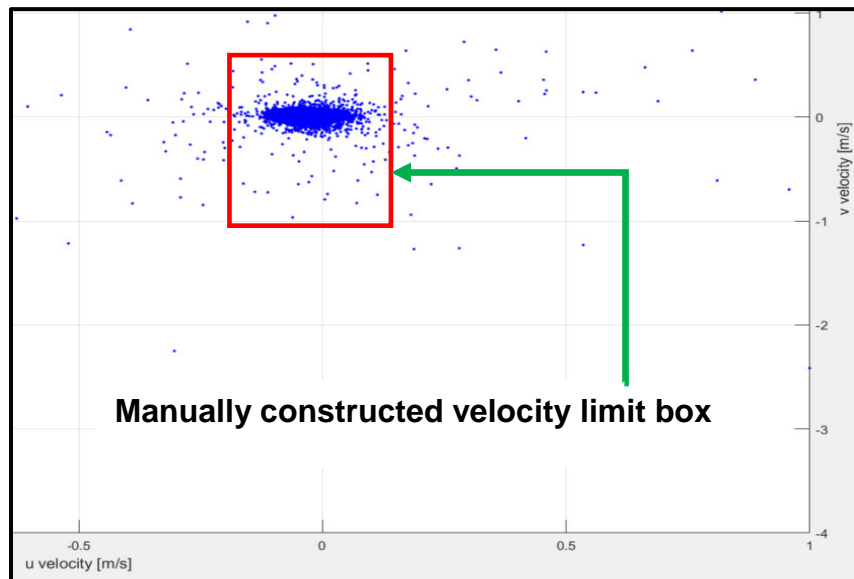


Figure 3-15: Setting velocity limits within PIVlab

The roller mechanism's movement is measured using Blender software (Figure 3-16). Blender allows for the independent motion tracking of a desired object between image pairs (Figure 3-16). The roller mechanism was verified to move over the tubes lower

boundary at a constant rate (Figure 3-16). The roller profile was tracked over consecutive image pairs to establish a mean roller speed. The mean roller speed was found to be 0.466 m/s.

The roller mechanism provides a single idealized wave pressure which runs along the length of the FPB. As the roller moves from left to right against the tube's lower boundary layer, it applies an external pressure on the tube. A reduction in the cross-sectional area of the tube generates an internal collapsible flow within the FPB (Grotberg and Jensen 2004). The magnitude and frequency of the fluctuations in the cross-sectional area, are directly related to the magnitude of the induced internal flow (Pedley and Pihler-Puzovic 2015).

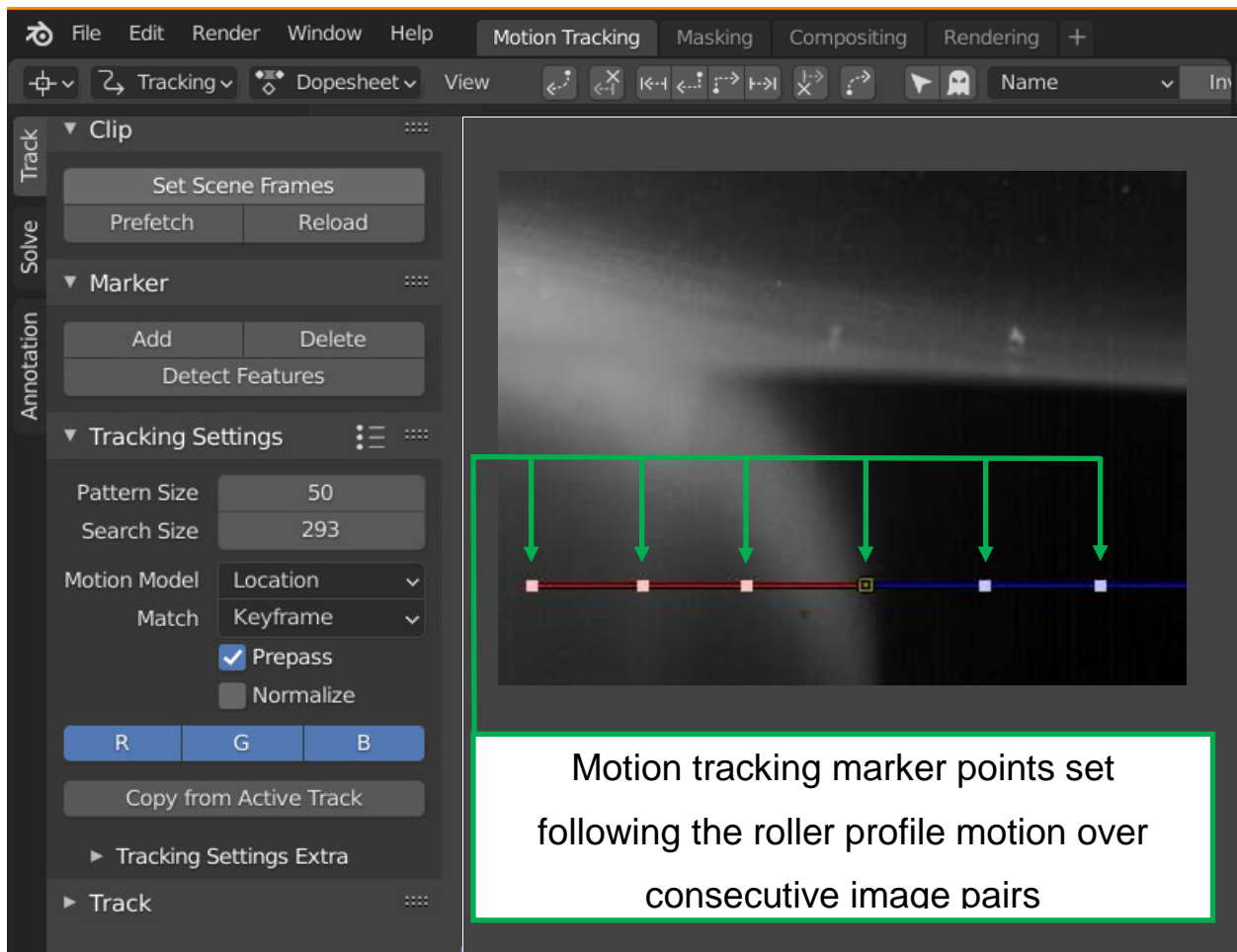


Figure 3-16: Blender GUI: Tracking the roller speed

CHAPTER 4: RESULTS AND DISCUSSION:

The application of the roller on the lower boundary of the FPB generates a transfer in pressure. The variations in internal pressure within the FPB displaces the internal fluid structure. The fluid motion is observed within PIVlab and particle pixel-displacement information is extracted. Raw PIVlab pixel-displacement data is extracted as ASCII text files carrying displacement and velocity information per IA over all CVs. Python software is an open-source programming tool that provides a platform on which to reorganize, store and manipulate raw data, allowing for the extraction of further characteristics of the flow. A Python script was designed and written to extract, store, calculate and depict PIVlab velocity and displacement information automatically for all experimental sets. Raw displacement data is transferred to Python and further characteristics of the flow are investigated. The roller moves from left to right against the tube's lower boundary. In the horizontal X-plane: right is positive and left is negative; in the vertical Y-plane: upwards is positive and downwards is negative.

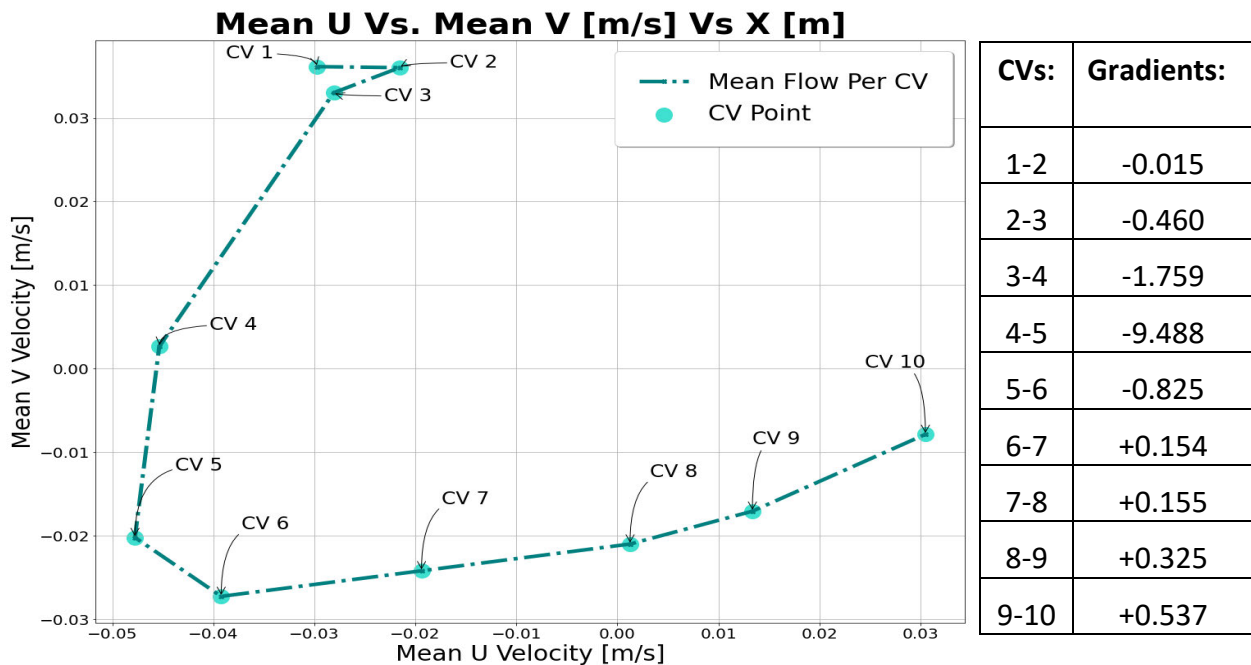


Figure 4-1: Mean fluid flow pattern over CVs 1-10 due to the direct influence of the roller on the tube's lower boundary

U and V velocities represent both the horizontal and vertical velocity components respectively. Observations are made over a series of 10 consecutive control volumes (CVs) in which the roller mechanism enters and exits the field of view (FOV) (Figure 26). The roller mechanism applies an external pressure on the FPBs lower boundary which displaces the fluid within the FPB. The internal fluid structure is observed. The mean velocity changes per CV indicate the average fluid trajectory over the investigation (Figures 4-1 and 4-2).

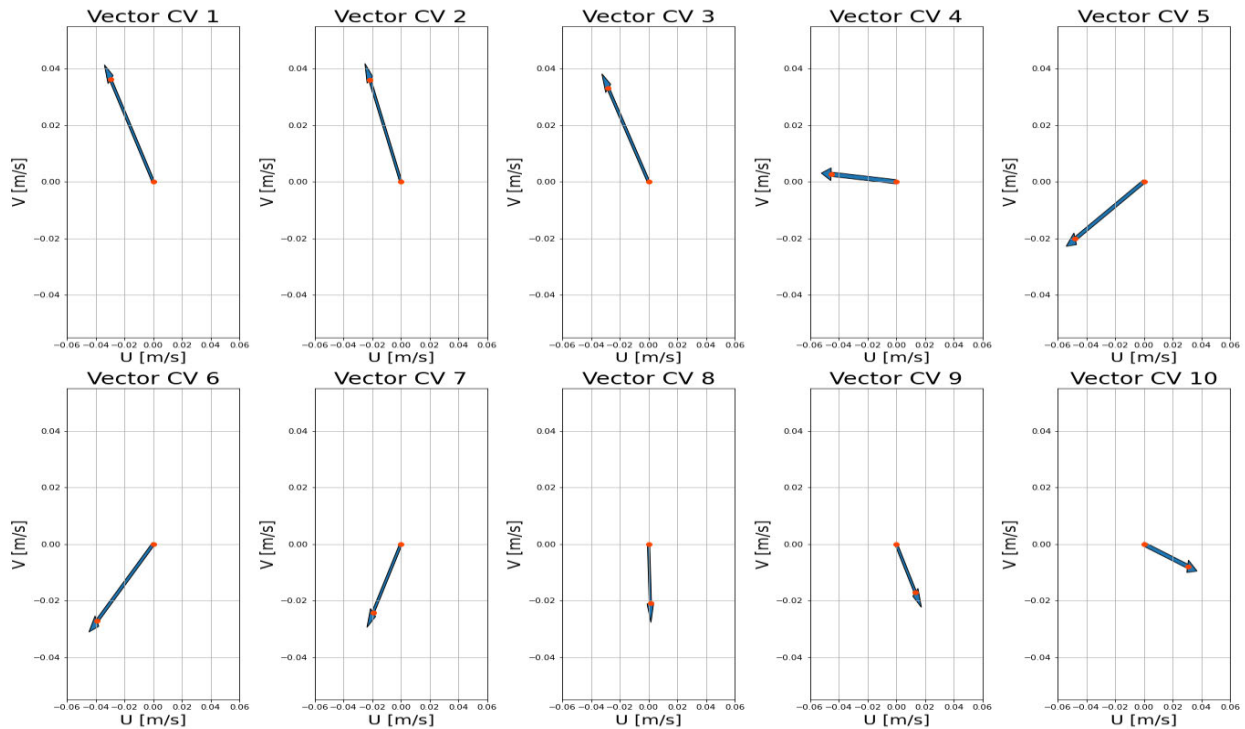


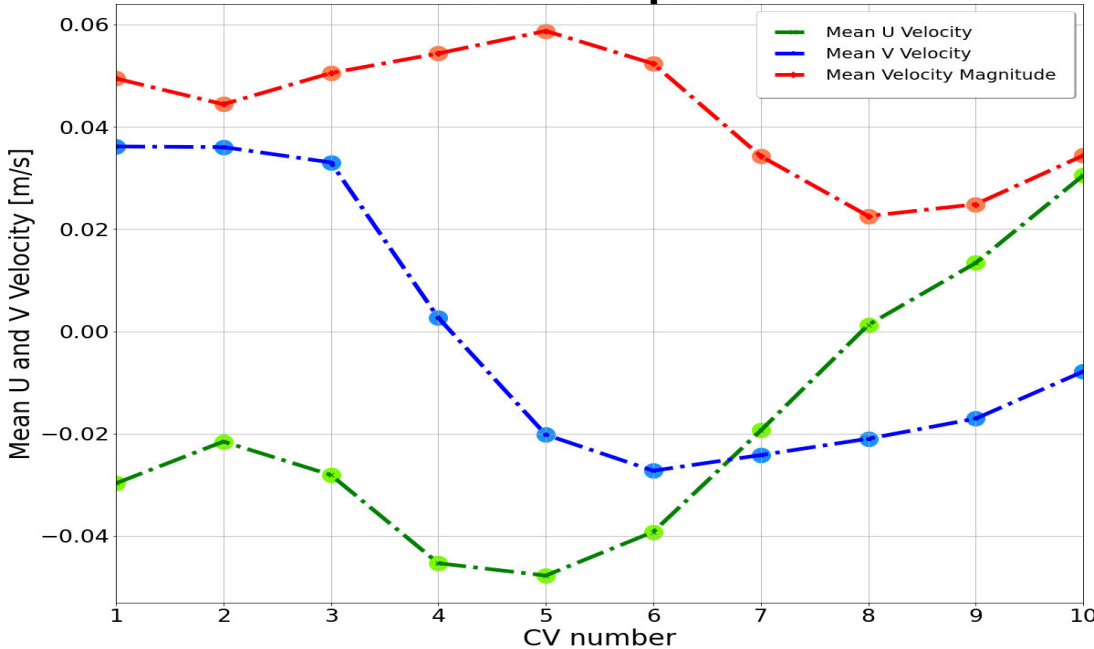
Figure 4-2: Mean flow vector per CV

In the X-plane the roller moves in the positive/right X-direction. Within the fluid: U_{Mean} initially moves positively between CVs 1-2, negatively between CVs 2-5 and positively again between CVs 5-10 (Figures 4-1 and 4-2). It is observed that within the regions which partially introduce the roller profile between CVs 1-2 (Figure 3-14) the fluid initially moves in the direction of the roller in the horizontal X-plane (Figure 4-1). Whereas between CVs 2-5 the fluid moves against the horizontal roller direction. This sudden jerk was observed as a drawback motion of the fluid. Between CVs 5-10 the roller begins its gradual exit from the FOV allowing for a restorative phase of the tube cross-sectional area (Figure 3-14). The tube, therefore, begins to expand on the left-hand side (LHS) of the roller-peak

profile. It is observed as the fluid is propelled horizontally forward under tube expansion, within CVs 5-10, the fluid changes trajectory and moves in the direction of the roller in the positive X-plane direction (Figure 4-2). Between CVs 2-10 the fluid maintains an anticlockwise overall trajectory (Figures 4-1 and 4-2).

In the Y-plane the roller acts in the upwards/positive direction causing a compressive force on the tube's lower boundary. V_{Mean} moves negatively between CVs 1-6 and positively between CVs 6-10 (Figure 4-1). Between CVs 1-3 the roller profile is gradually introduced into the FOV, where the peak profile point is first introduced in CV3. V_{Mean} is observed to marginally decrease between CVs 1-3 however between CVs 3-6 it undergoes a drastic decrease (Figure 4-1). The period between CVs 3-6 is observed as regions in which the roller profile is most prominent (causing peak compressive restriction in the Y-plane) (Figure 3-14). CVs 3-6 are identified as direct constrictions zones. Between CVs 6-10 the roller exits the FOV and the tube aims to restore its original shape. As the tubes cross-sectional area is restored to its original shape the tube expands and V_{Mean} steadily increases positively (Figure 4-1)

Mean Flow per CV



CVs:	U Gradient:	V Gradient:
1-2	+0.008	0.000
2-3	-0.007	-0.003
3-4	-0.017	-0.030
4-5	-0.002	-0.023
5-6	+0.009	-0.007
6-7	+0.020	+0.003
7-8	+0.021	+0.003
8-9	+0.012	+0.004
9-10	+0.017	+0.009

Figure 4-3: Mean velocity parameters of the flow over CVs 1-10

The peak positive V_{Mean} velocity occurs at CV 1 (Figure 4-3). Marginal decreases in V_{Mean} occur between CVs 1-3. Whereas a drastic decrease in V_{Mean} occurs between CVs 3-6. Within CVs 3-5 V_{Mean} rapidly decreases and changes sign from positive to negative (Figure 4-3). CV 6 holds the peak negative V_{Mean} . At CV6 V_{Mean} changes trajectory. Between CVs 6-10 V_{Mean} gradually increases as V_{Mean} tends to zero. In the Y-plane, the mean vertical fluid trajectory is observed to move negatively/downwards between CVs 1-6 and positively between CVs 6-10. The V_{Mean} fluid parameter is therefore observed to move negatively under tube compression (CVs 1-6) and positively under tube expansion (CVs 6-10) (Figure 31). CV 3 is identified as the region in which the roller-peak pressure point is introduced (full initial compression) and CV6 is the zone in which peak roller-profile pressure exits the FOV (initial period of full tube expansion: initially on the LHS of the roller-peak) (Figure 3-14). CV point 6 is identified as the region in which the fluids vertical trajectory changes sign convention (from negative to positive).

Initially between CVs 1-2 U_{Mean} holds a positive trajectory. Within CVs 2-5 however U_{Mean} gradually moves negatively, where CV 5 holds the peak negative U_{Mean} velocity. Between CVs 5-10 the horizontal fluid trajectory drastically increases positively (Figure 4-3). CVs 6-8 showed the sharpest/most drastic increase in U_{Mean} . Within CVs 7-8 U_{Mean} moves from negative to positive. CV 10 holds the peak positive U_{Mean} velocity. The fluid movement is therefore observed to initially move positively/right between CVs 1-2 (in the direction of the roller), negatively/left between CVs 2-5 (opposing the roller direction) and positively/right between CVs 5-10 in the X-plane (under tube expansion). CV point 2 and 5 are identified as zones in which the fluids changes its horizontal trajectory.

Table 4-1: Mean velocity relations in reference to Figure 4-3 (TP: Turning point)

CV:	U_{Mean}	V_{Mean}	$Vmag_{Mean}$	Notes:
1-2	Moves positively	Marginal negative movement Maximum (+) point	Decreasing	U_{Mean} initially moves in the + X-plane direction
2-3	Trajectory change Moves negatively	Marginal negative movement	Turning Point At CV2	U_{Mean} trajectory change coincides with $Vmag_{Mean}$ TP
3-4	Moves negatively (Drastic Decrease)	Moves negatively (Drastic decrease)	Increasing	Rapid decrease in V_{Mean} and U_{Mean}

4-5	Moves negatively	Moves negatively (Drastic decrease)	Increasing	Rapid decrease in V_{Mean}
5-6	Trajectory change Moves positively Maximum (-) point	Moves negatively	Turning Point at CV5 Maximum (+) point	U_{Mean} trajectory change coincides with $V_{mag_{Mean}}$ TP
6-7	Moves positively (Drastic Increase)	Moves positively Trajectory change Maximum (-) point	Decreasing	Drastic increase in U_{Mean} V_{Mean} trajectory change
7-8	Moves positively (Drastic increase)	Moves positively	Decreasing	Drastic increase in U_{Mean}
8-9	Moves positively $U_{Mean} \approx 0$	Moves positively	Turning Point At CV8 Maximum (-) point	U_{Mean} zero point coincides with $V_{mag_{Mean}}$ TP as $V_{mag_{Mean}}$ is dominated by V_{Mean}
9-10	Moves positively Maximum (+) point	Moves positively	Increasing	U_{Mean} increases under tube expansion

Turning points (TPs) along the mean velocity magnitude ($V_{mag_{Mean}}$) curve occur at CVs 2, 5 and 8 (Figure 4-3 and Table 4-1). The maximum $V_{mag_{Mean}}$ TP occurs at CV 5 whereas its minimum occurs at CV 8. Critical TPs at CV2 and 5 coincided with trajectory changes in the U_{Mean} component; whereas for the TP at CV8 the $U_{Mean} \approx 0$ and the magnitude of $V_{mag_{Mean}}$ is largely held by V_{Mean} (Figure 4-3 and Table 4-1). After which the bulk of the $V_{mag_{Mean}}$ is held by U_{Mean} as V_{Mean} gradually becomes less negative and tends towards zero as the tube is under no compressive influence. By CVs 9-10 the bulk of the $V_{mag_{Mean}}$ is held by the U_{Mean} velocity component; this is observed by the close relation between the U_{Mean} and the $V_{mag_{Mean}}$ parameters (Figure 4-3).

Changes in the internal fluid structure are a result of the gradually constricting influence of the roller profile against the tubes lower boundary. Isolated velocity components U and V are observed per CV in Figure 4-4 providing a more detailed description of the fluid motion and velocity changes over the length of the FOV per CV. Figure 4-4 is non-dimensionalised where both U_{Mean} and V_{Mean} velocity components are placed over the average roller speed in the Y-plane and X is placed over D (the tube diameter) in the X-plane. The relationship between the roller peak position and the variations in velocity profiles are observed per CV (Figure 4-4). The $Roller_{peak\ position}$ represents the greatest

constriction point due to the roller-profile against the tubes lower boundary in accordance with Figure 3-14.

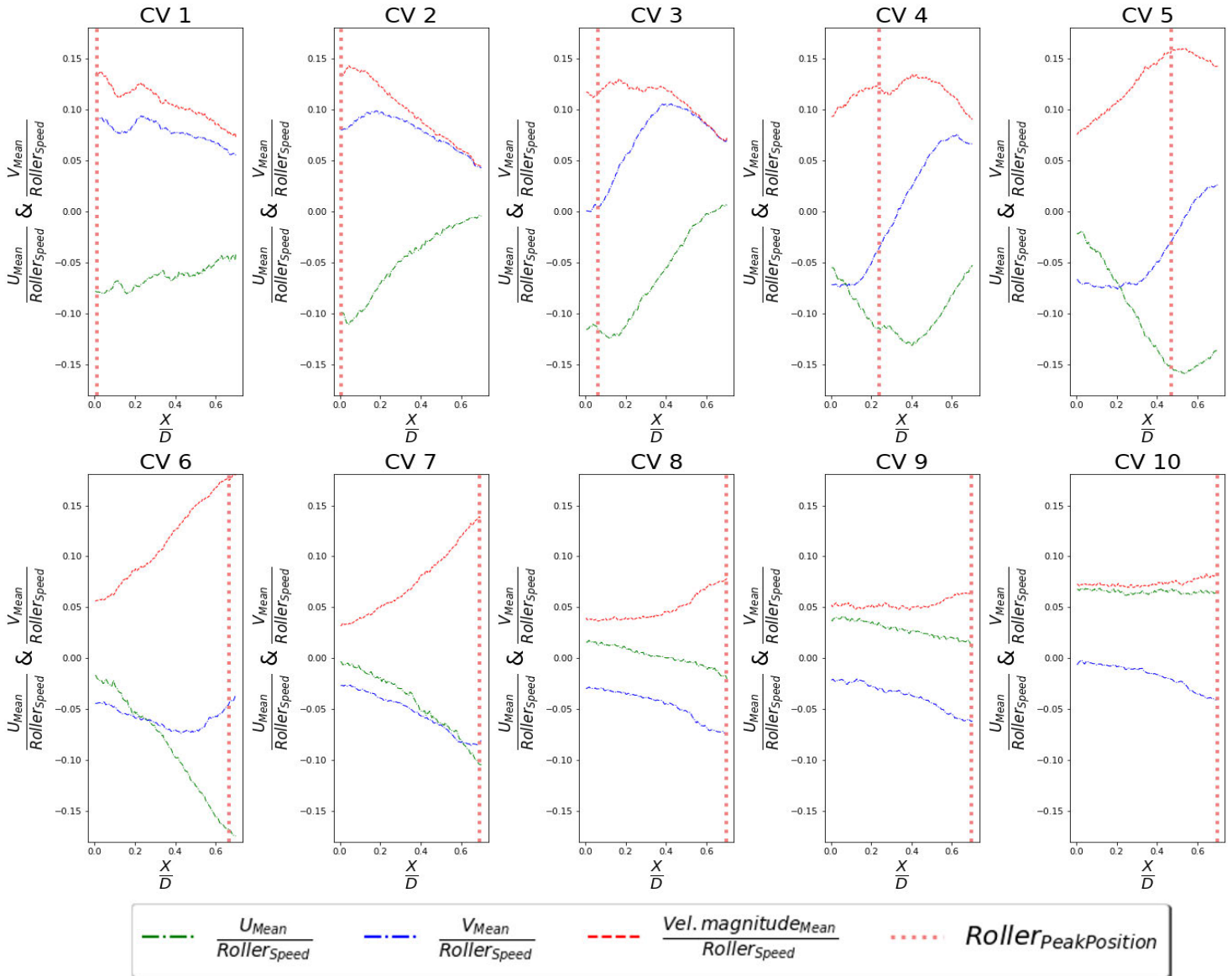


Figure 4-4: Non-dimensionalised velocity profiles in relation to the roller-peak position

Between CVs 1-10 the peak negative U_{Mean} is observed to move in close proximity with the $Roller_{peak position}$ (Figure 4-4). Across the constriction zones (CVs 1-6) the peak negative U_{Mean} becomes increasingly more negative, in close proximity with the $Roller_{peak position}$; whereas under tube expansion (CVs 6-10) U_{Mean} increases as the roller exits and U_{Mean} is distributed more uniformly across the FOV between CVs 8-10 (Figure 4-4). The U_{Mean} velocity profile per CV is therefore observed to distort

negatively under the influence of the roll-peak and U_{Mean} increases drastically due to tube expansion in the form of a bulge wave.

Across the direct tube constriction zones (CVs 1-6): V_{Mean} was observed to hold a positive/increasing trend relative to the RHS of the $Roller_{peak\ position}$ and hold a negative/decreasing trend relative to the LHS of the $Roller_{peak\ position}$ (Figure 4-4). However, under tube expansion (CVs 6-10) both U_{Mean} and V_{Mean} increased correspondingly. Between CVs 1-6: V_{Mean} was transformed to overcome the constricting influence of the roller profile on the tube's lower boundary. This generated an 'overturning' motion on the RHS of the $Roller_{peak\ position}$ and a 'spilling' motion on the LHS of the $Roller_{peak\ position}$.

Variations in the external pressure have a direct effect on the degree of growth (more circular shape) or reduction (more elliptical shape) of the tubes cross-sectional area (Grotberg and Jensen 2004). The FPB enclosure was filled to a zero-pressure gradient relative to the flumes surrounding medium. The tube therefore consistently aims to conserve its original circular cross-sectional shape. Under an external pressure the internal fluid structure is therefore transformed based on the degree of compression, and transformed again as the tube aims to counteract the compressive influence by expanding to restore its original shape; this was observed by the 'spilling' and 'overturning' motion.

The interactive relationship between the tube-profile and fluid motion are detailed on a streamline plot (Figure 4-5). Streamlines show the instantaneous direction of fluid motion throughout the flow field. Within unsteady flows streamline patterns change over time (Kundu 2003). Within an instantaneous time period a velocity vector exists along each grid-point/interrogation area. A streamlines path lies tangential to the average direction of the velocity field. The fluid streamline plot provides detailed representation of the isolated fluid movement pattern over and around the roller mechanism per CV (Figure 4-5). The fluid moves upward and left when on the right hand side (RHS) of the roller-peak (Figure 4-6A) whereas the fluid moves downward and left on the left hand side (LHS) of the peak (Figure 4-6B).

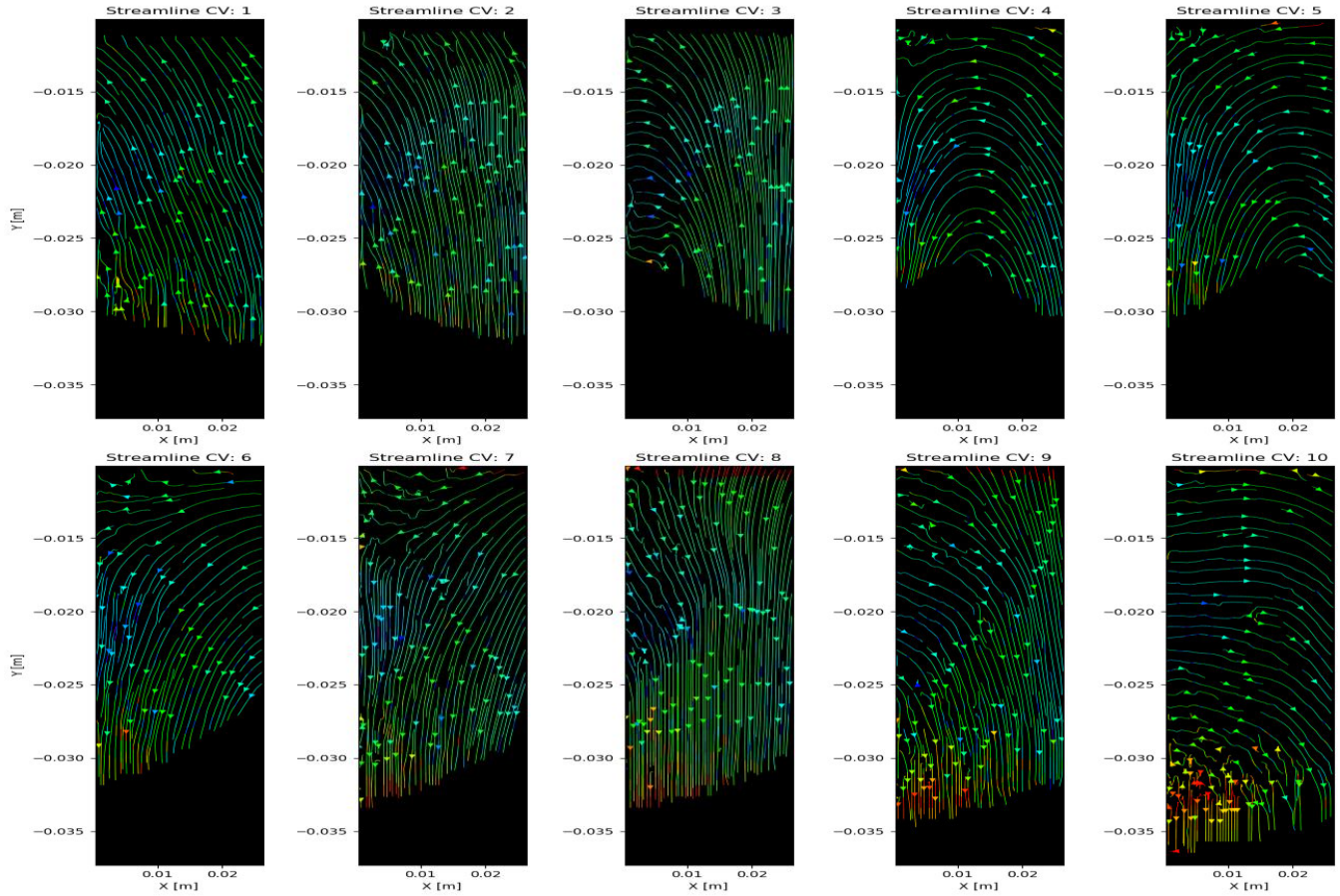


Figure 4-5: Instantaneous streamline plot per CV

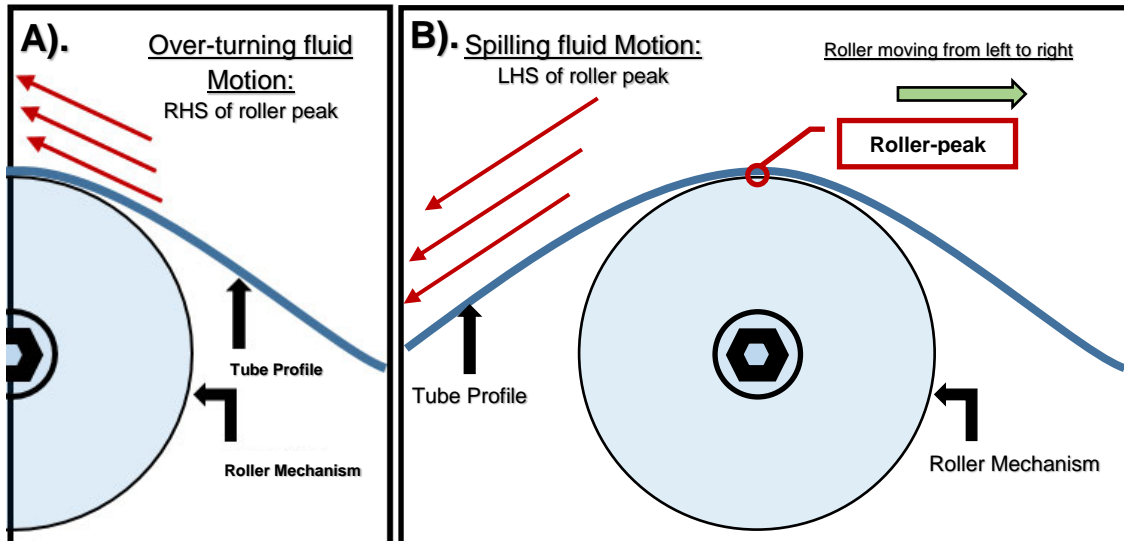


Figure 4-6: Fluid motion under the influence of the rollers pressure profile. The roller moves from left to right. The fluid is displaced along the curved profile

A semi-circular roller profile is placed on the tubes lower boundary across CVs 1-10. The roller moves from left to right in the X-plane. Pressure varies along the curved roller-profile and the fluid is therefore displaced non-uniformly. Between CVs 1-3 the fluid motion is observed relative to the RHS of the roller-peak; where the fluid is transformed positively in the Y-plane and negatively in the X-plane (Figure 4-5 and 4-6A) as it undergoes an over-turning motion to counteract the presence of the roller profile. However, in regions where the roller-peaks position lies centrally within the FOV (CVs 3-5): fluid motion is observed relative to both the LHS and RHS of the peak position. On the LHS of the peak the fluid moves negatively in the Y-plane and negatively in the X-plane (Figure 4-5 and 4-6B) and the fluid experiences a spilling motion. CVs 3-5 are subject to both the “spilling and overturning” action of the fluid over the roller-profile. Between CVs 6-7 the fluid is observed relative to the LHS of the roller-peak only; here the fluid maintained the spilling motion and moved negatively in both the X and Y planes (Figure 4-6B). It is observed that when the fluid is viewed on the RHS of the roller-peak the fluid aims to overcome/overturn the constriction whereas on the LHS of the roller-peak the fluid is given the freedom to disperse and spill over the roller-peak (Figure 4-4, 4-5 and 4-6). This relationship holds true between CVs 1-7. However, between CVs 8-10, under tube expansion, the fluid is free of the rollers compressive influence; as the tube is given the freedom to expand the fluid is propelled forward in the form of a bulge wave. Regions of drastic loss in V_{Mean} are observed between CVs 3-5 (Figure 4-3 and Table 4-1); these can be attributed to the large fluid spilling action on the LHS of the roller peak. Whereas regions of rapid increases in U_{Mean} are attributed to tube expansion.

Fluctuations in momentum cause the deformation of a fluid parcel. Reynolds stresses arise due to the turbulent transport of momentum. Further away from the wall boundary Reynolds stresses are produced in the form of a spiraling fluid motion (vortices) where fluid particles accelerate or decelerate while changing direction (Bernard and Handler 1990). Total Reynolds stress represents the net transport of momentum arising from the unpredictability of the fluid particle motion in the presence of a mean shear. The Reynolds stresses are therefore an indication towards the zones in which turbulence/mixing occurs; due to fluctuations in momentum caused by the unsteady/turbulent flow conditions.

Reynolds stresses are a function of mean quantities and indicate the relationship between the mean flow and background flow. Reynolds Stresses are calculated per CV where Reynolds Stress= $(U - \bar{U}) (V - \bar{V})$ to represent the stresses experienced across the FOV. (Figure 4-7)

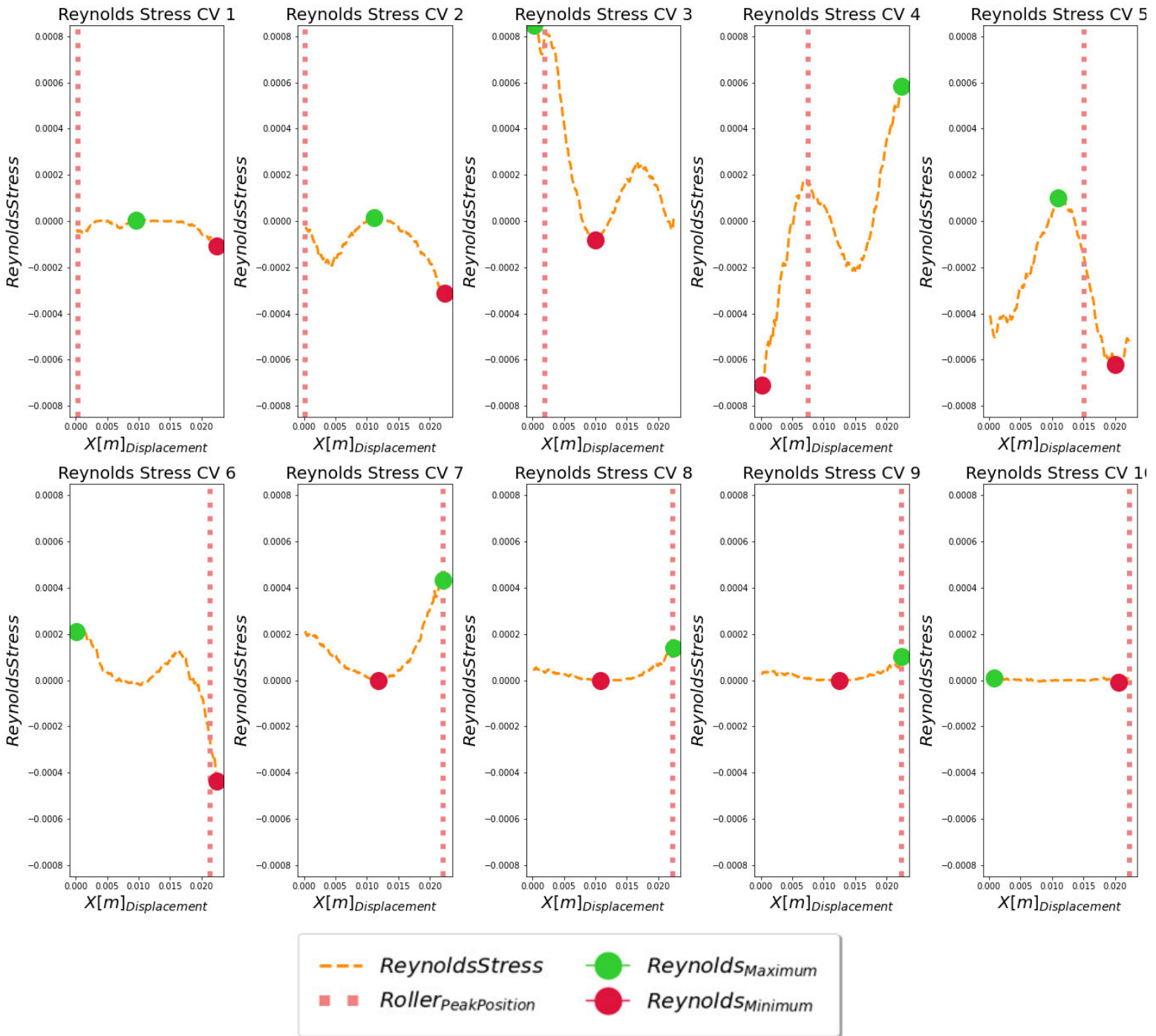


Figure 4-7: Reynolds stresses per CV in relation to the roller-peak profile

Table 4-2: Location of minimum and maximum Reynolds stresses across the FOV for CVs 1-10 in reference to Figure 4-7

CV No:	X_{Min} :	$Reynolds_{Min} \times 10^5$	X_{Max} :	$Reynolds_{Max} \times 10^5$
1	0.0224	-10.976	0.0095	+0.518
2	0.0223	-31.357	0.0111	+1.484
3	0.0100	-8.237	0.0002	+84.817
4	0.0002	-71.088	0.0224	+58.489
5	0.0200	-62.253	0.0110	+9.932
6	0.0224	-43.759	0.0001	+21.085
7	0.0118	-0.027	0.0221	+43.316
8	0.0109	-0.114	0.0224	+14.099
9	0.0124	-0.233	0.0224	+10.209
10	0.0206	-0.805	0.0009	+1.071

At CV1 the $Reynolds_{Max}$ remains relatively unchanged (Figure 4-7 and Table 4-2). At CV2, due to the initial roller-tube constriction (Figure 4-5 and 4-6A), the fluid is forced upwards relative to the RHS of the roller-peak. As the fluid undergoes the initial overturning motion the $Reynolds_{Min}$ is observed to peak on the RHS of the FOV (Figure 4-7). At CV3 the fluid begins to spill on the LHS of the roller-peak (Figure 4-5 and 4-6B). The $Reynolds_{Max}$ coincides with the overturning fluid motion at CV3. At CV4 the fluid is subject to both the spilling at overturning motion on both the LHS and RHS of the roller-peak position. The $Reynolds_{Min}$ is found to peak in regions of direct spilling whereas the $Reynolds_{Max}$ peaks in regions in which the fluid undergoes the overturning motion (Figure 4-7). At CVs 5-6 the fluid undergoes the direct spilling motion (Figure 4-4) and therefore peaks negatively. Between CVs 6-10 the fluid changes trajectory under tube expansion; the instability of the flow is gradually minimized as the fluid is propelled forward in the form of a bulge wave and the Reynolds stress curve becomes linear. The standard deviations indicate the level in which the velocity varied around the mean average velocity over the FOV per CV (Figure 4-8).

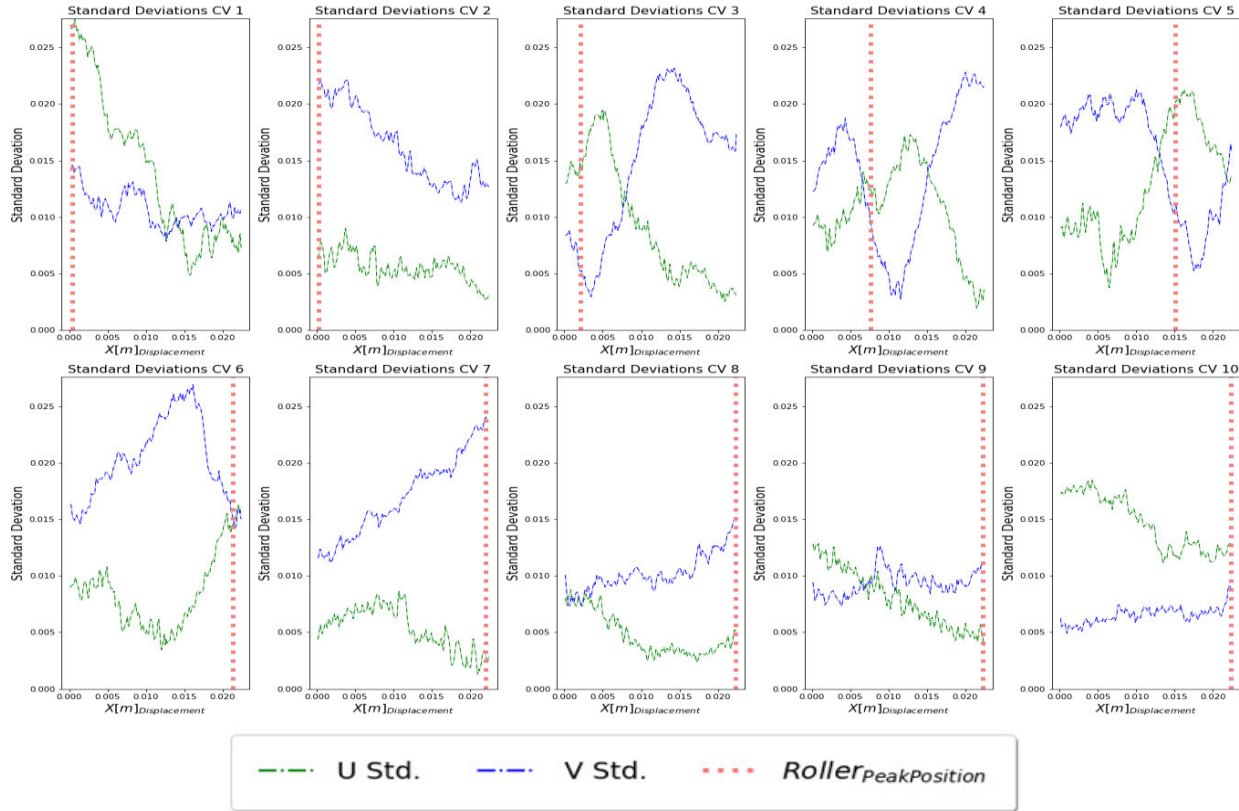


Figure 4-8: Standard deviations per CV in relation to the roller-peak profile across the FOV

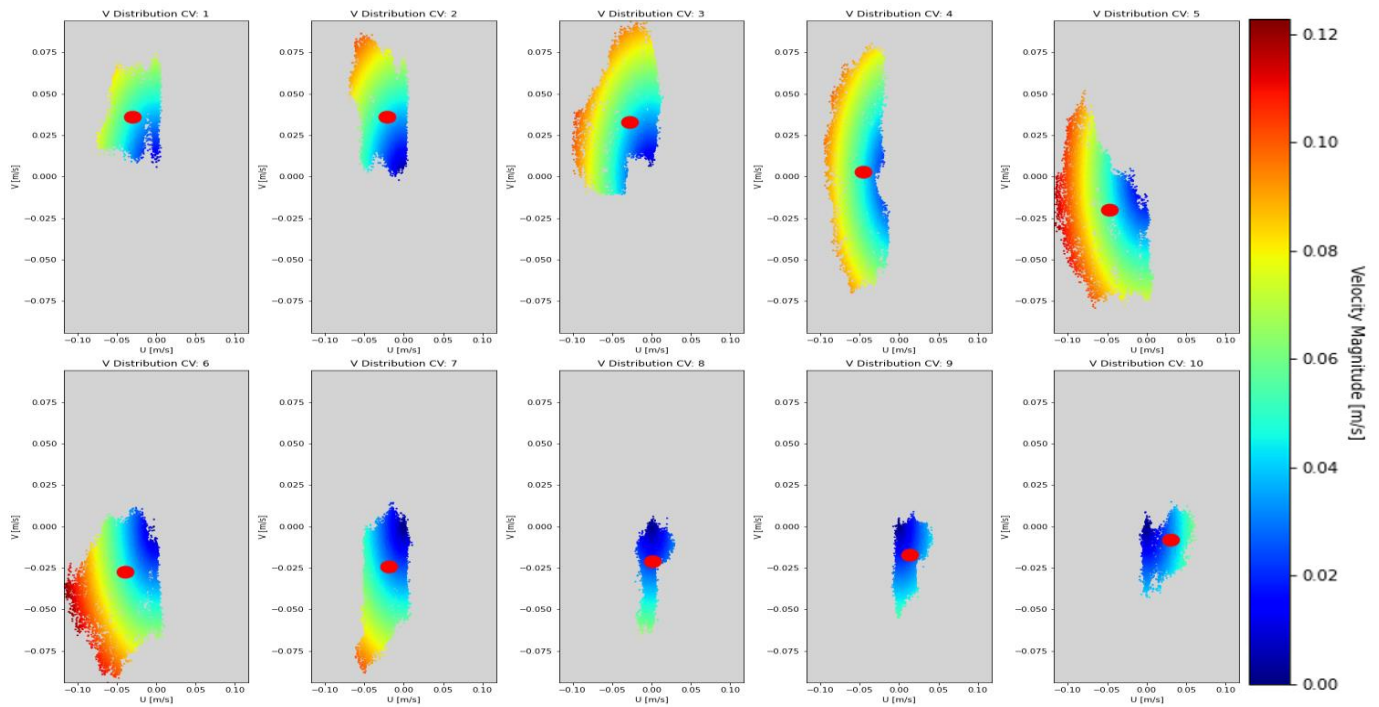


Figure 4-9: Velocity distribution around the mean (red marker) per CV

Standard deviations $U_{std.}$ and $V_{std.}$ vary along the FOV. Peak positive and negative values along the standard deviation curves coincide with peak U_{Mean} and V_{Mean} velocity parameters within each FOV per CV (Figure 4-4). Spikes in the standard deviation indicate regional spikes/changes in the mean velocity, therefore, indicating regions subject to rapid changes in the flow. Figure 4-9 represents the velocity distribution of data over the full investigation per CV. The data becomes more dispersed around the mean velocity parameter (red marker) between CVs 3-6 (direct compression zones). As the tube expands the velocity distribution becomes more centralized as V approaches zero and the fluid is propelled forward in the form of a bulge wave.

The combination of the rollers transverse and compressive influence on the tube generates a transfer in energy between the roller mechanism and the internal fluid structure. A V_{mag} contour plot aims to depict the differing regions of velocity magnitude.

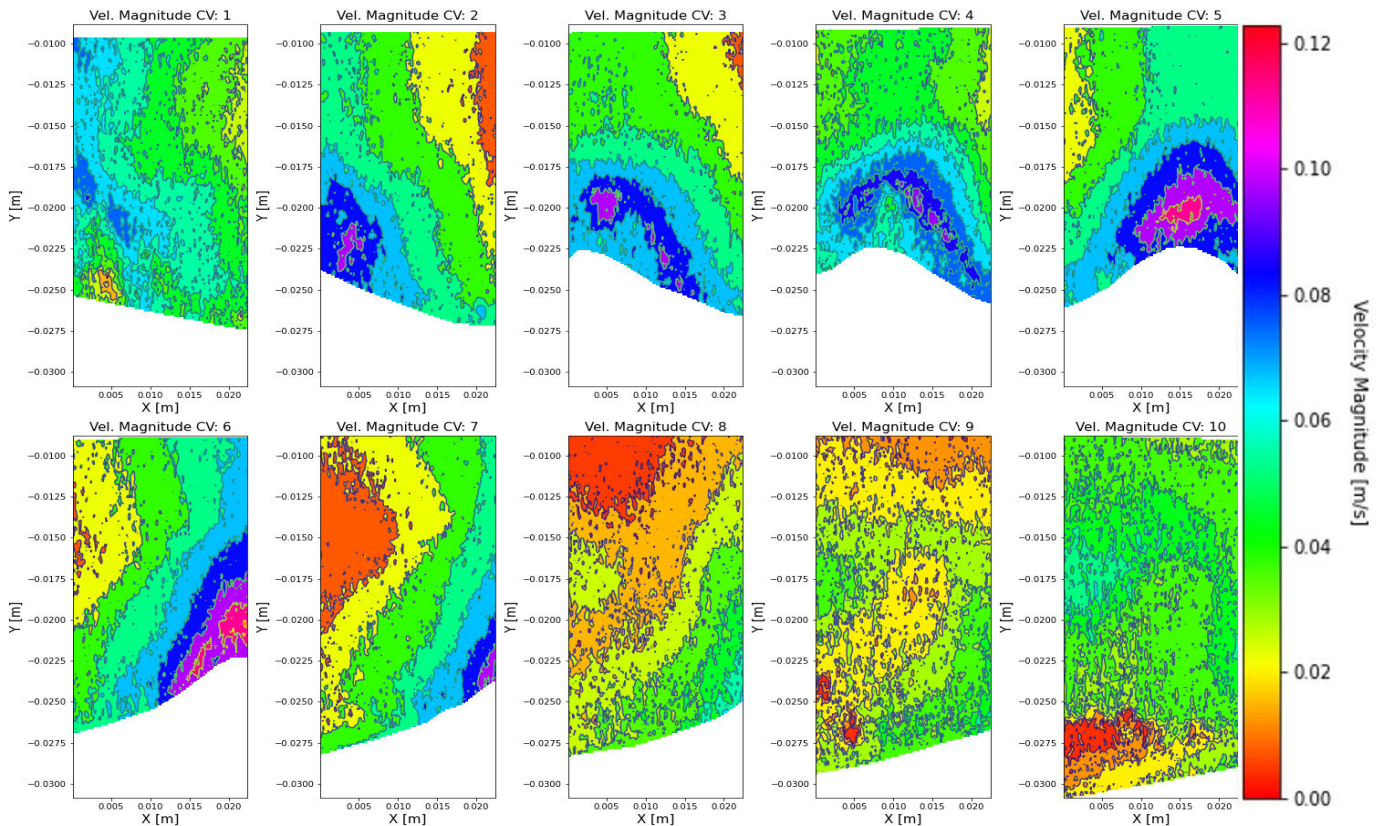


Figure 4-10: Detailed velocity magnitudes across each CV under direct contact with the tube profile.

The magnitude of the flow is notably stronger against the tube's roller-contact boundary (Figure 4-10). Stratified regions of the magnitude are observed to physically shape to the rollers profile. Between CVs 8-10 (under unrestricted tube expansion) the regions become more sporadic as the fluid is propelled forward. The mean velocity profiles (Figure 4-11) indicate how the flow varies along the Y-plane. V is observed to decrease towards the upper region of the tube. At CV4 the bulk of the V profile lies at zero this is due to the lateral motion of the fluid between the overturning and spilling motion (Figure 4-5).

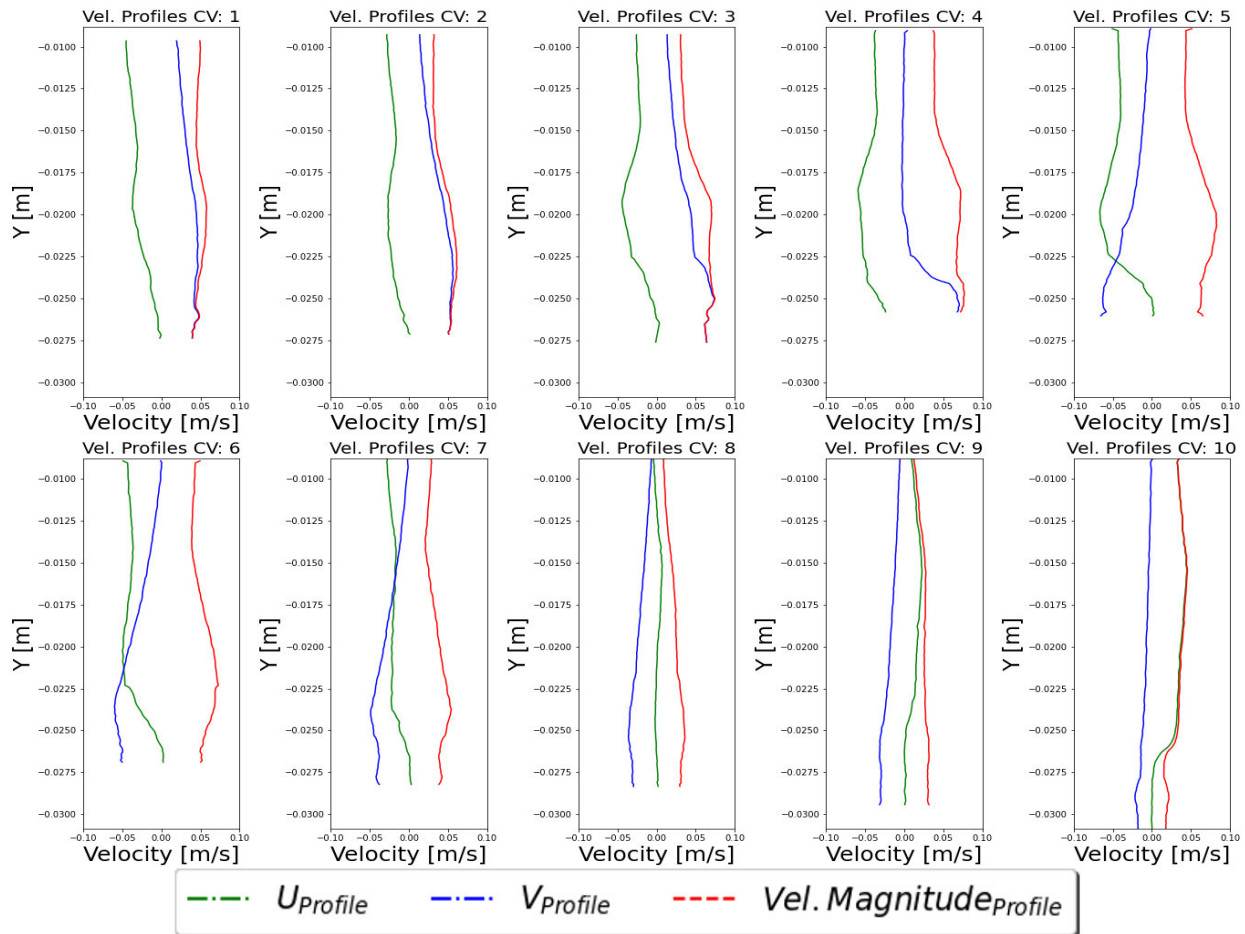


Figure 4-11: Mean velocity profiles per CV

Figure 4-11 displays the mean velocity profiles per CV, however, the magnitude of the flow varies under the influence of the roller. Figures 4-13 to 4-22 provide isolated velocity cross-sections across each CV; indicating variations in U , V and V_{mag} per CV. Four cross-sections are taken equidistant across the FOV. Each cross-section aims to depict how the velocity varies along the FOV under direct influence of the roller-mechanism per CV

(Figure 4-12). Within Figures 4-13 to 4-22 the velocity magnitude was observed to peak in close proximity with the roller-peak position.

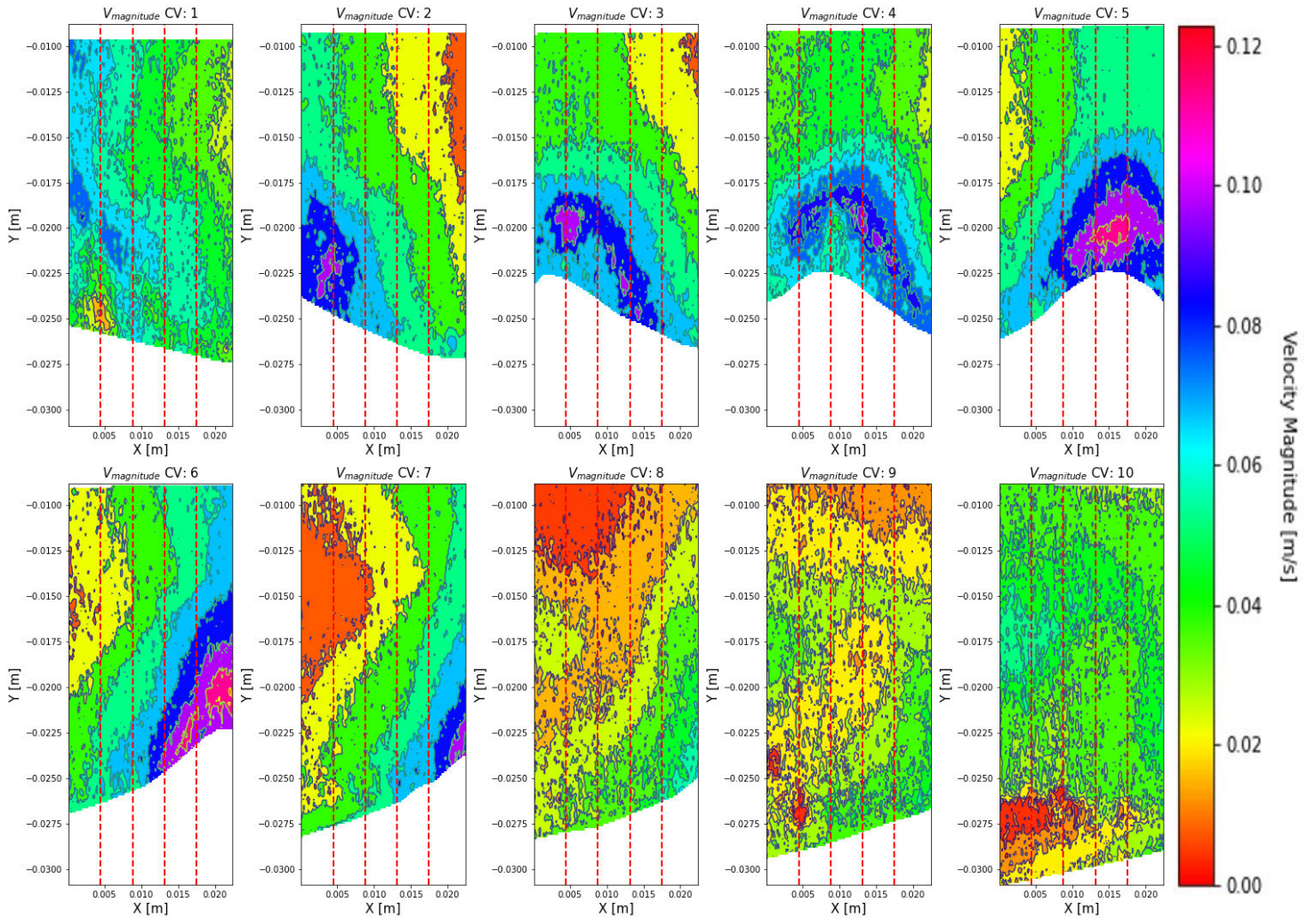


Figure 4-12: Cross-sections taken across the FOV per CV

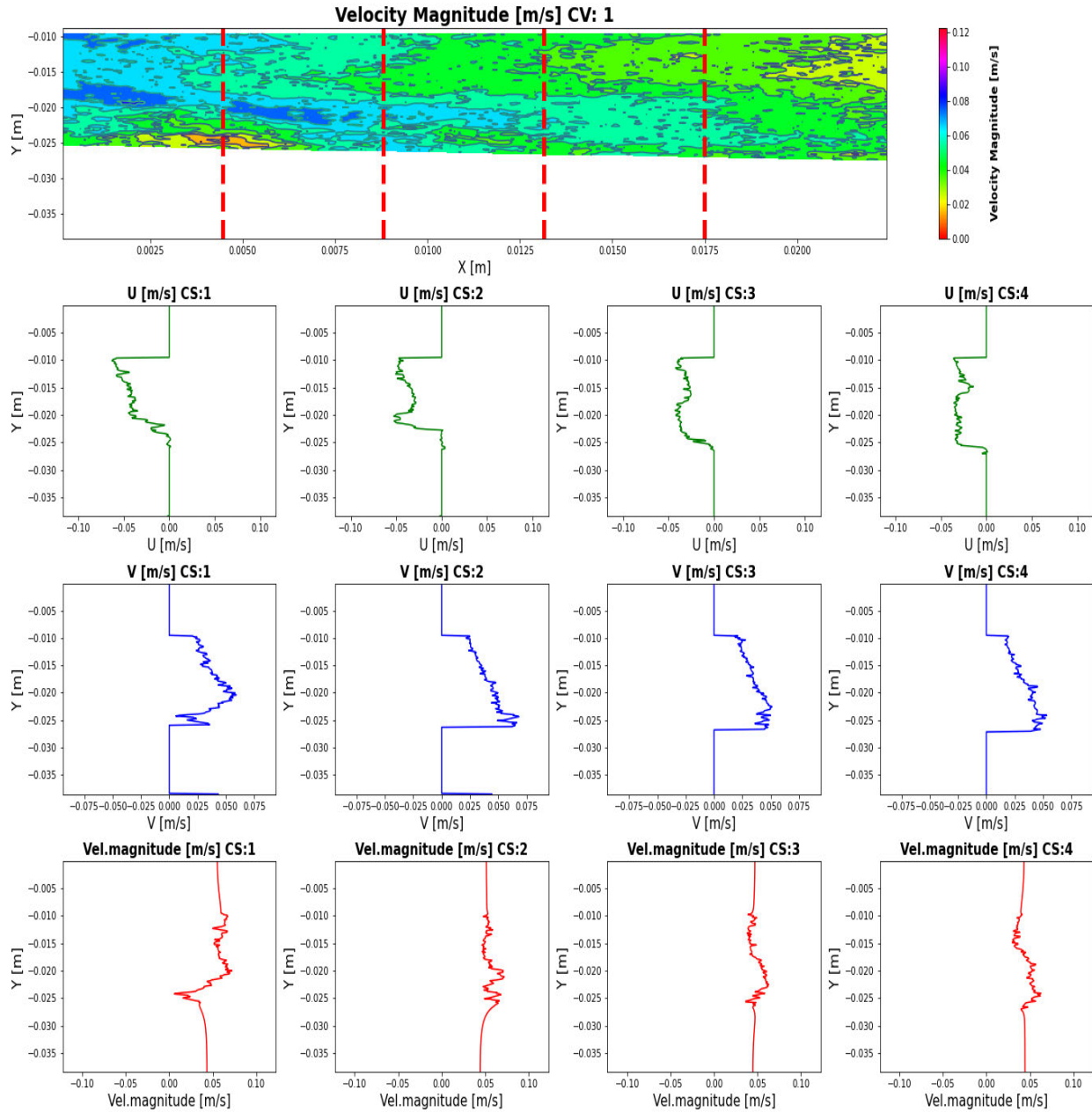


Figure 4-13: CV1: Velocity profiles at cross-sections

In Figure 4-13: CV1, U is negative and decreases along all cross-sections (CSs). Lower regions of the $U_{Profile}$ are observed to approach zero. The V_{mag} in the lower roller-tube contact region is therefore observed to be largely influenced by the magnitude of the $V_{Profile}$. V_{mag} is observed to marginally increase in the lower roller-tube contact region. V is observed to decrease towards the upper boundary layer. At CS1, there is a pocket region in which $V_{mag} \approx 0$. $V_{Profile}$ held a sharp change in velocity between CS 1 and 2.

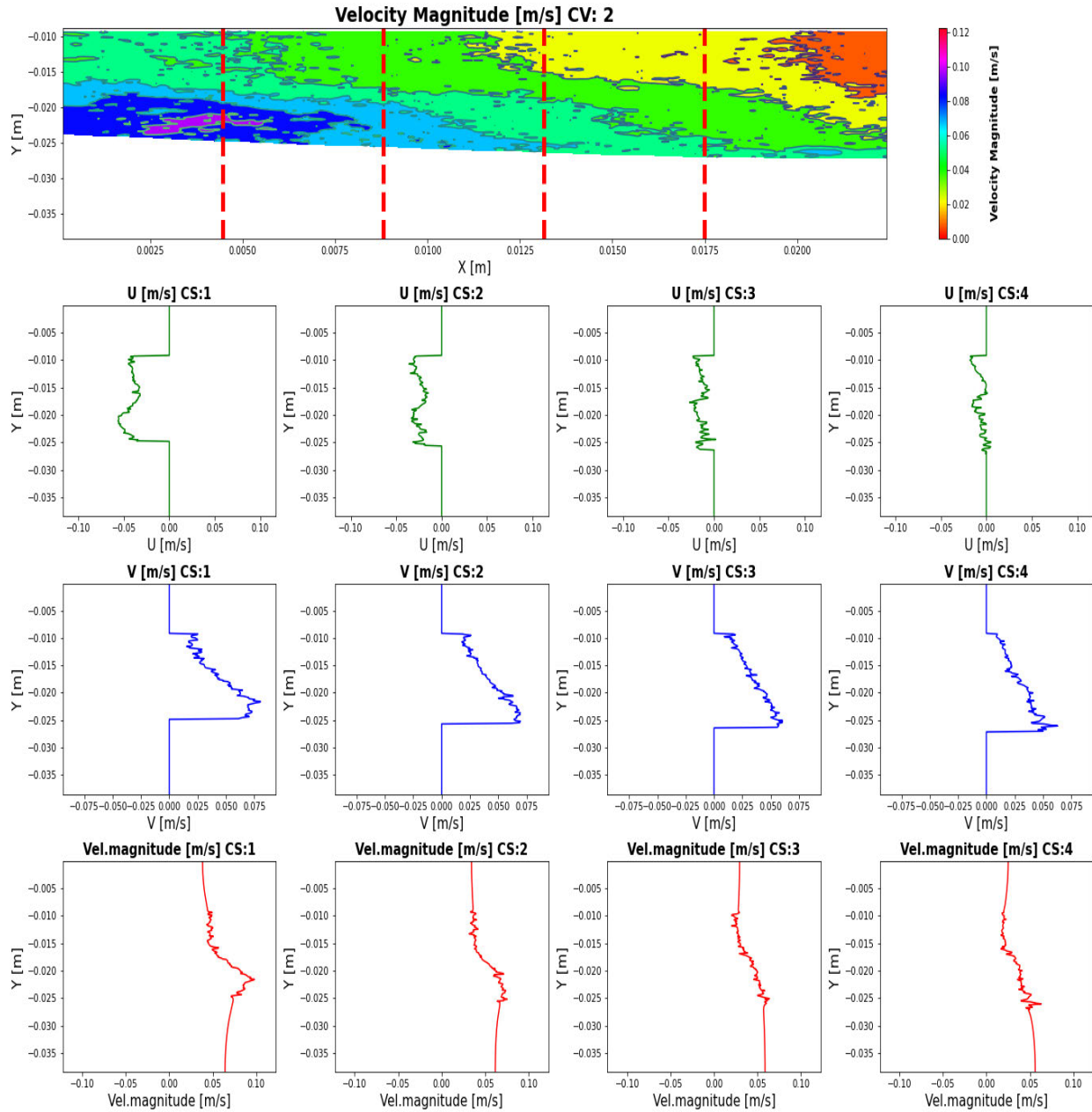


Figure 4-14: CV2: Velocity profiles at cross-sections

In Figure 4-14: CV2, U moves negatively and decreases along the CSs within the FOV. V continues to increase in the lower regions of the roller-tube contact region. The V_{mag} is observed to be largely influenced by the magnitude of the $V_{Profile}$. V_{mag} continues to increase in the lower roller-tube contact region. V continues to decrease towards the upper boundary layer. Just beyond CS4, there is a pocket region in which $V_{mag} \approx 0$.

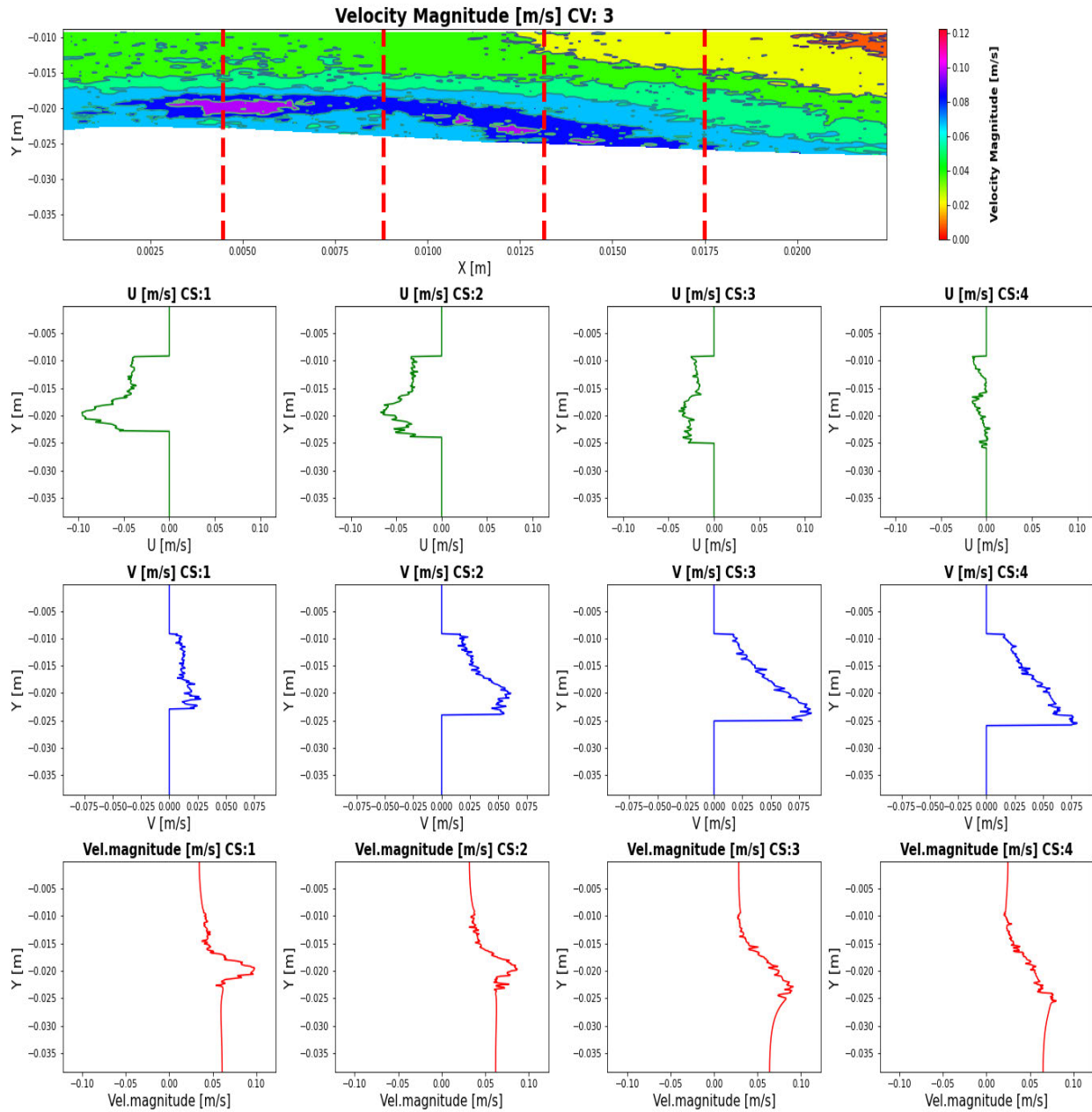


Figure 4-15: CV3: Velocity profiles at cross-sections

In Figure 4-15: CV3, the roller-peak profile is introduced. This was identified as the initial constriction zone. U is observed to move more negatively in proximity to the roller-peak and decrease along the CSs within the FOV. V was observed to decrease in proximity to the roller profile but increase further along the CSs due to the forced overturning motion of the fluid. V_{mag} peaked at CS1 due to the rapid increase of U . Just beyond CS4, the pocket region in which $V_{mag} \approx 0$ begins to exit the FOV.

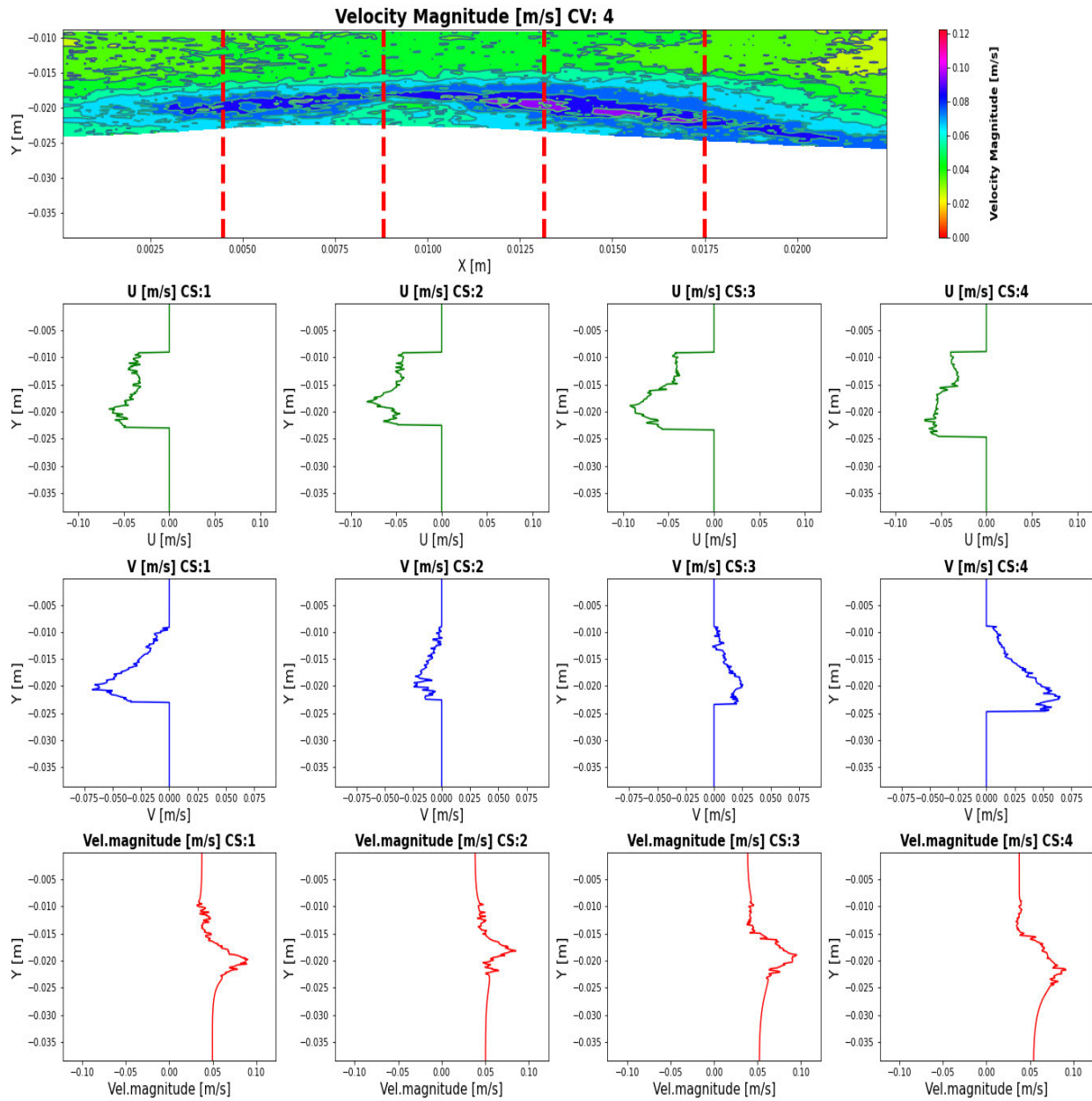


Figure 4-16: CV4: Velocity profiles at cross-sections

In Figure 4-16: CV4, the fluid is subject to both the spilling and overturning fluid motion. In proximity with the roller-peak position V was observed to decrease. On the LHS of the roller-peak position V moves negatively whereas on the RHS V moved positively. In both cases V decreased toward the upper tube boundary. U continued to move more negatively in close proximity with the roller-peak position.

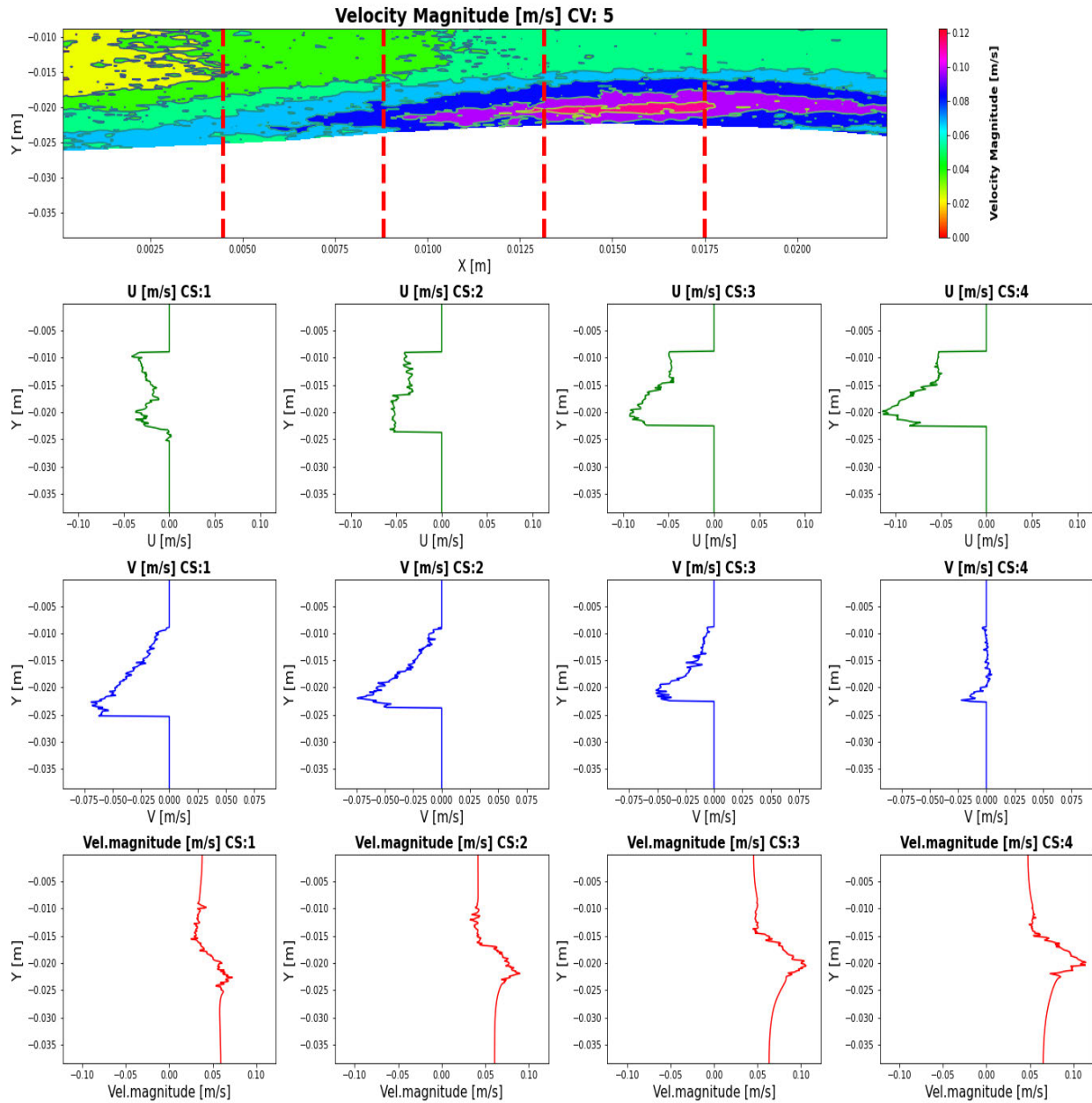


Figure 4-17: CV5: Velocity profiles at cross-sections

In Figure 4-17: CV5, the fluid remains subject to the spilling and overturning fluid motion. In proximity with the roller-peak position V continued to decrease. On the LHS of the roller-peak position V moves negatively. In both cases V continued to decrease toward the upper tube boundary. U was observed to become less negative further away from the roller-peak position however continued to become more negative in close proximity with the roller-peak position. A pocket region of high V_{mag} is observed between CSs 3-4.

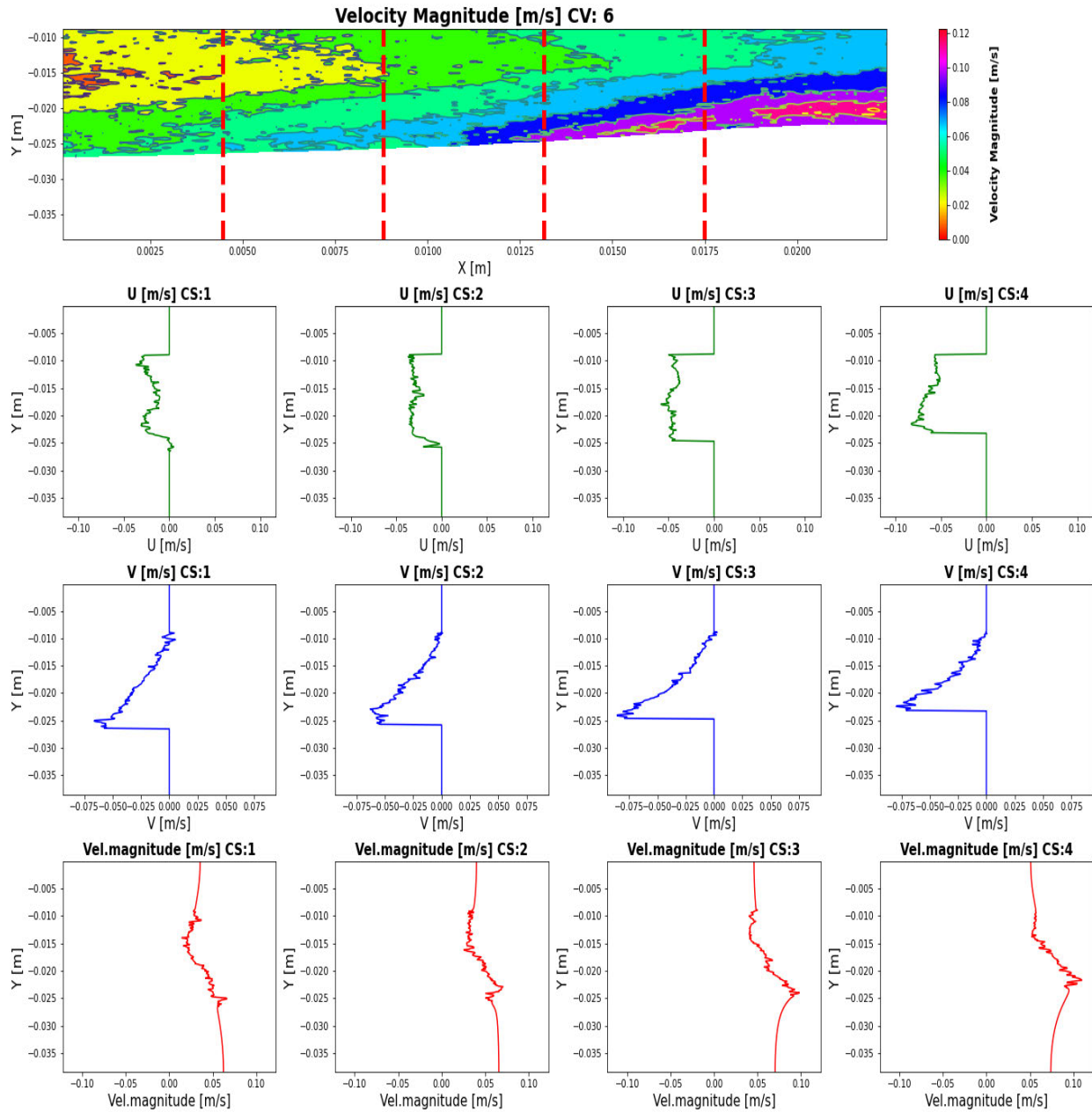


Figure 4-18: CV6: Velocity profiles at cross-sections

In Figure 4-18: CV6, the fluid is no longer subject to the overturning fluid motion. Under fluid ‘spilling’, V continues to move negatively. U became less negative further away from the roller-peak position (continued to change trajectory) and continued to move negatively in close proximity with the roller-peak position. A pocket region of high V_{mag} is observed on the RHS of CS4.

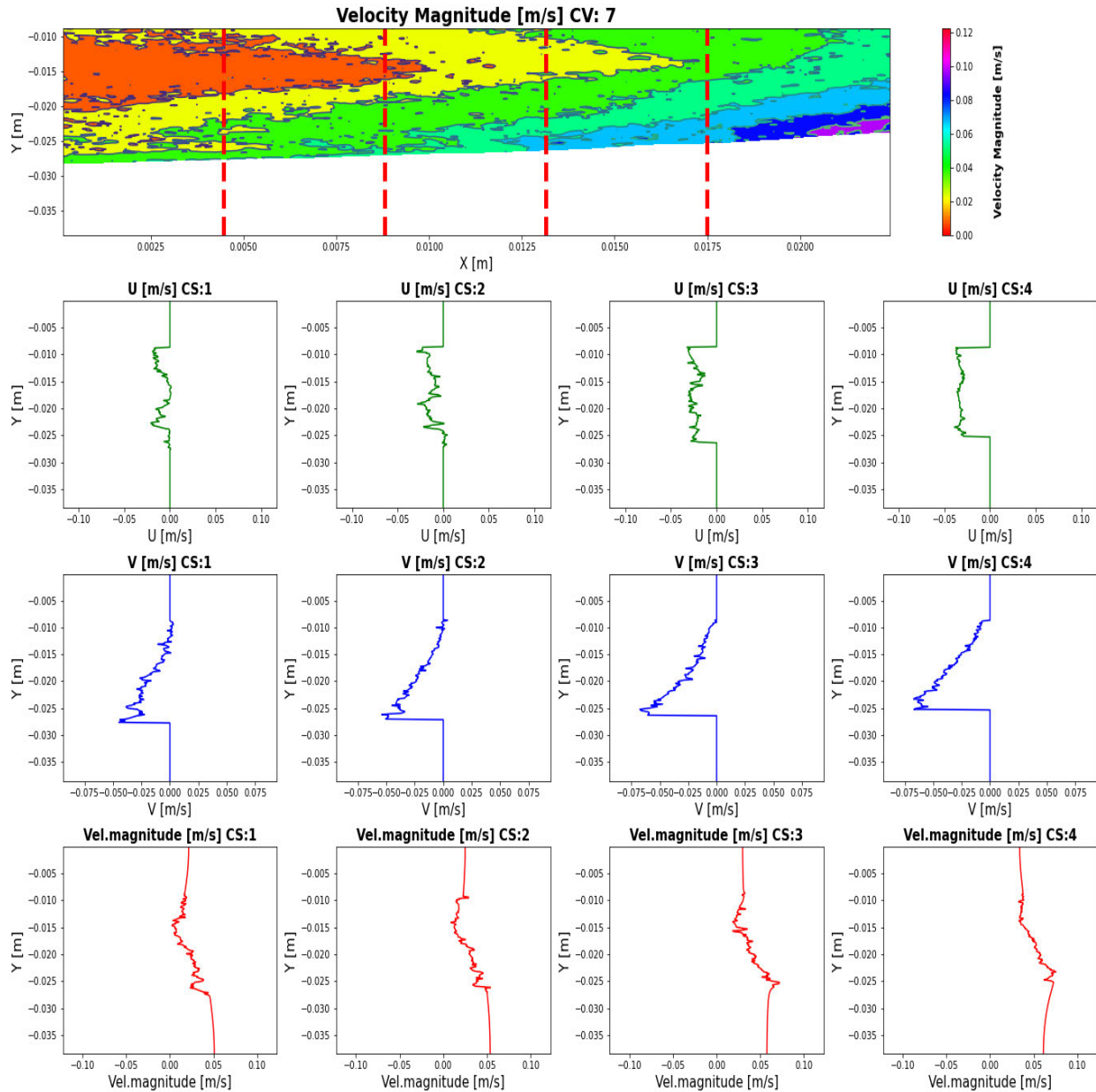


Figure 4-19: CV7: Velocity profiles at cross-sections

In Figure 4-19: CV7, the fluid undergoes a transitional period in which the tube begins to expand. Under tube expansion U and V becomes less negative. V_{mag} therefore decreases. On the LHS of the FOV the flow is largely governed by V as V decreases toward the tube's upper boundary however the $V_{mag} \approx 0$.

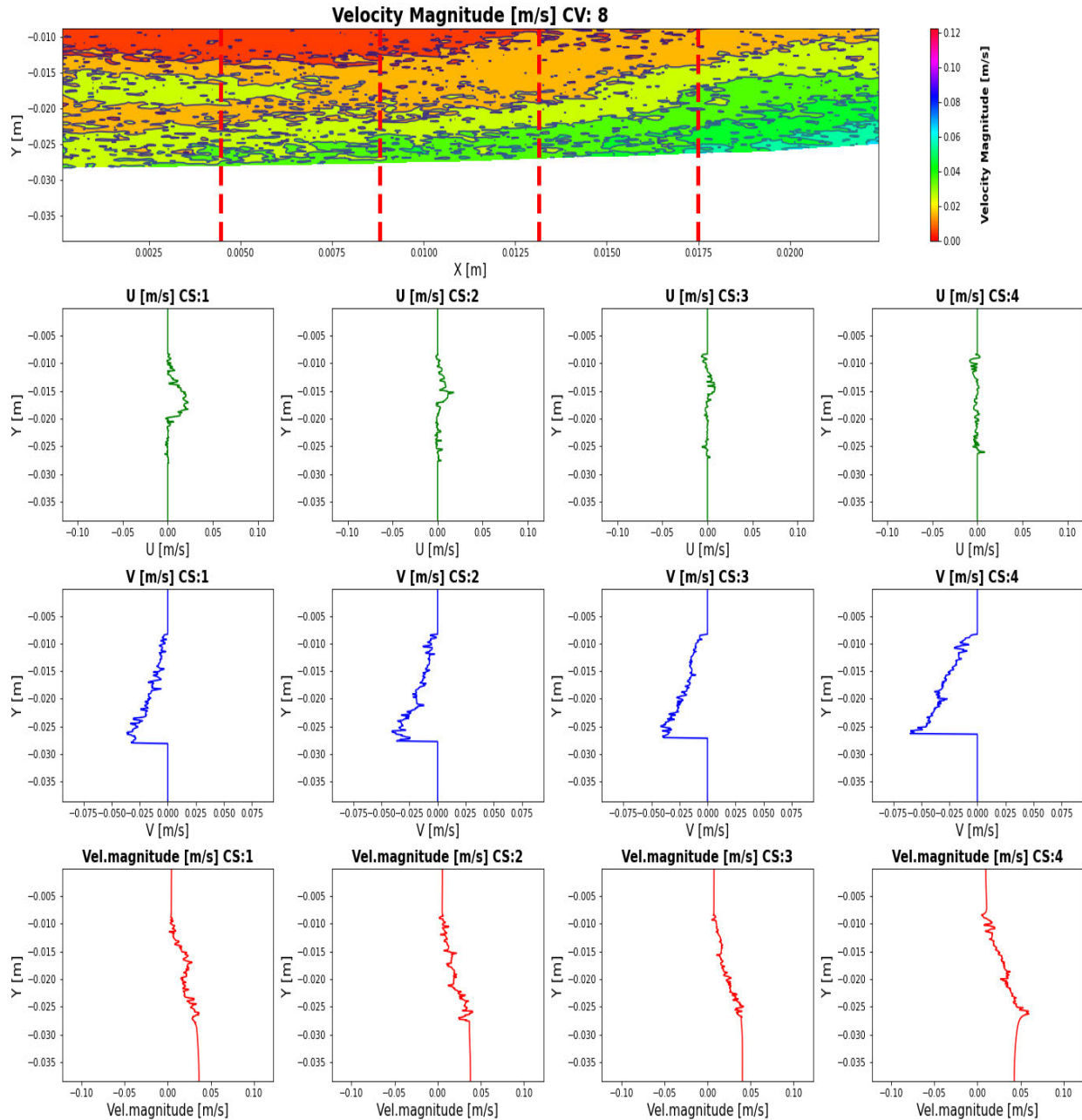


Figure 4-20: CV8: Velocity profiles at cross-sections

In Figure 4-20: CV8, the fluid continues its transitional period under tube expansion where U and V continue to become less negative; and V_{mag} continues to decrease. As U approaches zero the flow is largely governed by V ; however, V too continues to decrease and maintains the pattern of decreasing toward the tube's upper boundary. The bulk of the flow is governed by V particularly in the lower roller-tube contact region.

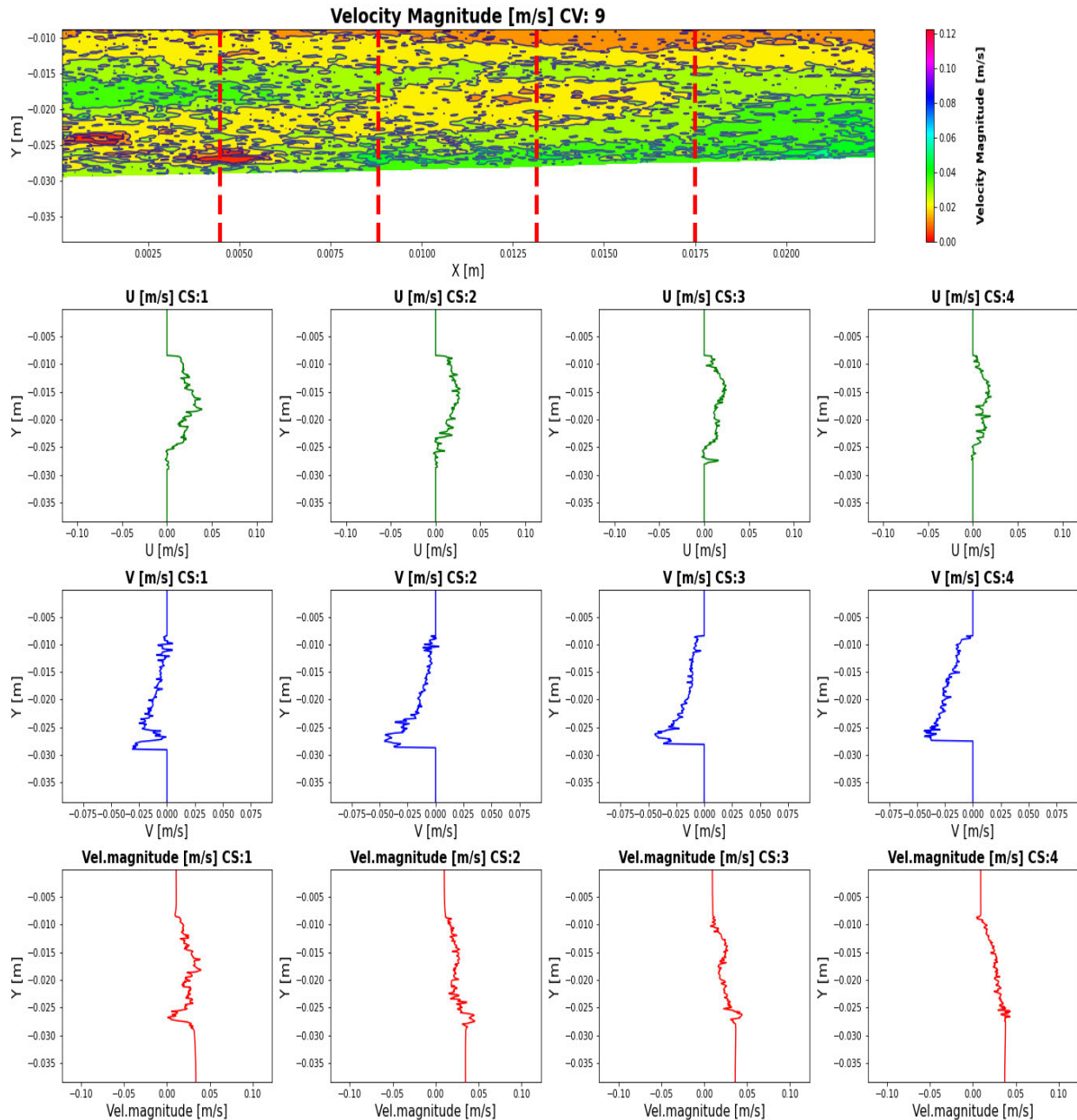


Figure 4-21: CV9: Velocity profiles at cross-sections

In Figure 4-21: CV9, the tube continues to expand. V continues to become less negative whereas U becomes increasingly more positive. The flow is pushed forward in the positive X-plane. Lower regions of the roller-tube contact remain governed by V .

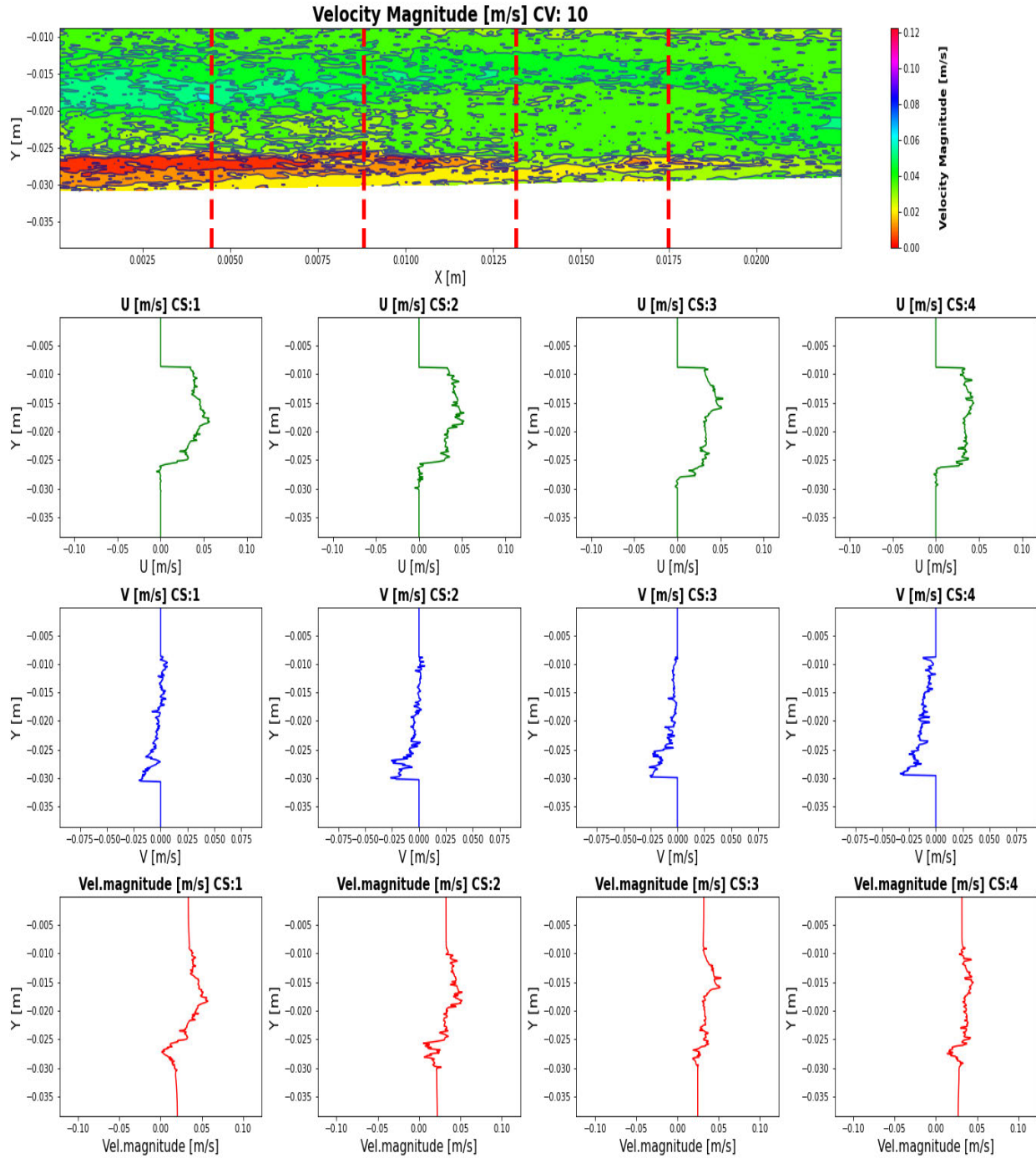


Figure 4-22: CV10: Velocity profiles at cross-sections

In Figure 4-22: CV10, the tube continues to expand. V continues to become less negative and approaches zero. U becomes increasingly more positive and the flow is propelled forward in the positive X-plane in the form of a bulge wave. Lower regions of the roller-tube contact remain governed by V .

A fluid can undergo four types of motion or deformation: translation, shear strain, linear strain and rotation all of which occur simultaneously (Çengel and Cimbala 2006). Parameters of a fluid in constant motion can be described in terms of rates. The fluid within the FPB is displaced under the deformation of the tube. As the fluid moves it is subject to a shear force. The shear strain rate (ε_{xy}) can be defined as half the rate of decrease of an angle between two initially perpendicular lines that intersect at a point (Çengel and Cimbala 2006):

$$\varepsilon_{xy} = \frac{1}{2} \left(\frac{\partial u}{\partial y} + \frac{\partial v}{\partial x} \right) \quad (27)$$

The shear stress is derived from the velocity components and therefore provides a good relation to the velocity gradient within the fluid flow, based on the linear relation to Newton's law of friction (Kundu 2003). Shear layers, therefore, occur at regions of fluctuating velocity. Shear is a tangential fluid stress acting parallel to an infinitesimal fluid element. When two parallel flows, of differing velocities, meet it is termed a shear layer. Shear stresses in a fluid are more dependent on the intermolecular cohesive forces than by the thermal motion of molecules (Kundu 2003). Within a boundary layer, the momentum transport is largely affected by the viscous forces, which resist shear deformation. Within the formation of a shear layer, the flow is not dominated by viscous forces but by the turbulent transfer of momentum. Shear stresses generate unstable fluctuations in momentum which drive turbulent mixing. In a mixing layer particles of differing momentum exchange energy. The shear layer acts as a source of energy towards turbulent fluctuations and is therefore observed as a mixing layer.

At CV1 a strong positive shear layer is observed detached from the lower boundary of the tube (Figure 4-23). An additional nineteen equidistant cross-sectional velocity profiles were extracted across each control volume to observe the changes in the velocity parameters within closer proximities (Appendix A). Between CS 1-6, of the full cross-sectional extraction (Appendix A) the v velocity contains a rapid change in the velocity gradient, from a negative to positive, within the lower regions of the tube; indicated by the sharp spike in velocity along the v velocity profile (Appendix A). However, the upper regions maintained a gradually negative v velocity gradient trend. For the laminar flow in

pipes a typical velocity profile is parabolic. In turbulent flow however the velocity profile becomes flatter with a sharp drop near the pipe wall (Çengel and Cimbala 2006). The u velocity profile held a sharp negative velocity gradient along the lower region of the tube across all cross-sectional velocity profiles (Appendix A).

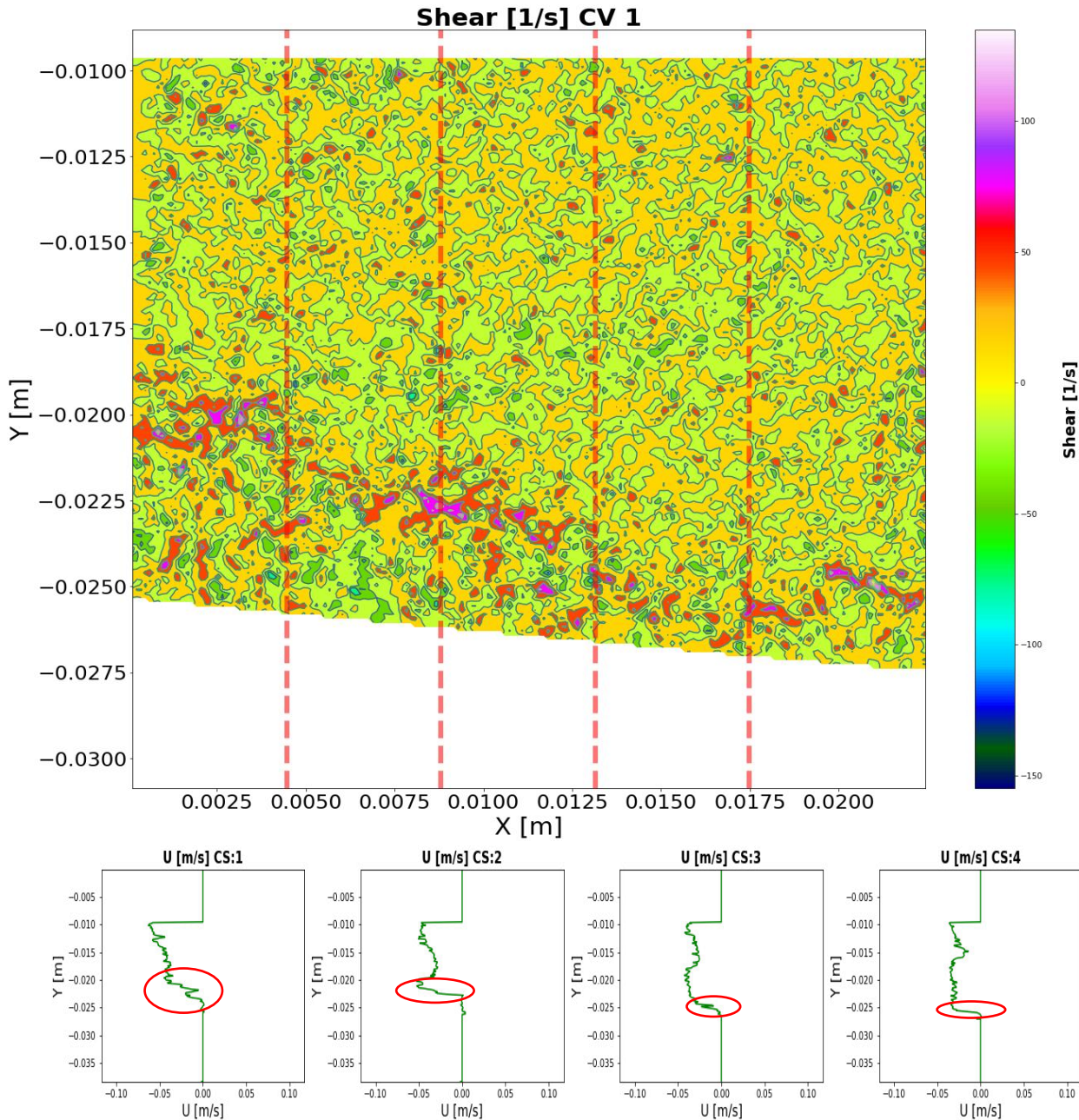


Figure 4-23: Shear rate at CV1 and the U velocity cross-sections along corresponding cross-sectional lines. U profiles hold a negative velocity gradient (Circled)

The lower regions of the tube were observed to hold a linear u velocity relationship between CS 1-10. This can be attributed to the no-slip condition and a viscous sublayer in which a velocity profile remains relatively linear. The thickness of the viscous sublayer plays an important role in the characteristics of the flow as it generates large velocity gradient potential (Çengel and Cimbala 2006). Above the sublayer lies a turbulent shear layer in which the flow becomes unstable. This is observed by the sharp negative velocity gradient within the lower regions of the u velocity profile (Appendix A and B). Within CV1, the strong positive shear layers corresponded to points along the negative u velocity profile in which the velocity gradient decreased rapidly (Figure 4-23). Negative and/or zero shear was observed within the upper regions of the tube due to minimal changes in both the u and v velocity profiles.

Observing CVs 1-10, from Figure 4-4, the U_{Mean} velocity was observed to peak negatively in accordance with the $Roller_{peak\ position}$; whereas the V_{Mean} velocity was observed to decrease on the LHS of the $Roller_{peak\ position}$ and increase on the RHS of the $Roller_{peak\ position}$ provided the tube had not reached a period of free expansion. As the fluid aims to overcome the roller constriction the flow accelerates. The pressure within this region therefore decreases. Pressure and velocity are inversely proportional whereas the pressure and shear are directly proportional. According to (Bernard and Handler 1990), on the downstream end of a curved boundary layer, the velocity decreases. As the fluid is free of the constriction the flow decelerates and the pressure within the region increases. The velocity profile is therefore subject to an inflection point. An inflection point along a velocity profile signifies an adverse pressure gradient and a consequent region in which the flow slows down. A decelerating pressure gradient promotes an increase in the boundary layer thickness (Bernard and Handler 1990). Rapid growth in the thickness of the boundary layer generates a flow separation. Under a relatively strong adverse pressure gradient, flows near a wall reverse their direction resulting in a backward flow. A separation point is defined as a boundary between the forward and backward flow where stress vanishes (Bernard and Handler 1990). The effect of the boundary layer on the adverse pressure gradient is dependent on the geometry of the flow and whether it is laminar or turbulent.

Boundary layers generate the largest degree of turbulence due to the no-slip condition (Tennekes et al. 1972). Velocity gradients are consequently stronger near the boundaries and decrease away from a boundary layer. A turbulent boundary layer is more capable of withstanding adverse pressure gradients as the velocity profile in a turbulent boundary layer holds more energy; and the separation points moves further down along a curve as wakes become narrower (Bernard and Handler 1990). The rapid changes in the velocity gradients are shown by the strong shear layers which are indicative of a separation in the flow. Full shear stress extractions between CVS 1-10 are shown in Appendix B.

Instabilities within the flow are generated due to the interaction of the boundary layer and the peristaltic motion of the tube. Between CVs 2-9 there is a breakdown in the positive shear and a consequent breakdown in turbulence. Eddies break down shear in a chaotic motion (Kundu 2003). CVs 2-9 are identified as possible chaotic mixing regions where the mean flow changes direction. The breakdown in shear between CVs 2-9 are observed as pockets of positive and negative shear present within the FOV (Appendix B). Between CVs 1-6, pockets of strong positive shear were observed to lie within the lower regions of the tube and within close proximity to the *Roller_{peak position}*. Whereas pockets of negative shear were observed within the mid-region of the tube overlaying the strong positive shear layer. Between CVs 6-10 the tube is free from the direct roller constriction and is given the freedom to expand. As the tube expands the flow is thrust forward in the form of a bulge wave. Both U_{Mean} and V_{Mean} increase between CVs 6-10. Pockets of negative shear overcome the fluid (Appendix B).

At CV10 the flow is subject to a strong negative shear within the lower regions of the tube (Figure 4-24). The lower region of the u velocity profiles maintained a linear relationship within the boundary layer. The strong negative shear layer is observed to correspond to the spike in the positive u velocity gradient as the u profile tends toward the right. A possible mixing region is identified between CVs 2-9 as the fluid is subject to a chaotic change in the mean flow direction. The potential timescale for mixing is therefore observed at approximately 0.133 seconds between CVs 2-9 (16 frames shot at 120 Fps).

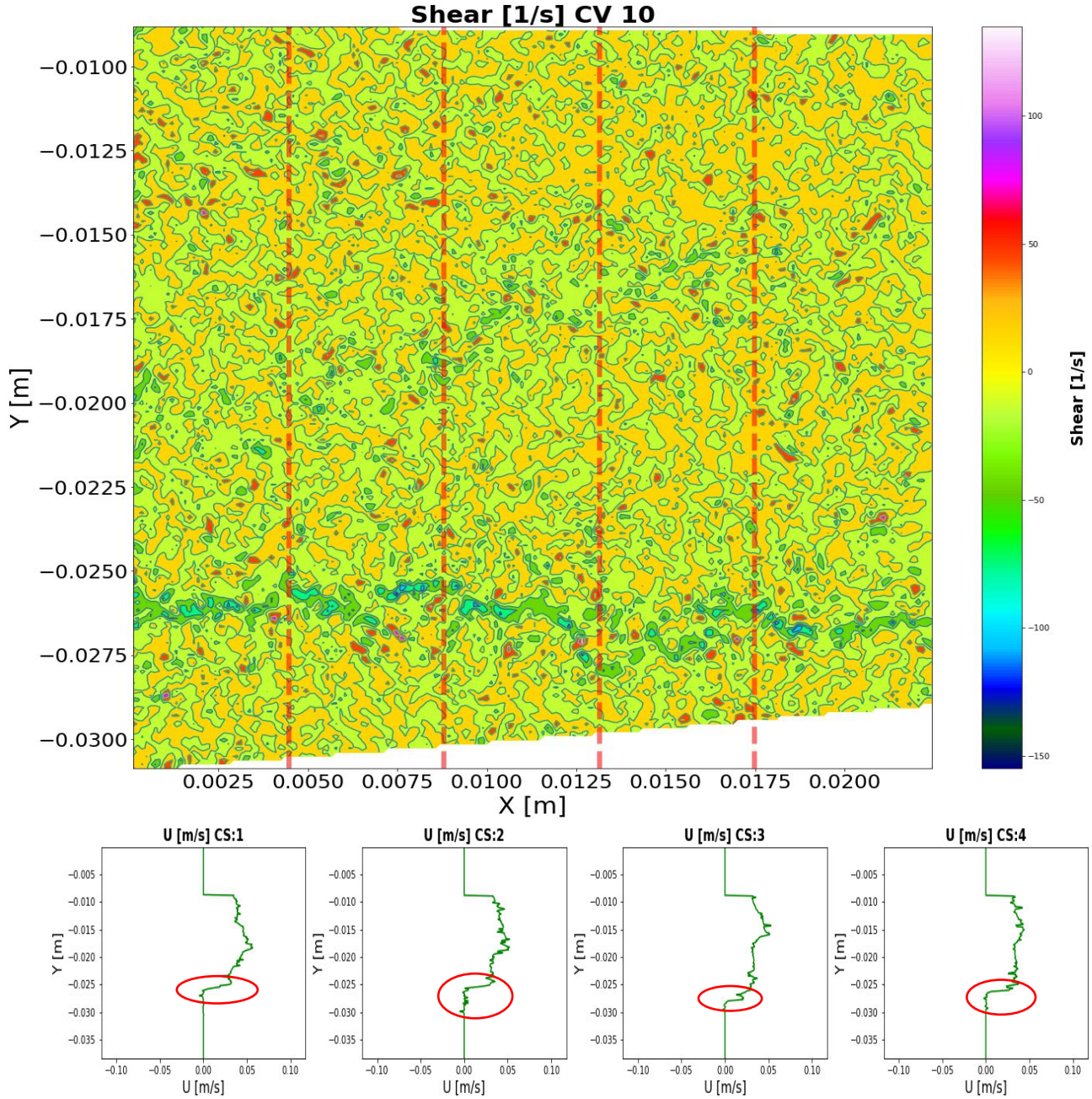


Figure 4-24: Shear rate at CV10 and the U velocity cross-sections along corresponding cross-sectional lines. U profiles hold a negative velocity gradient (Circled)

The linear strain rate (ϵ_{Total}); and can be defined as the rate of increase in length per unit length (Çengel and Cimbala 2006). A positive linear strain rate indicates a stretching whereas a negative value indicates a shrinking along each plane.

$$\epsilon_{Total} = \epsilon_{xx} + \epsilon_{yy} = \frac{\partial u}{\partial x} + \frac{\partial v}{\partial y} \quad (28)$$

A fluid is subject to both tangential and normal stresses. Normal stresses contribute very little to the transport of mean momentum (Tennekes et al. 1972). Strain deformations are applied perpendicular to the fluid element whereas shear deformations are applied parallel. The relationships observed in the strain rates correspond with the observations made in the shear plots (Figure 4-23 and 4-24 and Appendix B). The strain rate full extraction plots can be found in (Appendix C).

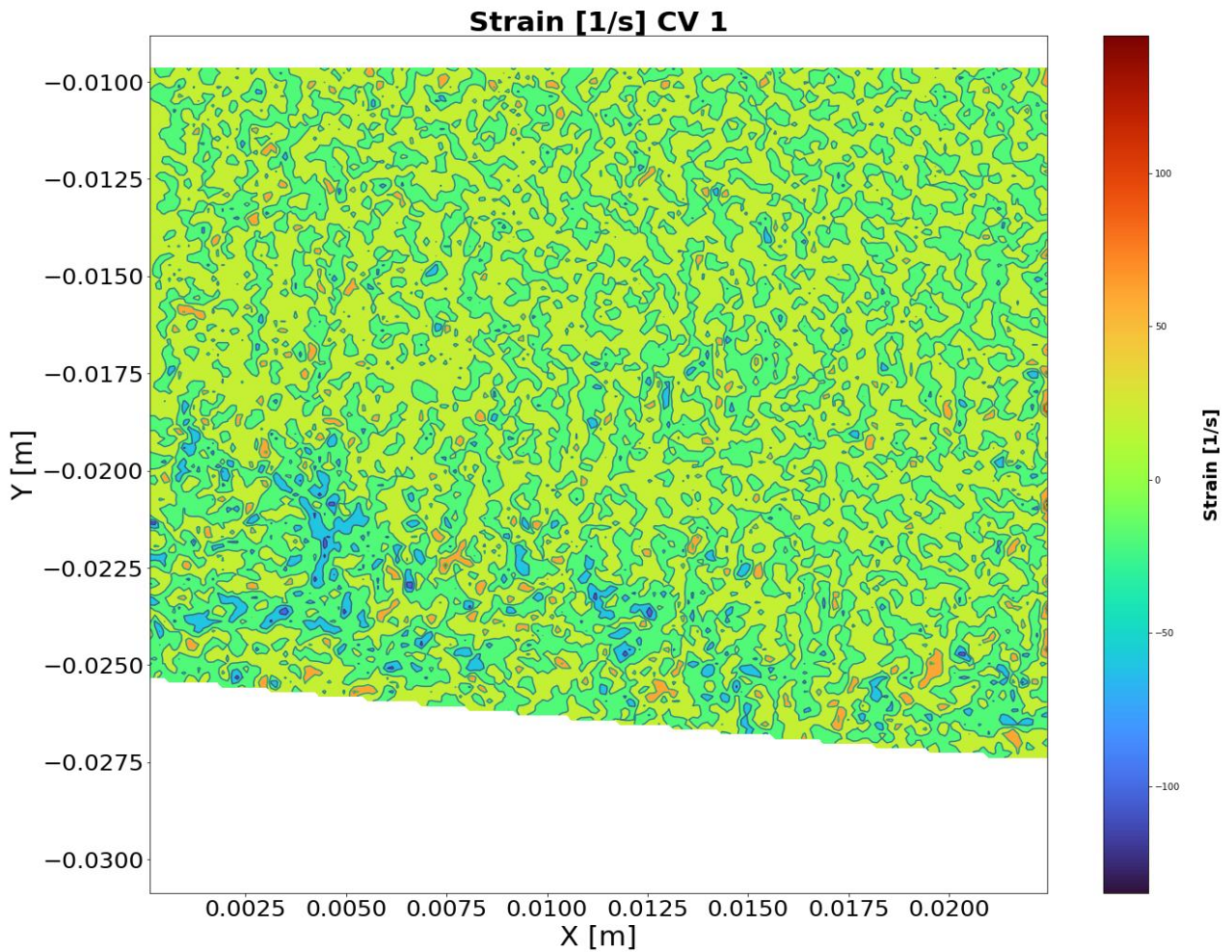


Figure 4-25: Strain rate at CV1

Within CV1 (Figure 4-25), a strong negative strain layer was observed to correspond with the prominent positive shear layers in Figure 4-23 of CV1. Along the full cross-sectional velocity extraction (Appendix A) the v velocity profile tends right and positively in the lower regions of the tube. At CV10 (Figure 4-26) the strain is more dispersed however packets

of both positive and negative strain are observed to correspond in position to the strong negative shear layer of Figure 4-24.

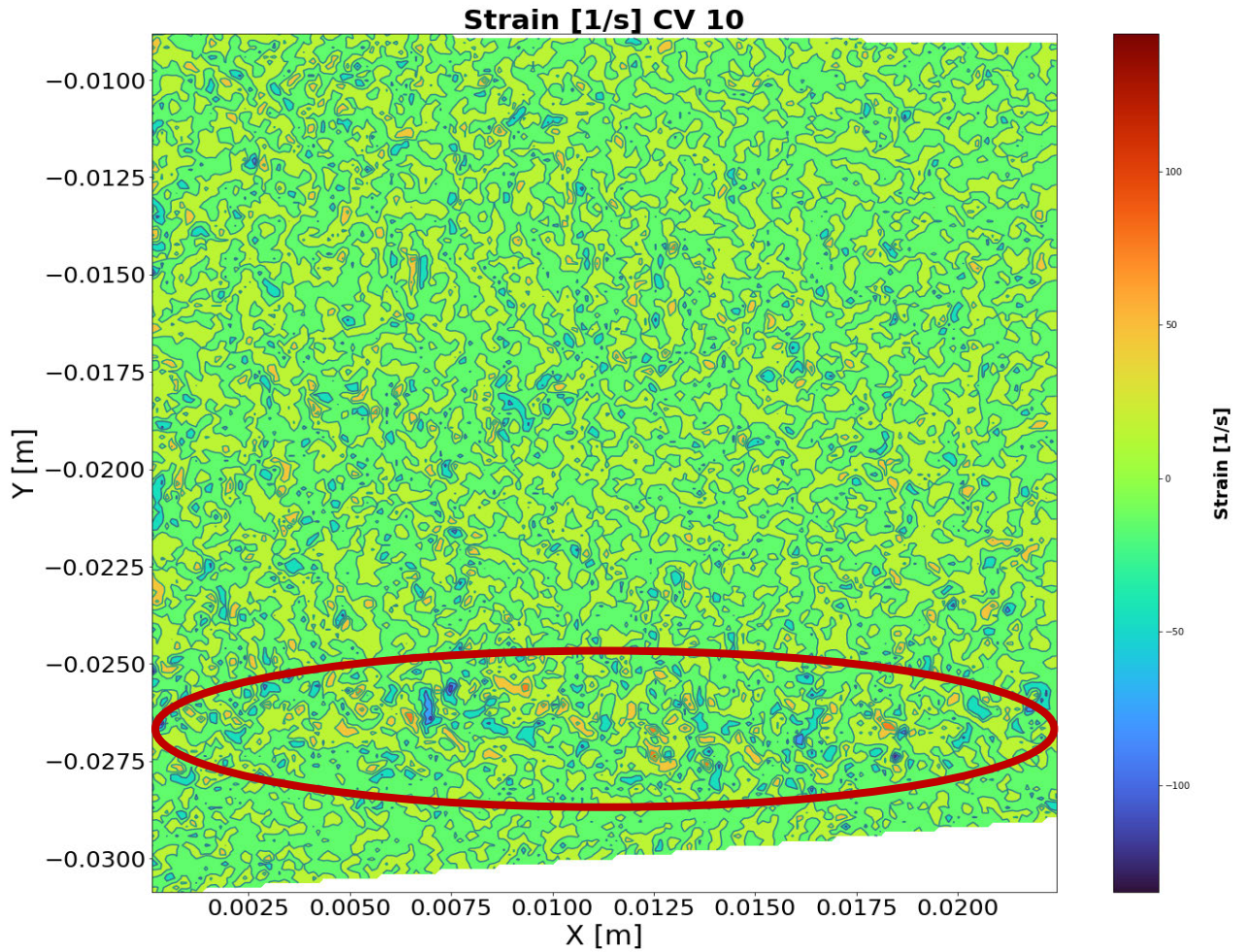


Figure 4-26: Strain rate at CV10. Condensed pockets of positive and negative strain which correspond in position to the strong negative shear layer.

The vector rate of translation (V) can be expressed as:

$$V = u_i + v_j \quad (29)$$

The rate of rotation (ω) of a fluid element can be expressed as:

$$\omega = \frac{1}{2} \left(\frac{\partial v}{\partial x} - \frac{\partial u}{\partial y} \right) \quad (30)$$

The vorticity vector is defined as the curl of the velocity vector (V) and is a measure of the rotation of a fluid particle. The rate of the rotation of the rotation vector is equal to half the vorticity vector:

$$\zeta = \nabla \times V \tag{31}$$

$$\therefore \omega = \frac{1}{2} (\nabla \times V) = \frac{\zeta}{2} \tag{32}$$

$$\therefore \zeta = 2\omega \tag{33}$$

Where ζ is the vorticity is vector and ∇ is the curl of the velocity vector. If the vorticity is nonzero the flow is rotational. The vorticity is defined as twice the angular momentum (ω).

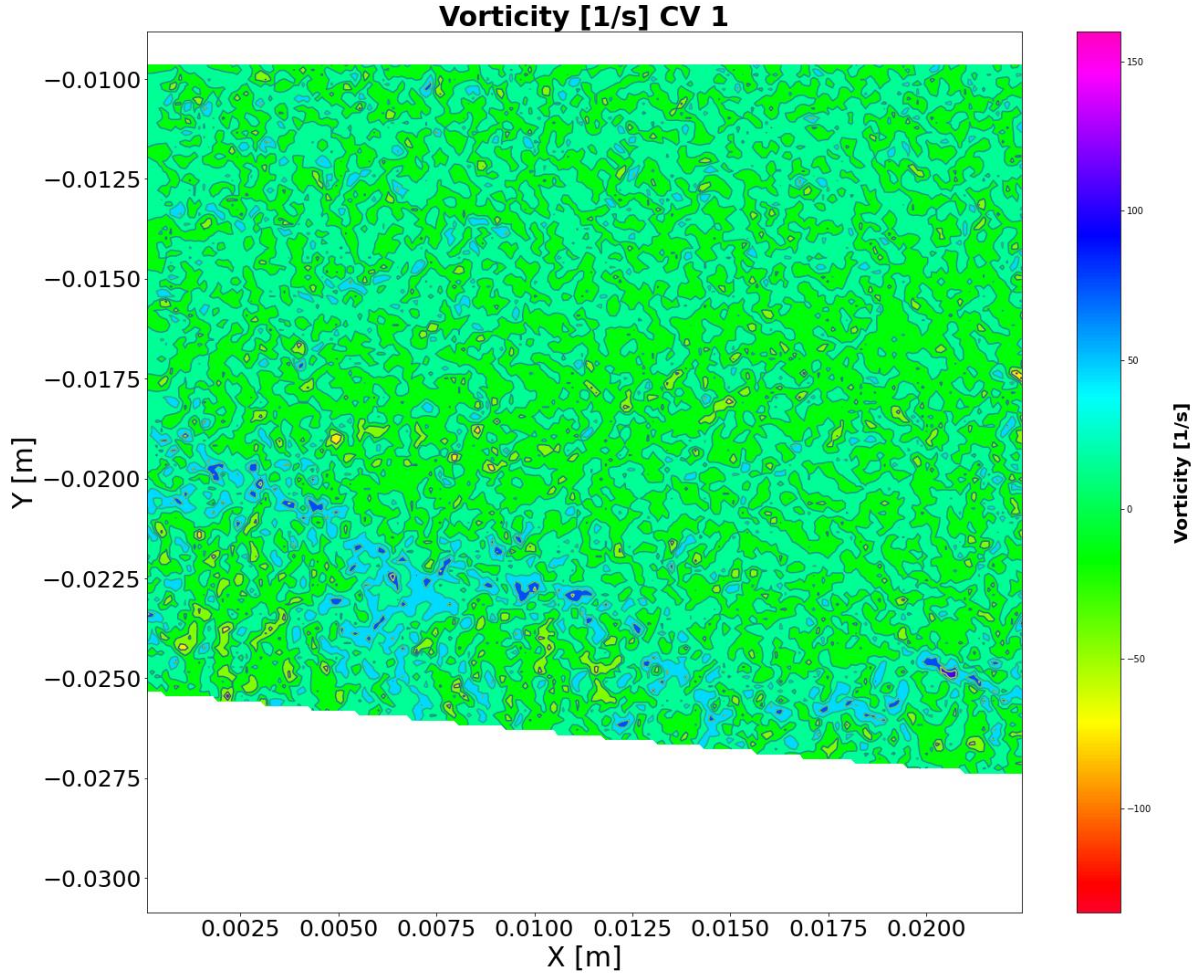


Figure 4-27: Vorticity at CV1

Strong positive regions of vorticity coincide with the shear layer observed in Figure 4-23. This is due to the large velocity gradients observed within these portions of the flow (Appendix A). The magnitude of the vorticity is highest in regions where the spatial derivatives of the velocity are high (Çengel and Cimbala 2006). Vortex flows are flow motion in a circular path. Motion on the outside of a vortex core is assumed to be irrotational (Kundu 2003). Velocity potential exists in all irrotational flows. Vortices placed within close proximity to one another can interact mutually. Either rotational or irrotational vortices may exist depending on whether fluid particles hold vorticity or not. A positive vorticity is observed in Figure 4-27 and indicates an anti-clockwise rotation. Large scale eddies are responsible for the bulk of particle and momentum transport. Whereas small eddies are statistically independent of the mean flow due to their small timescales (Tennekes et al. 1972). The concentration of the vorticity is observed to lessen as the vorticity diffuses on the downstream end (Figure 4-27).

The nature of turbulent flow can be characterised by high levels of fluctuating vorticity. Turbulent flows are often independent of viscosity except at very small scales of motion. The most powerful eddies are those which can absorb the energy from the shear flow effectively; and whose principle axis is roughly aligned with that of the mean strain rate (Tennekes et al. 1972). Powerful vortices therefore have a strong correlation between the shear and strain rates. The scale of the eddies decrease as the strain rate increases (Tennekes et al. 1972). The energy dissipation from large scale to small scale eddies is termed vortex stretching.

The shear and strain rates are observed in CV1 (Figures 4-23 and 4-25). A strong positive shear rate coincided with a strong negative strain rate and an overall positive vorticity (anti-clockwise rotation) (Figure 4-27). Between CVs 2-6, the pockets of positive vorticity moved within close proximity to the roller position along the tube (Appendix D). Under unrestricted tube expansion, between CVs 6-9, there was a dissipation in the positive vorticity and the formation of a negative vorticity layer in CV10. CV 10 held strong negative vorticity (clockwise rotation) (Figure 4-28). The negative vorticity layer coincided with a strong negative shear rate (Figure 4-23) and a dispersed region of positive and negative strain (Figure 4-26).

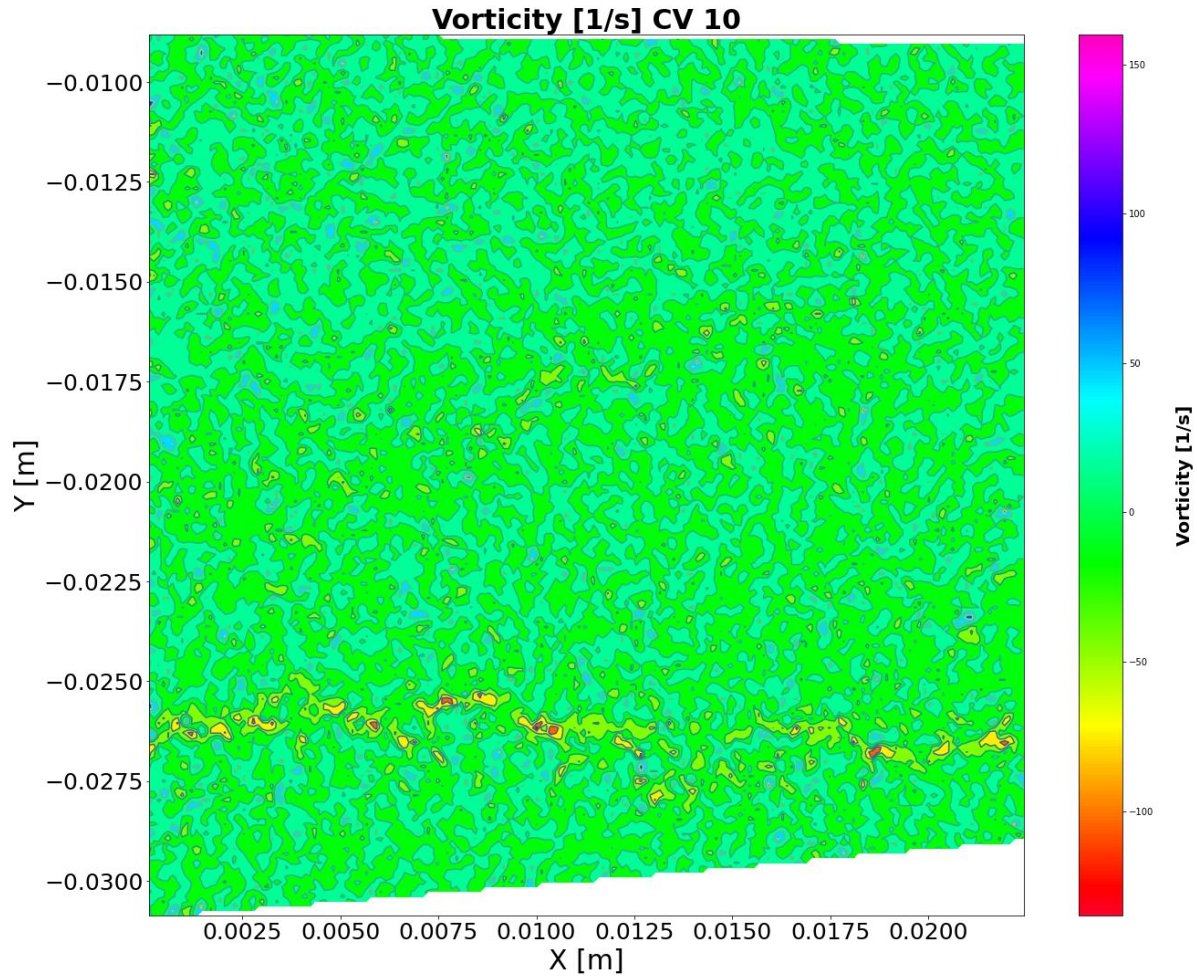


Figure 4-28: Vorticity at CV10

The parameters of the flow are observed from an Eulerian approach in which the flow was quantified in the spatial domain. The flow was therefore observed from a stationary point of view. To better interpret/simplify the essential parameters of the fluid an observation point is established relative to the roller; as the roller moves at the same speed as the boundary layer. Galilean invariance states that the laws of motion are the same in all inertial frames (Lévy-Leblond 1971). Galilean transformation is used to transform co-ordinates from separate reference frames which differ only by a constant relative motion. An inertial frame of reference is taken as a stationary point on the roller. We therefore subtract the roller speed from the horizontal velocity components. As shear, strain and vorticity are a function of the velocity gradient they remained unchanged. The results of the Galilean transformation are shown in Figures 4-29 to 4-30.

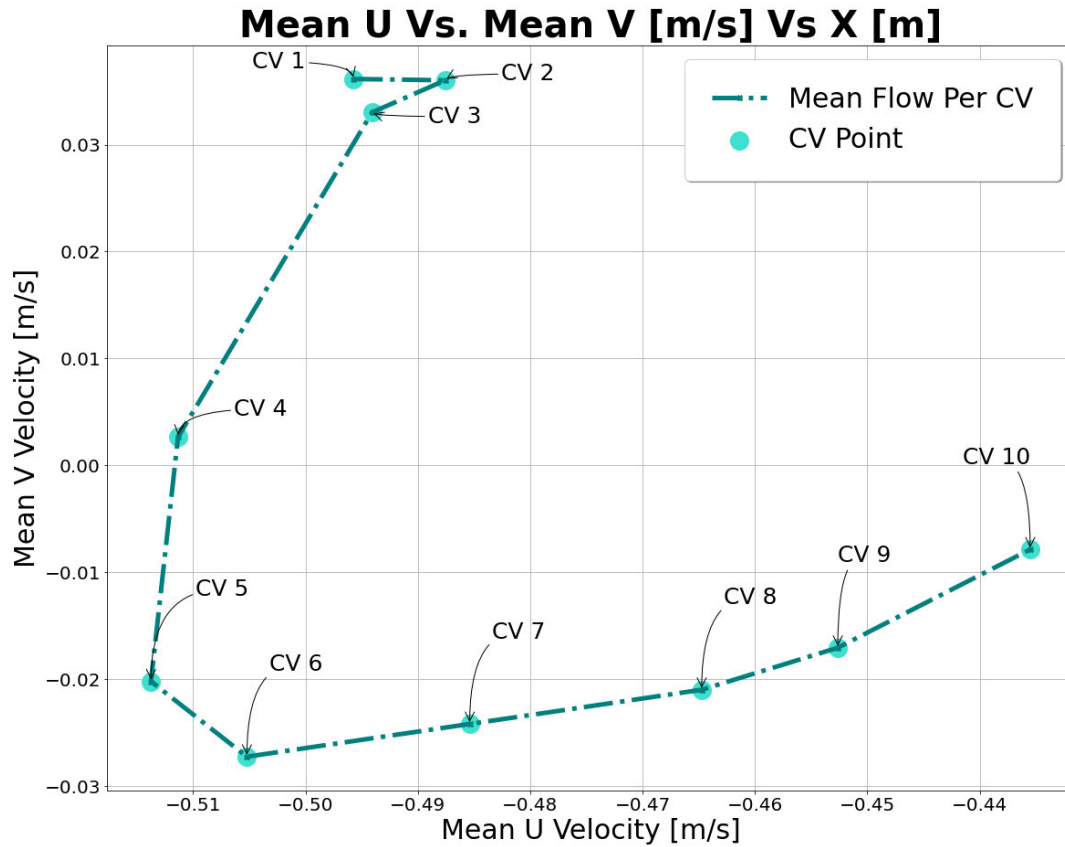


Figure 4-29: Mean velocity components relative to the roller speed

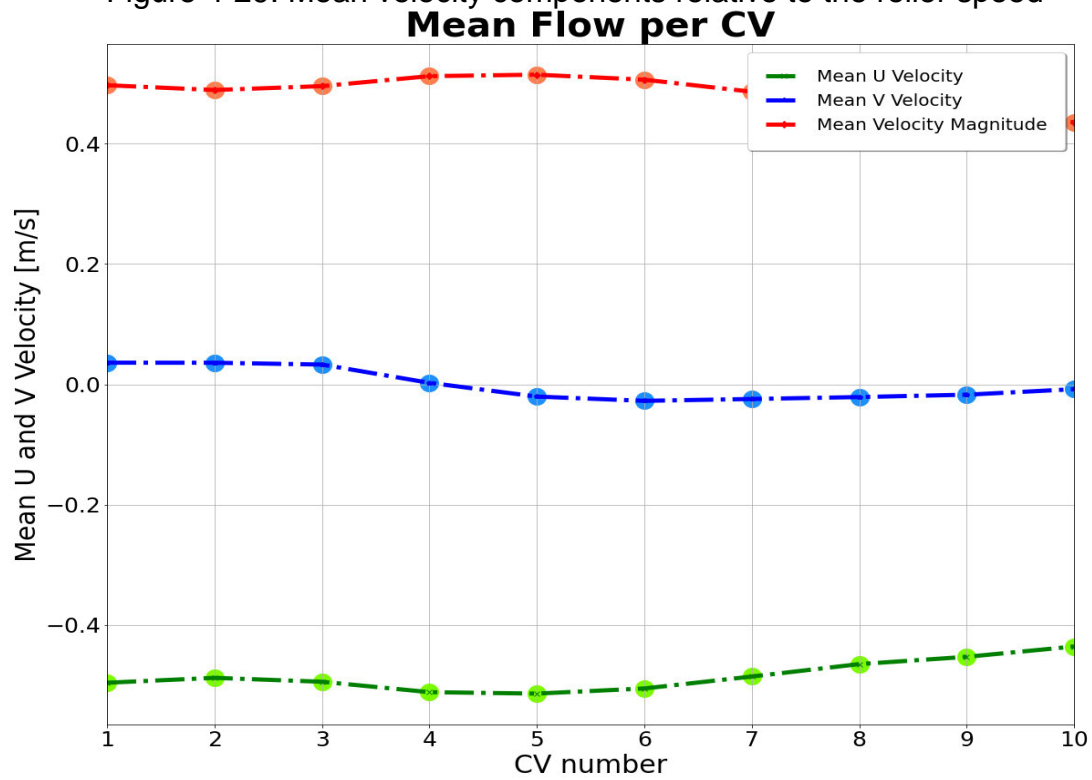


Figure 4-30: Mean U and V velocity across CVs 1-10

CHAPTER 5: REVIEW AND CONCLUSIONS

This study analysed the flow in a physical FPB model under the influence of an idealised pressure constriction. The application of a roller mechanism on the lower boundary of a flexible tube generated a transfer in pressure within the FPB. Oscillations in the tubes cross-sectional profile generated a pumping action which drives a complex internal collapsible flow. The interaction of the tubes peristaltic motion on the internal fluid structure was investigated using PIV in order to observe and quantify essential parameters of the flow. The effective illumination of the fluid tracer particles was essential in improving the overall accuracy of the fluid flow measurement. In order to optimize the rendering quality of the flow within PIVlab the light refraction conditions of the experimental setup were ensured to be optically non-invasive. Following a Eulerian approach, the flow was quantified in the spatial domain. Further parameters of the flow were extracted by manipulating raw pixel-displacement data in Python.

An idealised pressure (roller mechanism) moved along the lower boundary of the FPB at 0.466 m/s from left to right. Changes in the internal fluid flow structure were observed. Within the initial region of tube constriction, U_{mean} was observed to initially move in the direction of the pressure/roller (positively). However under the gradual introduction of the constriction into the FOV, the U_{mean} moved negatively, opposing the direction of the pressure/roller. This was observed as a drawback motion of the fluid. U_{Mean} was observed to peak negatively in accordance with the $Roller_{peak\ position}$. Under tube expansion the U_{Mean} was found to increase positively resulting in a positive forward thrust of the fluid in the form of a bulge wave. Within regions of direct pressure/roller constriction, V_{mean} was observed to decrease on the LHS of the $Roller_{peak\ position}$ and increase on the RHS of the $Roller_{peak\ position}$ provided the tube had not reached a period of free expansion. Under full tube expansion (as the tube aims to restore its original cross-sectional area and equalize its internal pressure), V_{mean} increases and approaches zero; as the bulk of the flow is dominated by U_{mean} . The magnitude of the velocity was observed to increase in regions of tube constriction and decrease under tube expansion. However, within the final stages of tube expansion (in which a bulge wave is present) the velocity magnitude

increases again, where the bulk of the magnitude is held by the horizontal velocity component. The mean overall internal fluid flow was observed to hold an anticlockwise motion within the FPB.

Equidistant cross-sectional velocity profiles were extracted across each control volume to observe the changes in the velocity parameters within closer proximities. Notifiable changes in the velocity gradients signified regions of stress with the fluid. Within the initial constriction zone, the fluid held a strong positive shear layer detached from the lower boundary of the tube. This corresponded to a negative U profile which tends negatively. Lower regions of the profile were observed to remain linear, indicating a viscous sublayer. Rapid changes in the velocity gradients indicated regions of flow separation. The region of strong positive shear coincided with a strong negative strain rate and anti-clockwise vorticity. Within the tube expansion zone, the fluid was found to instead have a strong negative shear rate, dispersed regions of positive and negative strain, and clockwise vorticity.

The transition in sign convention of the deformation terms indicated a breakdown in stress. A possible mixing region is identified between these transitions as the fluid is subject to a chaotic change in the mean flow direction. This is observed by packets of positive and negative shear, strain, and vorticity with the tube which broke down the shear layers. A potential timescale for mixing is therefore observed at approximately 0.133 seconds between CVs 2-9. Mixing promotes light, nutrient, and aeration exchange with microalgal cultures. However, excessive shear was shown to correlate to cell mortality, reduced cell viability, and an overall decrease in the microalgal growth rate. A shear tolerance limit should therefore be applied based on the microalgal species used. Regions of strong positive shear were shown under initial tube constriction and regions of strong negative shear were shown under full tube expansion. These are identified as regions that pose a possible threat to microalgal cells.

5.1 FUTURE APPROACH AND RECOMMENDATIONS:

Based on the marginal frictional translations experienced on from the FPB model, it is recommended that the roller and roller-track mechanism must be altered to provide a frictionless interaction. This would ensure that the roller moves smoothly against the tubes lower boundary. To optimize the accuracy of the flow measurement in PIV, the FPB should be more densely seeded to ensure at least 20 particles per IA with uncontaminated neutrally buoyant tracer particles. This limits the deceleration of particles due to gravity and therefore improves the overall quality of the fluid measurement. Measuring the internal pressure with the FPB enclosure can be done using an Audrino pressure transducer. C++ can be used to calibrate a pressure transducer. The measurement of the pressure aims to verify the regions of fluctuating velocity and link the magnitude of roller pressure to the resultant flow conditions. In order to build an improved level of confidence in the results it is recommended that numerous experimental runs are done for the same pressure constriction. The results can be overlaid to greater improve the accuracy of the relationships observed. Further experimental conditions can aim to increase the constriction pressure applied to the FPB, in order to compare how changes in the magnitude of the pressure affect the internal structure fluid.

REFERENCES:

- Barton, Charles, and Severin Raynor. 1968. 'Peristaltic Flow in Tubes'. *The Bulletin of Mathematical Biophysics* 30 (4): 663–80. <https://doi.org/10.1007/BF02476682>.
- Bernard, Peter S, and Robert A Handler. 1990. 'Reynolds Stress and the Physics of Turbulent Momentum Transport'. *Journal of Fluid Mechanics* 220: 99–124. <https://doi.org/10.1017/S0022112090003202>.
- Budwig, R. 1994. 'Refractive Index Matching Methods for Liquid Flow Investigations'. *Experiments in Fluids* 17 (5): 350–55. <https://doi.org/10.1007/bf01874416>.
- Bwapwa, Joseph K, Akash Anandraj, and Cristina Trois. 2017. 'Possibilities for Conversion of Microalgae Oil into Aviation Fuel: A Review'. *Renewable and Sustainable Energy Reviews* 80 (C): 1345–54. <https://doi.org/10.1016/j.rser.2017.05.22>. 2018. 'Microalgae Processing for Jet Fuel Production'. *Biofuels, Bioproducts and Biorefining* 12 (4): 522–35. <https://doi.org/10.1002/bbb.1878>.
- Carlozzi, Pietro. 2002. 'Dilution of Solar Radiation through Culture Lamination in Photobioreactor Rows Facing South-North: A Way to Improve the Efficiency of Light Utilization by Cyanobacteria (*Arthrospira Platensis*)'. *Biotechnology and Bioengineering* 81 (3): 305–15. <https://doi.org/10.1002/bit.10478>.
- Carlozzi, Pietro, and Giuseppe Torzillo. 1996. 'Productivity of Spirulina in a Strongly Curved Outdoor Tubular Photobioreactor'. *Applied Microbiology and Biotechnology* 45: 18–23. <https://doi.org/10.1007/s002530050642>.
- Çengel, Y A, and J M Cimbala. 2006. *Fluid Mechanics: Fundamentals and Applications*. Fluid Mechanics: Fundamentals and Applications. McGraw-HillHigher Education. <https://books.google.co.za/books?id=4RVEAQAAIAAJ>.
- Chisti, Yusuf. 2007. 'Biodiesel From Microalgae'. *Biotechnology Advances* 25: 294–306.

<https://doi.org/10.1016/j.biotechadv.2007.02.001>.

Dean, Robert G, and Robert A Dalrymple. 1991. *Water Wave Mechanics for Engineers and Scientists*. World Scientific. <https://doi.org/10.1142/1232>.

European Commission, Directorate-General, and Innovation. 2012. *Innovating for Sustainable Growth: A Bioeconomy for Europe*. Publications Office of the European Union.

Flynn, Kevin J. 2019. 'Enhancing Microalgal Production'. *Enhance Microalgae*.

Grotberg, James B, and Oliver E Jensen. 2004. 'Biofluid Mechanics In Flexible Tubes'. *Annual Review of Fluid Mechanics* 36 (1): 121–47. <https://doi.org/10.1146/annurev.fluid.36.050802.121918>.

Hadad, T, and Roi Gurka. 2013. 'Effects of Particle Size, Concentration and Surface Coating on Turbulent Flow Properties Obtained Using PIV/PTV'. *Experimental Thermal and Fluid Science* 45: 203–212. <https://doi.org/10.1016/j.expthermflusci.2012.11.006>.

Handapangoda, Harshani, S A Galindo-Torres, and Alexander Scheuermann. 2015. 'Particle Image Velocimetry with High Power Light Emitting Diodes for Flow through Porous Medium'. In . <https://doi.org/10.2495/MPF150421>.

Huang, Qingshan, Fuhua Jiang, Lianzhou Wang, and Chao Yang. 2017. 'Design of Photobioreactors for Mass Cultivation of Photosynthetic Organisms'. *Engineering* 3 (3): 318–29.

Hung, Tin-Kan, and Thomas D Brown. 1976. 'Solid-Particle Motion in Two-Dimensional Peristaltic Flows'. *Journal of Fluid Mechanics* 73 (1): 77–96. <https://doi.org/10.1017/S0022112076001262>.

IEA World Energy Outlook. 2009. *IEA World Energy Outlook*. Reference. Paris.

- Javanmardian, Minoo, and Bernhard O Palsson. 1991. 'High-Density Photoautotrophic Algal Cultures: Design, Construction, and Operation of a Novel Photobioreactor System'. *Biotechnology and Bioengineering* 38 (10): 1182–89. <https://doi.org/10.1002/bit.260381010>.
- Kenny, Philip, and Kevin J Flynn. 2017. 'Physiology Limits Commercially Viable Photoautotrophic Production of Microalgal Biofuels'. *Journal of Applied Phycology* 29 (6): 2713–27. <https://doi.org/10.1007/s10811-017-1214-3>.
- Khan, Muhammad Imran, Jin Hyuk Shin, and Jong Deog Kim. 2018. 'The Promising Future of Microalgae: Current Status, Challenges, and Optimization of a Sustainable and Renewable Industry for Biofuels, Feed, and Other Products'. *Microbial Cell Factories* 17 (1). <https://doi.org/10.1186/s12934-018-0879-x>.
- Kompenhans, Juergen, M Raffel, Lutz Dieterle, Tim Dewhurst, H Vollmers, K Ehrenfried, Christian Willert, et al. 1999. 'Particle Image Velocimetry in Aerodynamics: Technology and Applications in Wind Tunnels'. In .
- Kundu, P. 2003. *Fluid Mechanics 2nd Edition*. Elsevier Exclusive. <https://books.google.co.za/books?id=9MTCbwAACAAJ>.
- Lévy-Leblond, Jean-Marc. 1971. 'Galilei Group and Galilean Invariance'. In *Group Theory and Its Applications*, 221–99. Elsevier.
- Maulud, A L, and H Saidi. 2012. 'The Malaysian Fifth Fuel Policy: Re-Strategising the Malaysian Renewable Energy Initiatives'. *Energy Policy* 48: 88–92. <https://doi.org/https://doi.org/10.1016/j.enpol.2012.06.023>.
- Muthu, P, B V Kumar, and Peeyush Chandra. 2001. 'Peristaltic Motion in Circular Cylindrical Tubes: Effect of Wall Properties.' *Indian Journal of Pure and Applied Mathematics* 32.
- Pedley, T J, and D Pihler-Puzovic. 2015. 'Flow and Oscillations in Collapsible Tubes: Physiological Applications and Low-Dimensional Models'. *Sadhana* 40 (3): 891–909.

<https://doi.org/10.1007/s12046-015-0363-9>.

Qiang, Hu, Hugo Guterman, and Amos Richmond. 1996. 'Physiological Characteristics Of *Spirulina Platensis* Cyanobacteria Cultured At Ultrahigh Cell Densities'. *Journal of Phycology* 32 (6): 1066–73. <https://doi.org/10.1111/j.0022-3646.1996.01066.x>.

Reeve, Dominic, Andrew Chadwick, and Christopher Fleming. 2012. *Coastal Engineering: Processes, Theory and Design Practice*. CRC Press.

Ren, Rui, Xue Han, Haiping Zhang, Hongfei Lin, Jianshe Zhao, Ying Zheng, and Hui Wang. 2018. 'High Yield Bio-Oil Production by Hydrothermal Liquefaction of a Hydrocarbon-Rich Microalgae and Biocrude Upgrading'. *Carbon Resources Conversion* 1 (2): 153–59. <https://doi.org/10.1016/j.crcon.2018.07.008>.

Singhasuwan, Somruethai, Wanna Choorit, Sarote Sirisansaneeyakul, Nakhon Kokkaew, and Yusuf Chisti. 2015. 'Carbon-to-Nitrogen Ratio Affects the Biomass Composition and the Fatty Acid Profile of Heterotrophically Grown *Chlorella* Sp. {TISTR} 8990 for Biodiesel Production'. *Journal of Biotechnology* 216 (December): 169–77. <https://doi.org/10.1016/j.jbiotec.2015.10.003>.

Sokoray-Varga, Béla, and János Józsa. 2008. 'Particle Tracking Velocimetry (PTV) and Its Application to Analyse Free Surface Flows in Laboratory Scale Models'. In .

Steenbergen, Wiendelt. 1996. 'Reduction of Beam Refraction in Optical Pipe Flow Experiments by Use of Sheet-Fabricated Pipe Walls'. *Experiments in Fluids* 22: 165–73. <https://doi.org/10.1007/s003480050034>.

Tennekes, Hendrik, John Leask Lumley, Jonh L Lumley, and others. 1972. *A First Course in Turbulence*. MIT press.

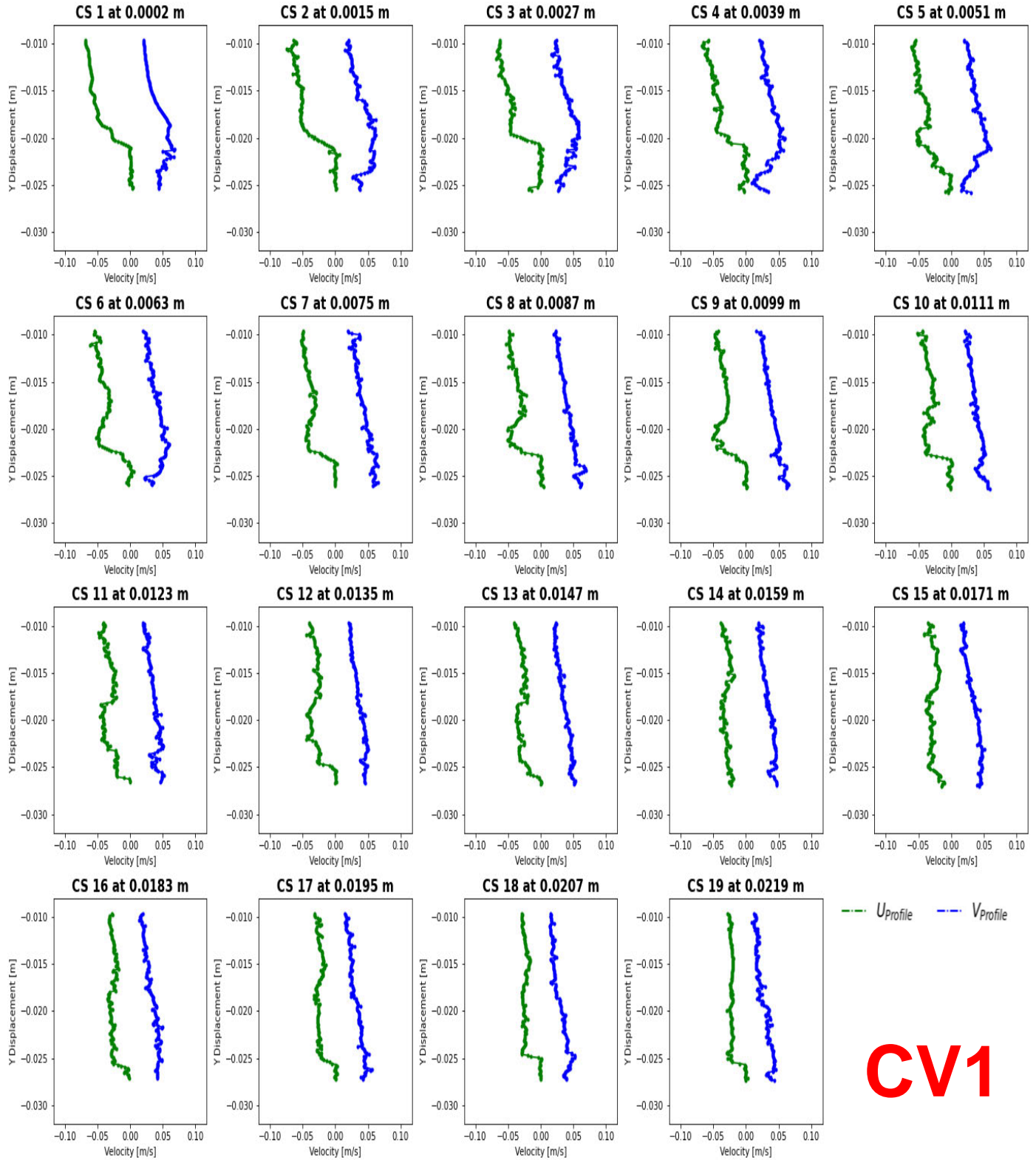
Thielicke, William, and Rene Sonntag. 2021. 'Particle Image Velocimetry for MATLAB: Accuracy and Enhanced Algorithms in PIVlab'. *Journal of Open Research Software* 9. <https://doi.org/10.5334/jors.334>.

- Thielicke, William, and Eize Stamhuis. 2014. 'PIVlab – Towards User-Friendly, Affordable and Accurate Digital Particle Image Velocimetry in MATLAB'. *Journal of Open Research Software* 2. <https://doi.org/10.5334/jors.bl>.
- Trent, Jonathan. 2012. 'Offshore Membrane Enclosures for Growing Algae (OMEGA): A Feasibility Study for Wasterwater to Biofuels - Final Project Report', no. CEC-500-2013-143. <http://www.energy.ca.gov/2013publications/CEC-500-2013-143/CEC-500-2013-143.html>.
- U.S. EIA. 2010. *Annual Energy Outlook 2009: Updated Reference Case. Annual Energy Outlook 2009: Updated Reference Case*. Washington, DC: U.S. Energy Information Administration.
- Ugwu, C U, Hi Aoyagi, and H Uchiyama. 2008. 'Photobioreactors for Mass Cultivation of Algae'. *Bioresource Technology* 99 (10): 4021–28.
- Wang, Chinchin, and Christopher Lan. 2018. 'Effects of Shear Stress on Microalgae – A Review'. *Biotechnology Advances* 36 (March). <https://doi.org/10.1016/j.biotechadv.2018.03.001>.
- Xue, Zhenyu, John J Charonko, and Pavlos P Vlachos. 2014. 'Particle Image Velocimetry Correlation Signal-to-Noise Ratio Metrics and Measurement Uncertainty Quantification'. *Measurement Science and Technology* 25 (11): 115301. <https://doi.org/10.1088/0957-0233/25/11/115301>.
- Yin, F C P, and Y C Fung. 1971. 'Comparison of Theory and Experiment in Peristaltic Transport'. *Journal of Fluid Mechanics* 47 (1): 93–112. <https://doi.org/10.1017/s0022112071000958>.
- Yin, F, and Y C Fung. 1969. 'Peristaltic Waves in Circular Cylindrical Tubes'. *Journal of Applied Mechanics* 36 (3): 579–87. <https://doi.org/10.1115/1.3564720>.
- Yousif, Majid Y, David W Holdsworth, and Tamie L Poepping. 2010. 'A Blood-Mimicking Fluid for Particle Image Velocimetry with Silicone Vascular Models'. *Experiments in*

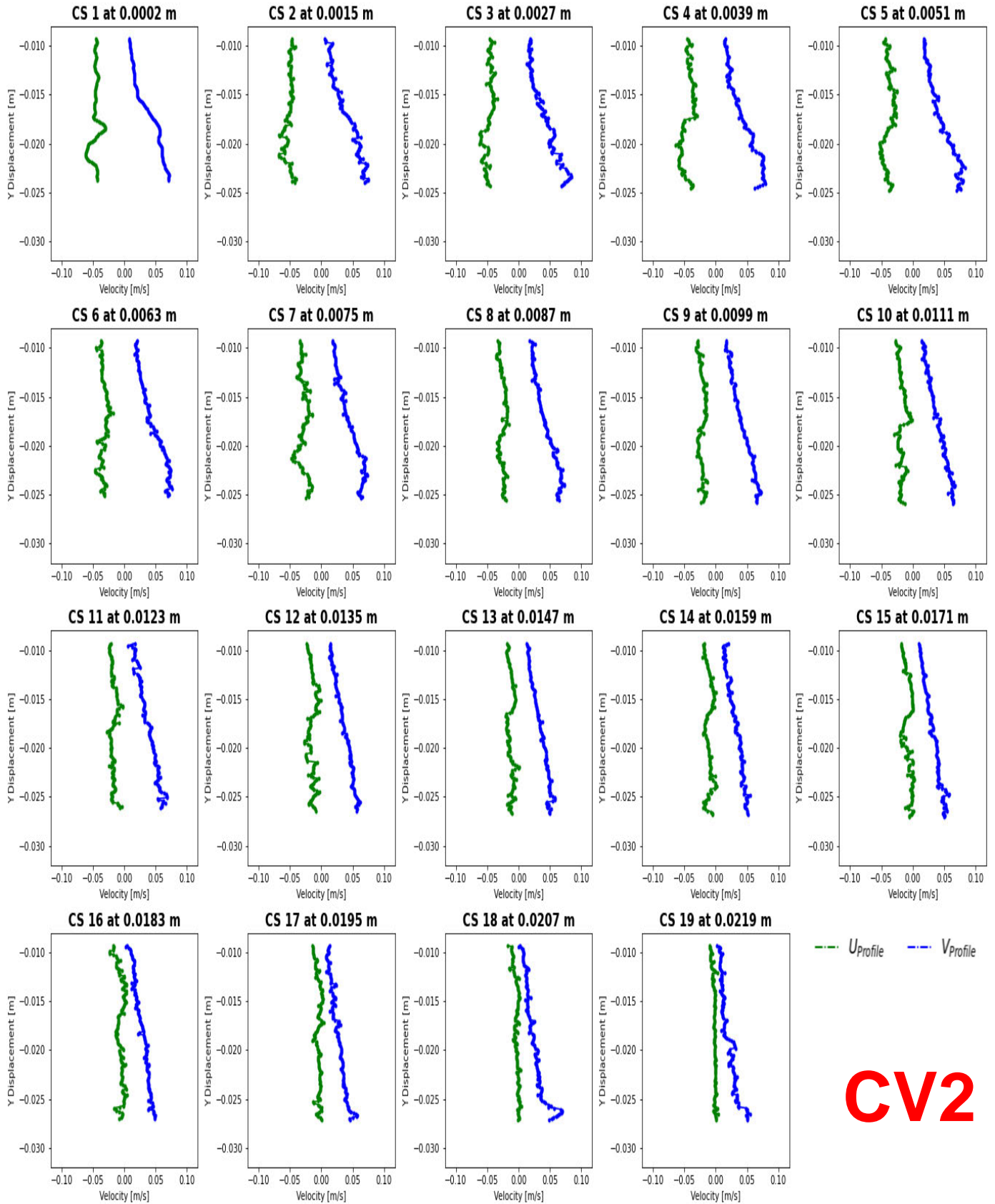
Fluids 50 (3): 769–74. <https://doi.org/10.1007/s00348-010-0958-1>.

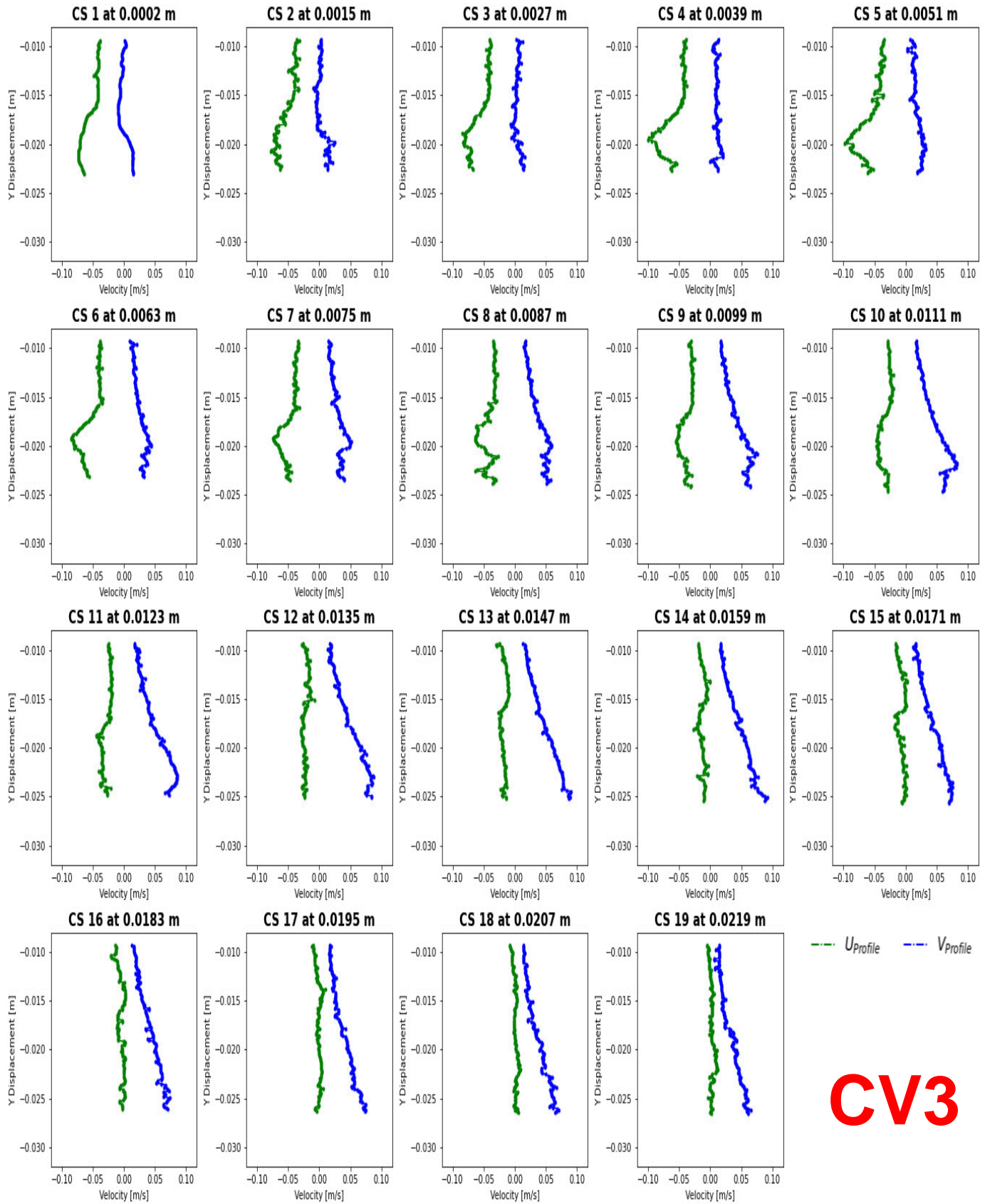
Zhu, Liandong, Zhaohua Li, and Erkki Hiltunen. 2018. 'Microalgae *Chlorella Vulgaris* Biomass Harvesting by Natural Flocculant: Effects on Biomass Sedimentation, Spent Medium Recycling and Lipid Extraction'. *Biotechnology for Biofuels* 11 (1): 183.

APPENDIX A: VELOCITY CROSS-SECTIONS

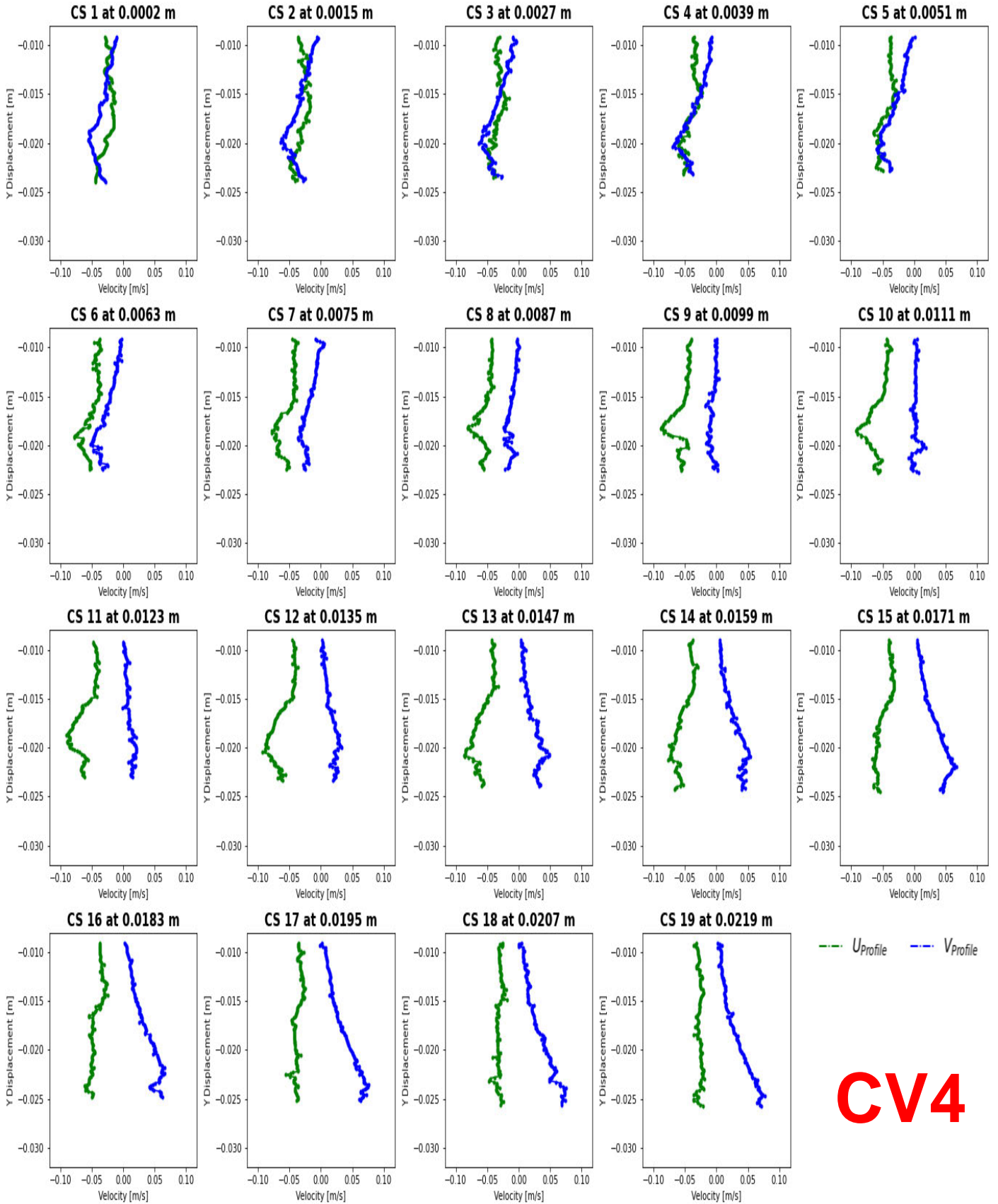


CV1

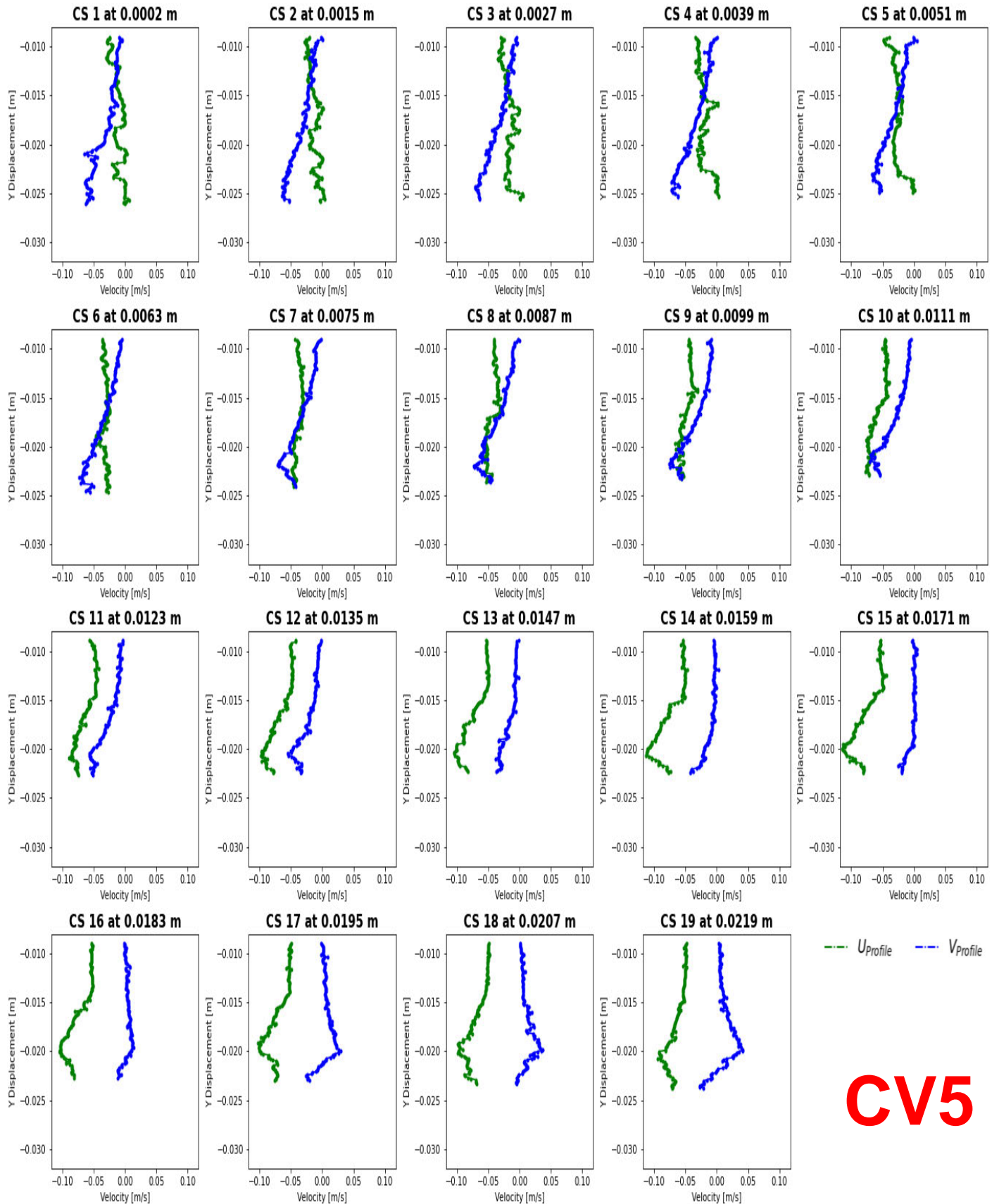




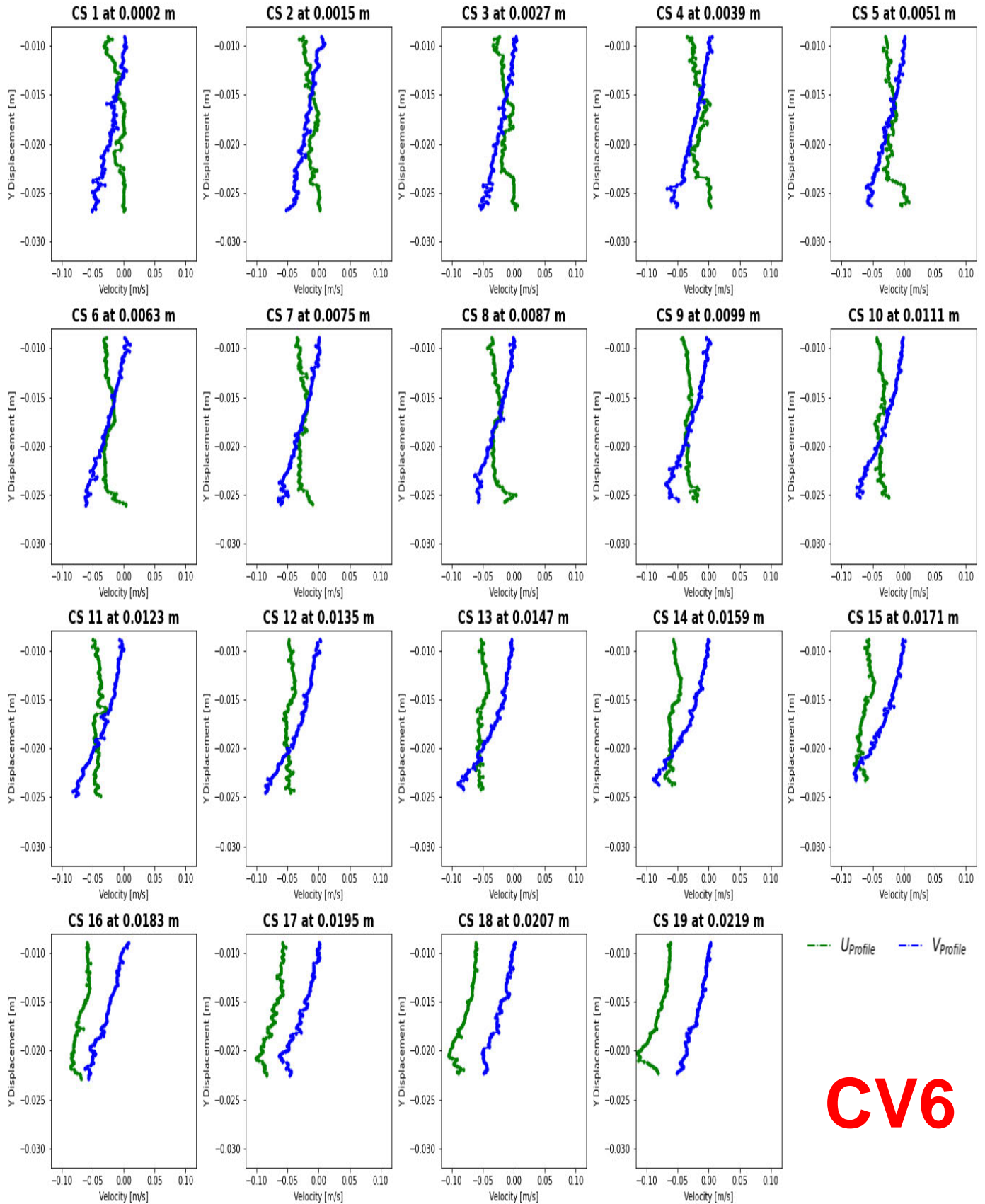
CV3



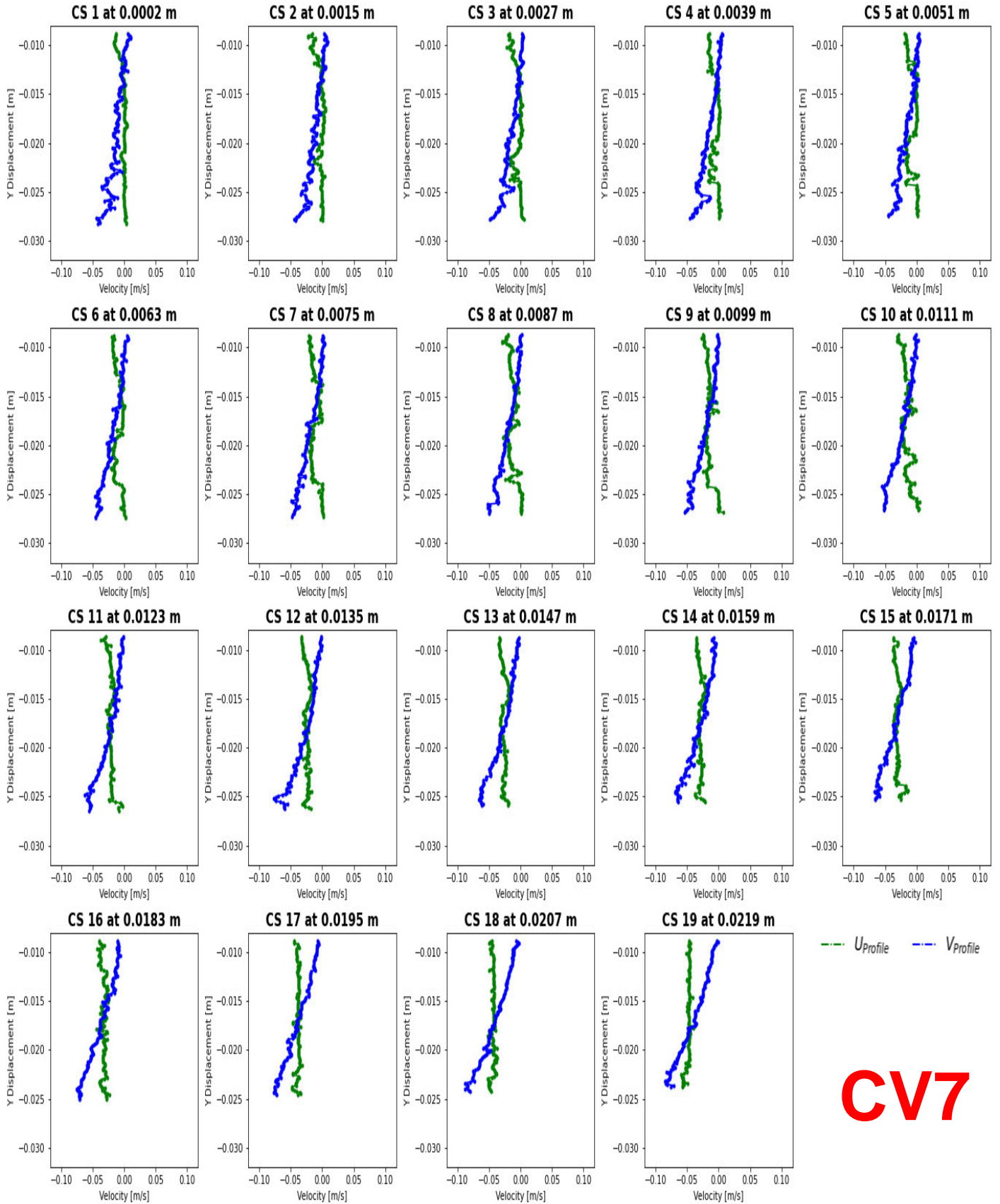
CV4



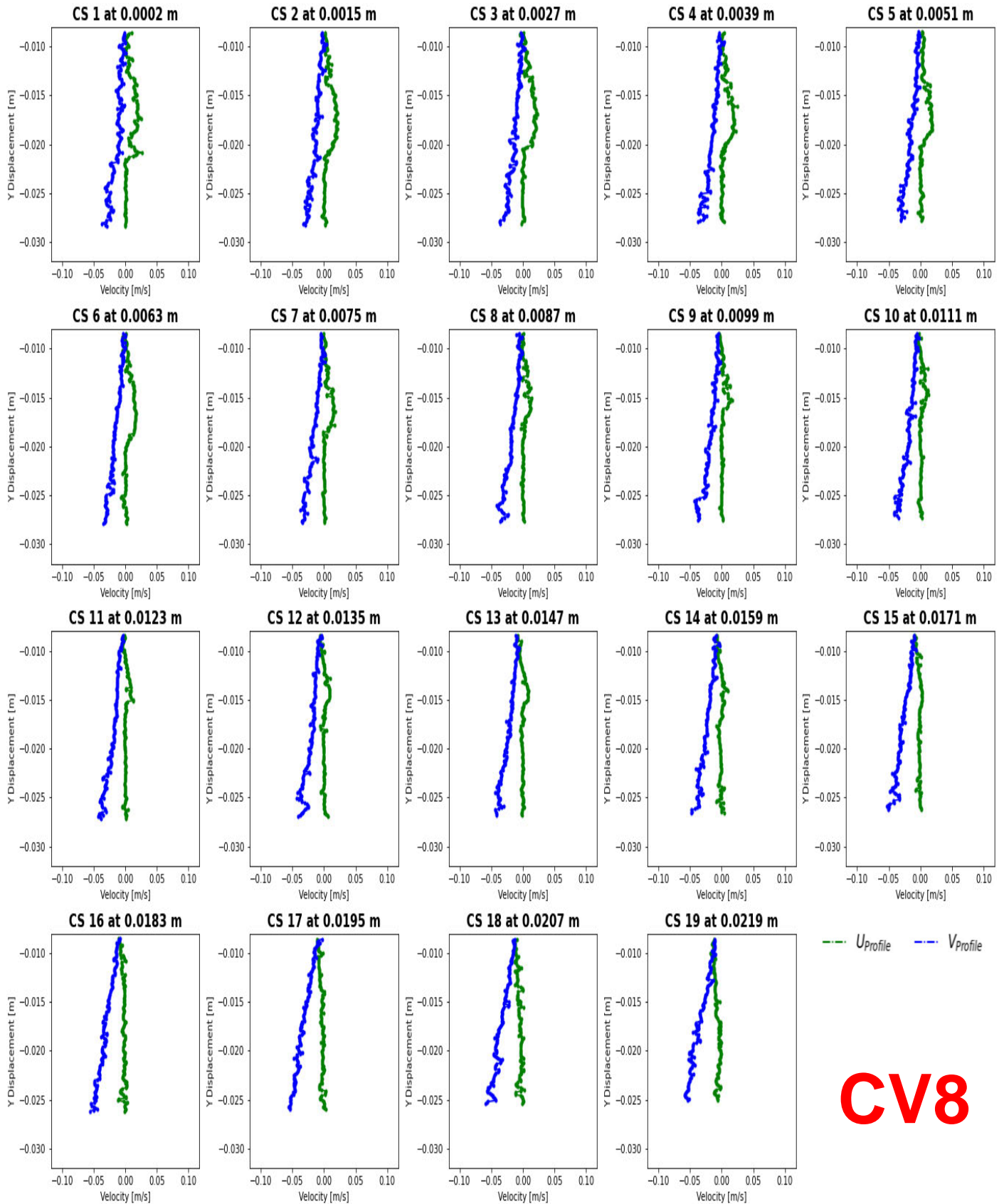
CV5



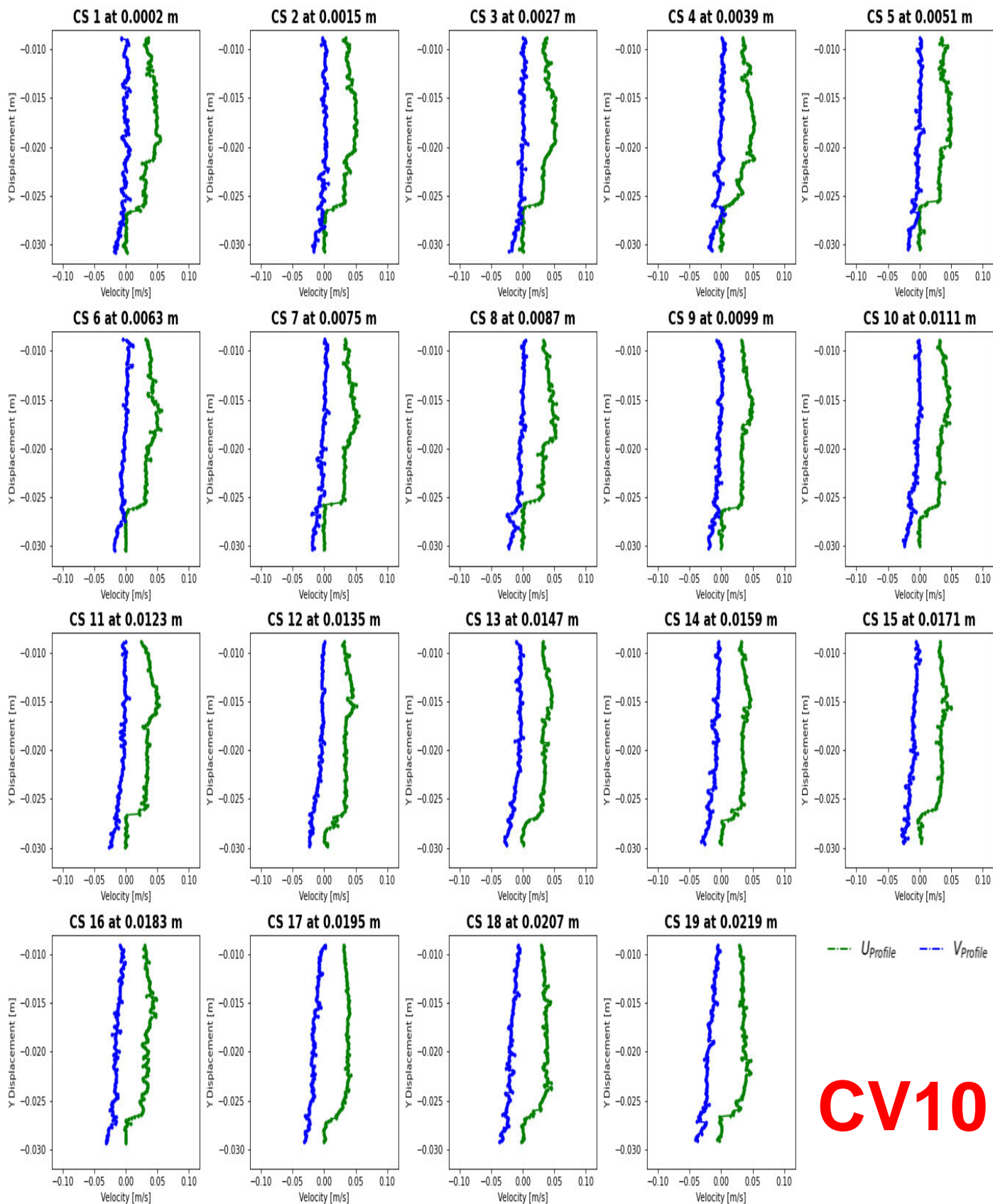
CV6



CV7

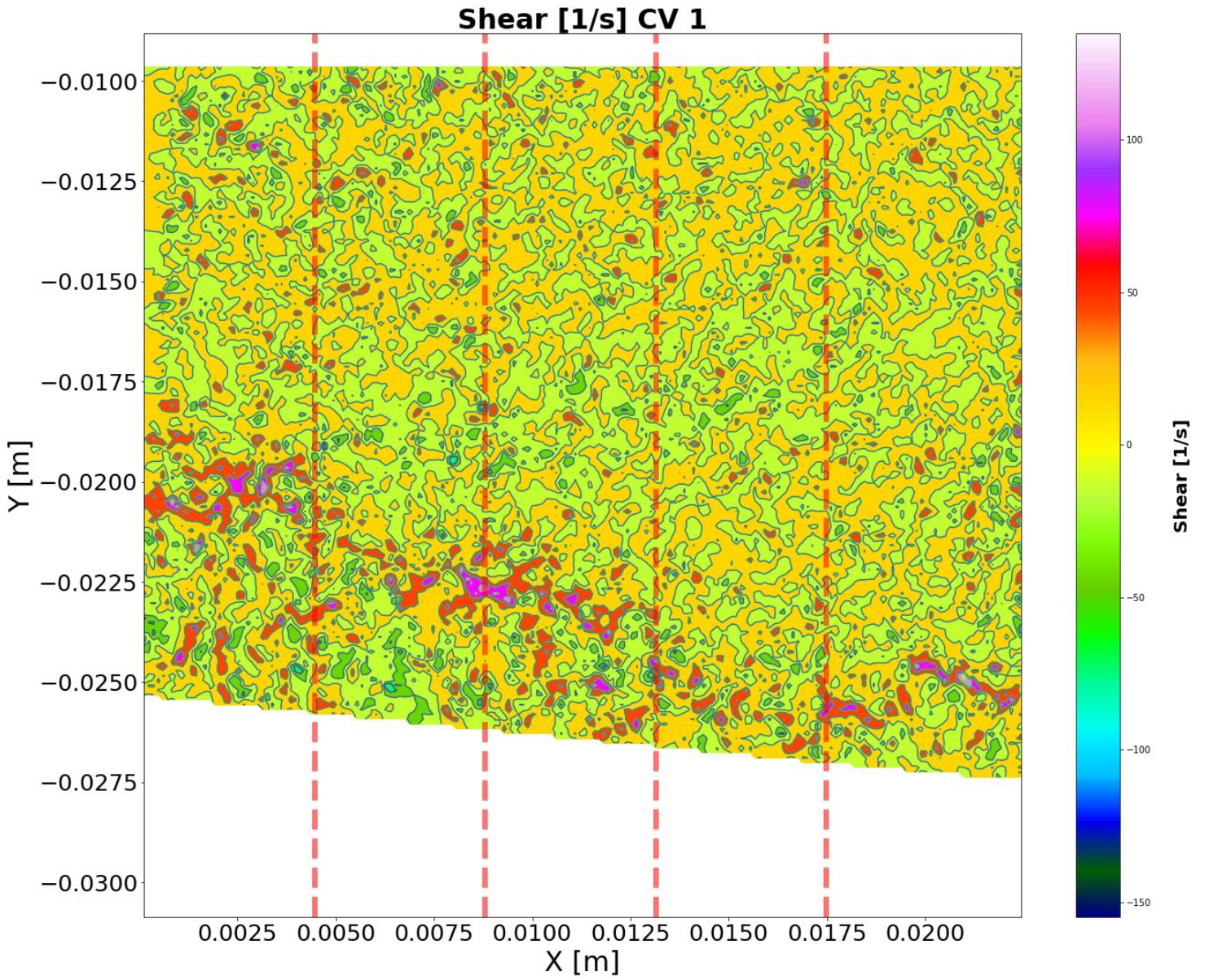


CV8

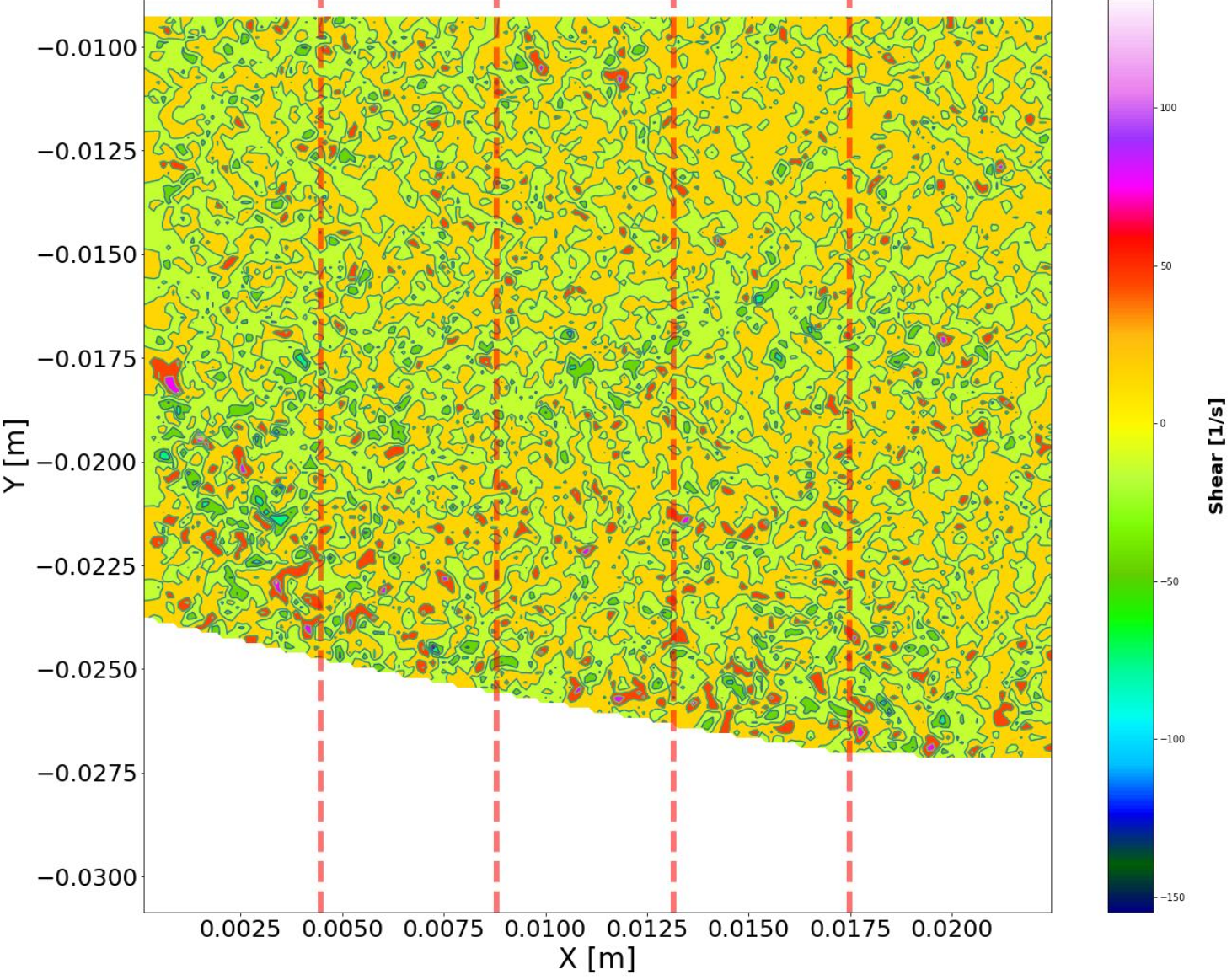


CV10

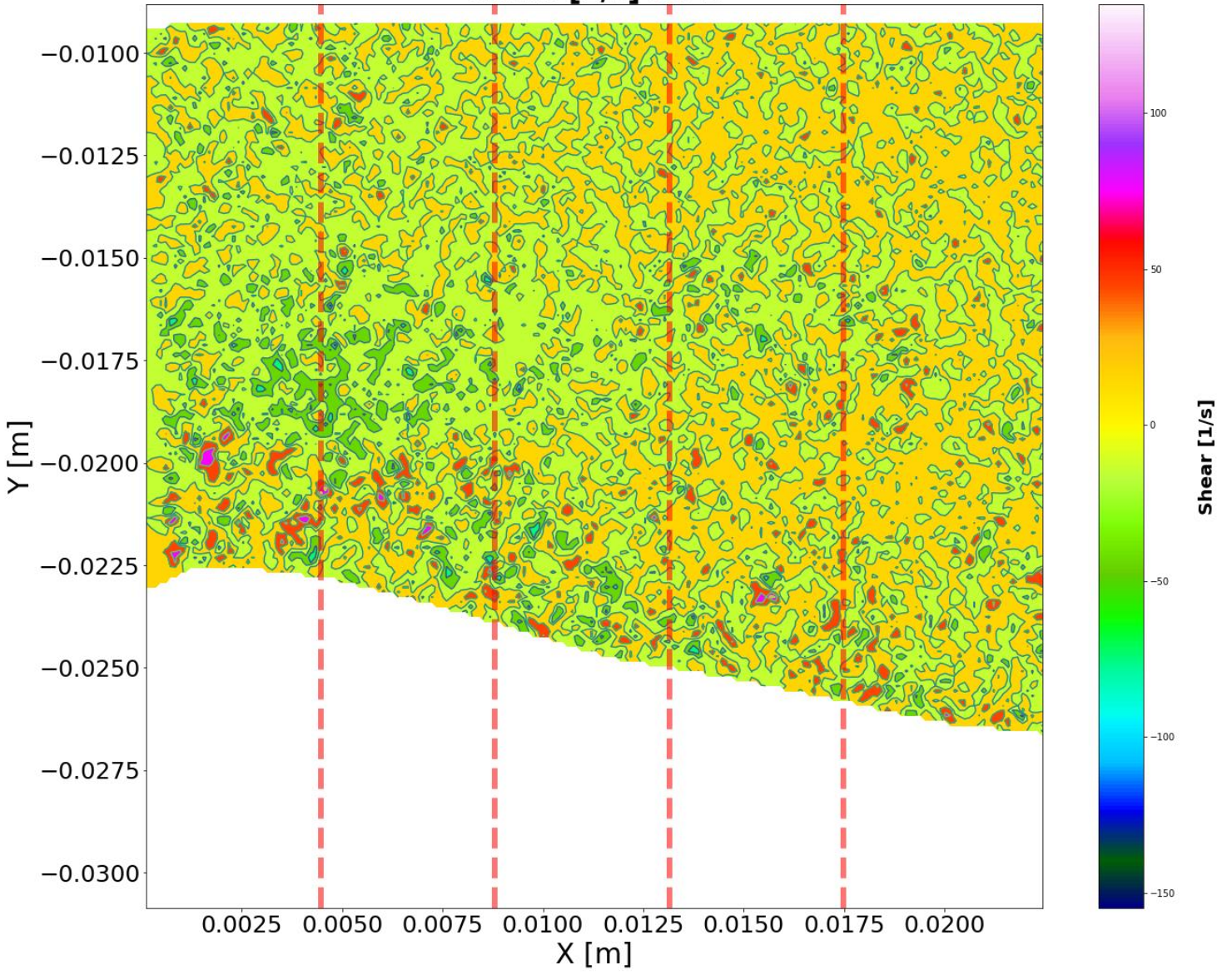
APPENDIX B: SHEAR RATE



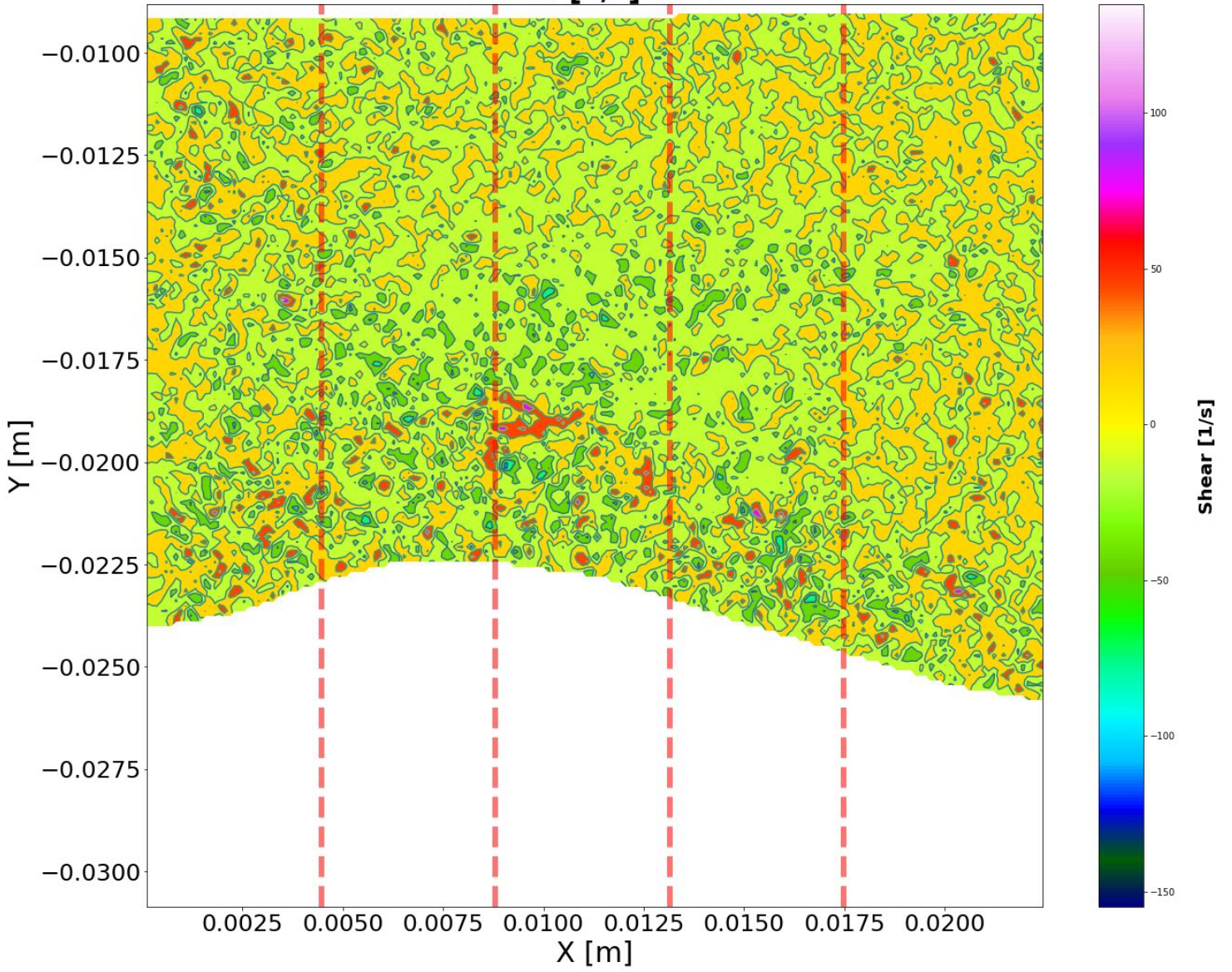
Shear [1/s] CV 2



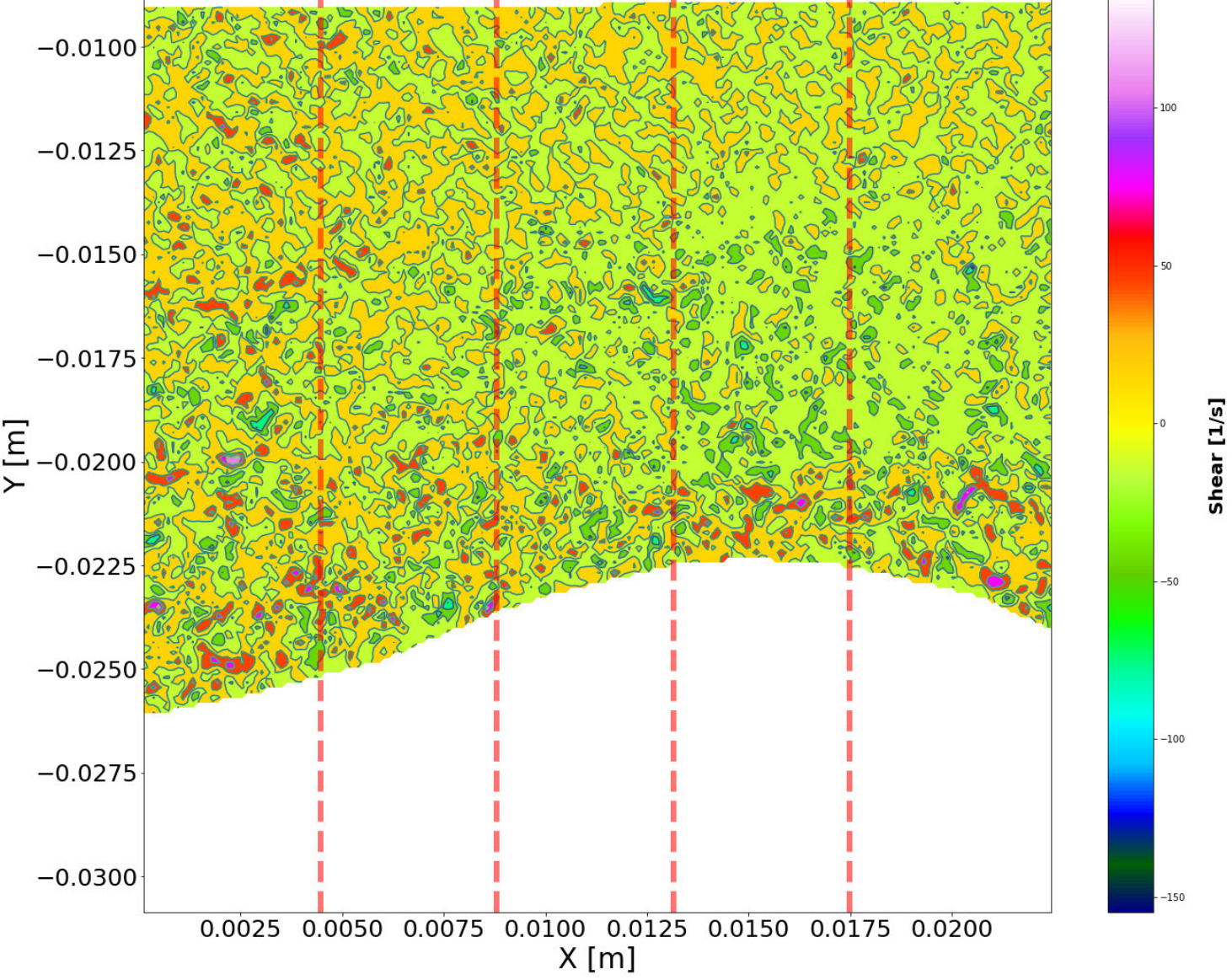
Shear [1/s] CV 3



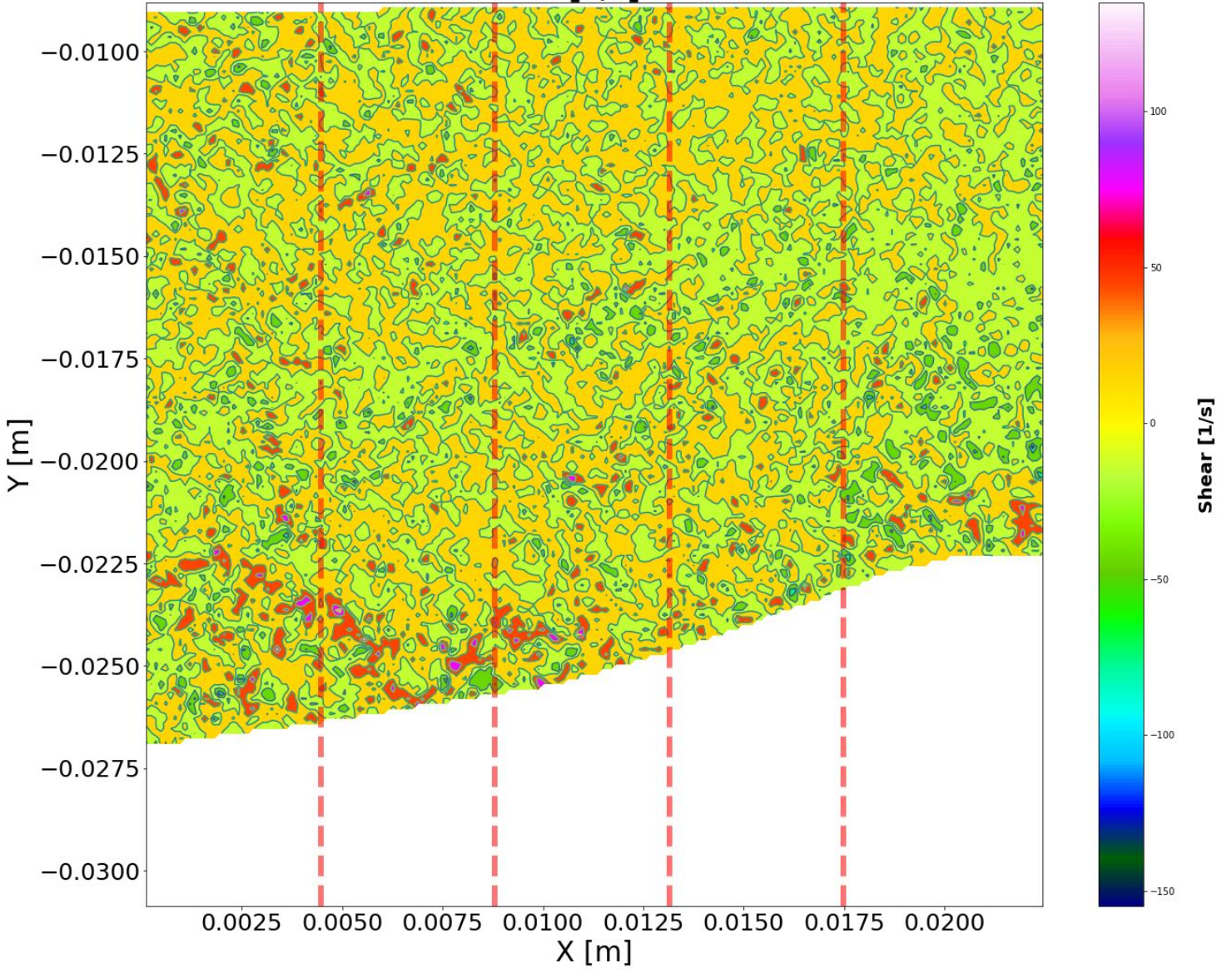
Shear [1/s] CV 4



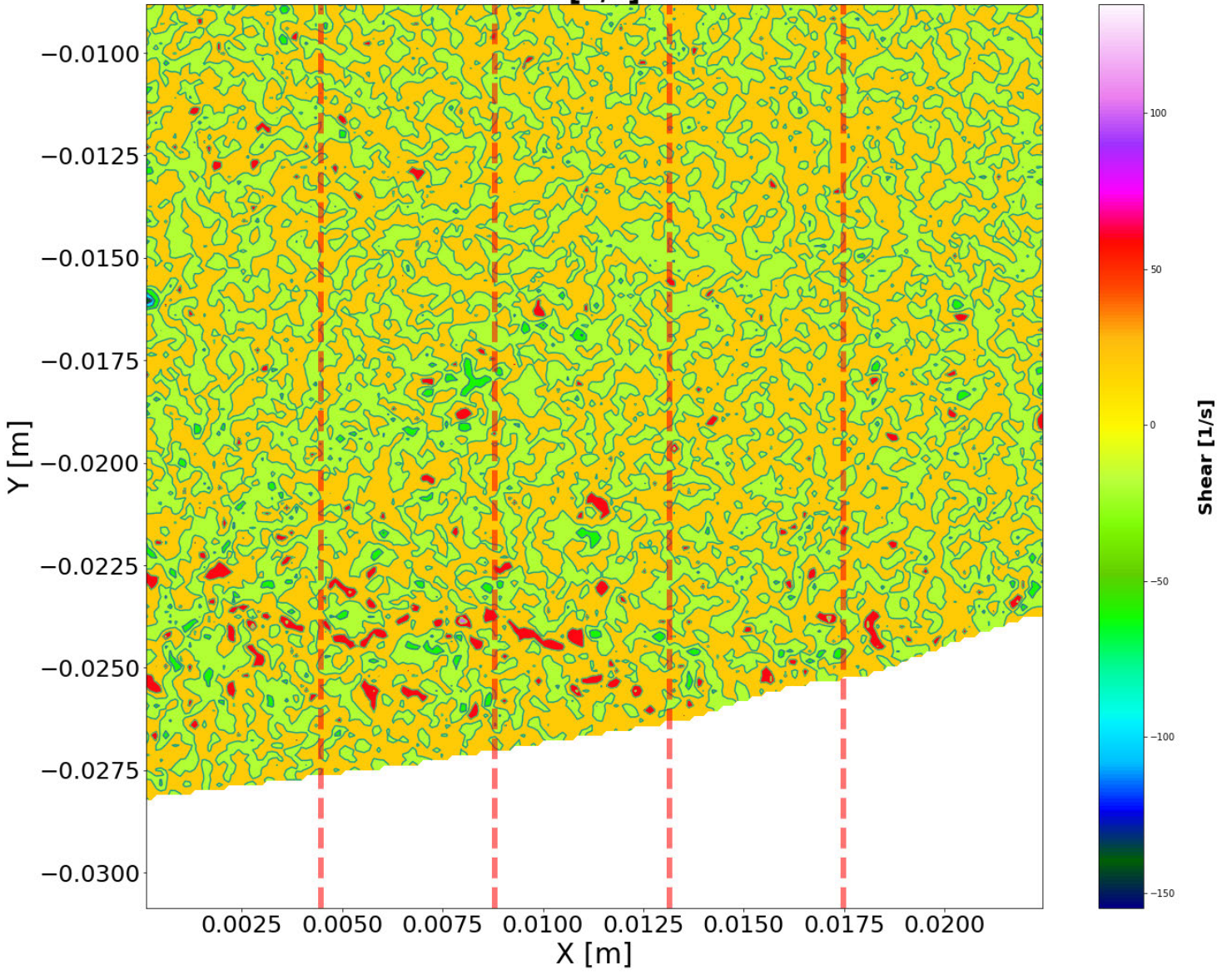
Shear [1/s] CV 5



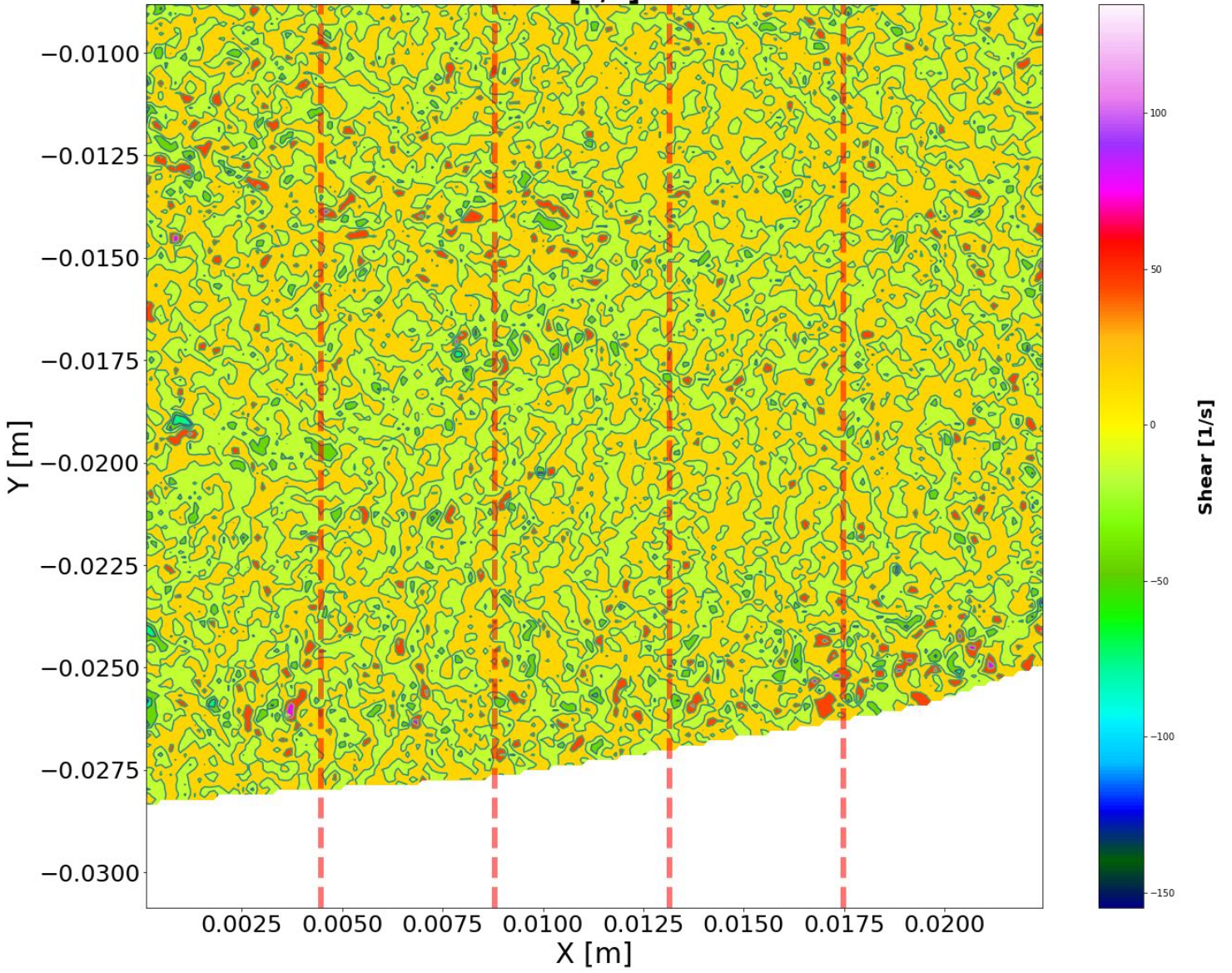
Shear [1/s] CV 6



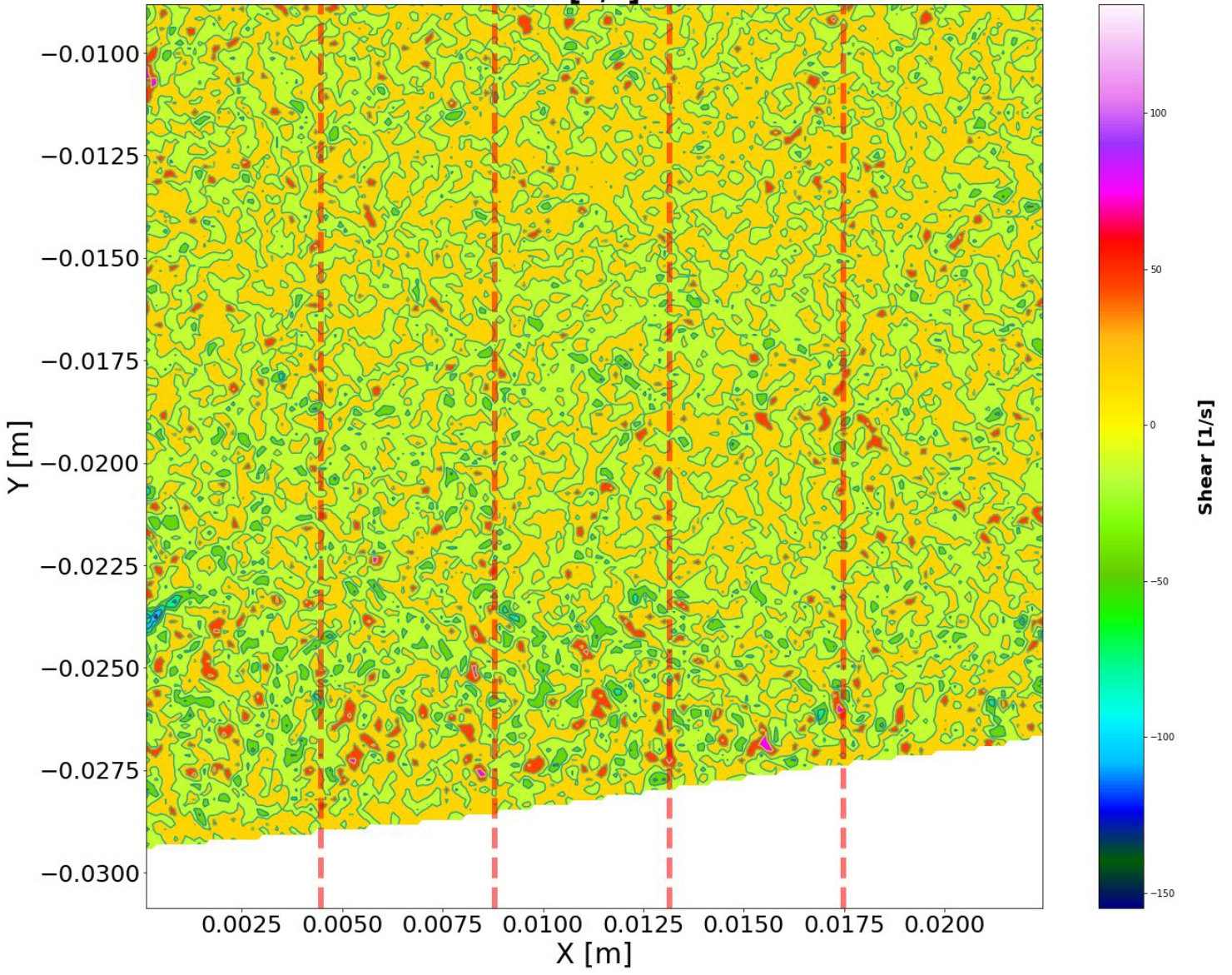
Shear [1/s] CV 7



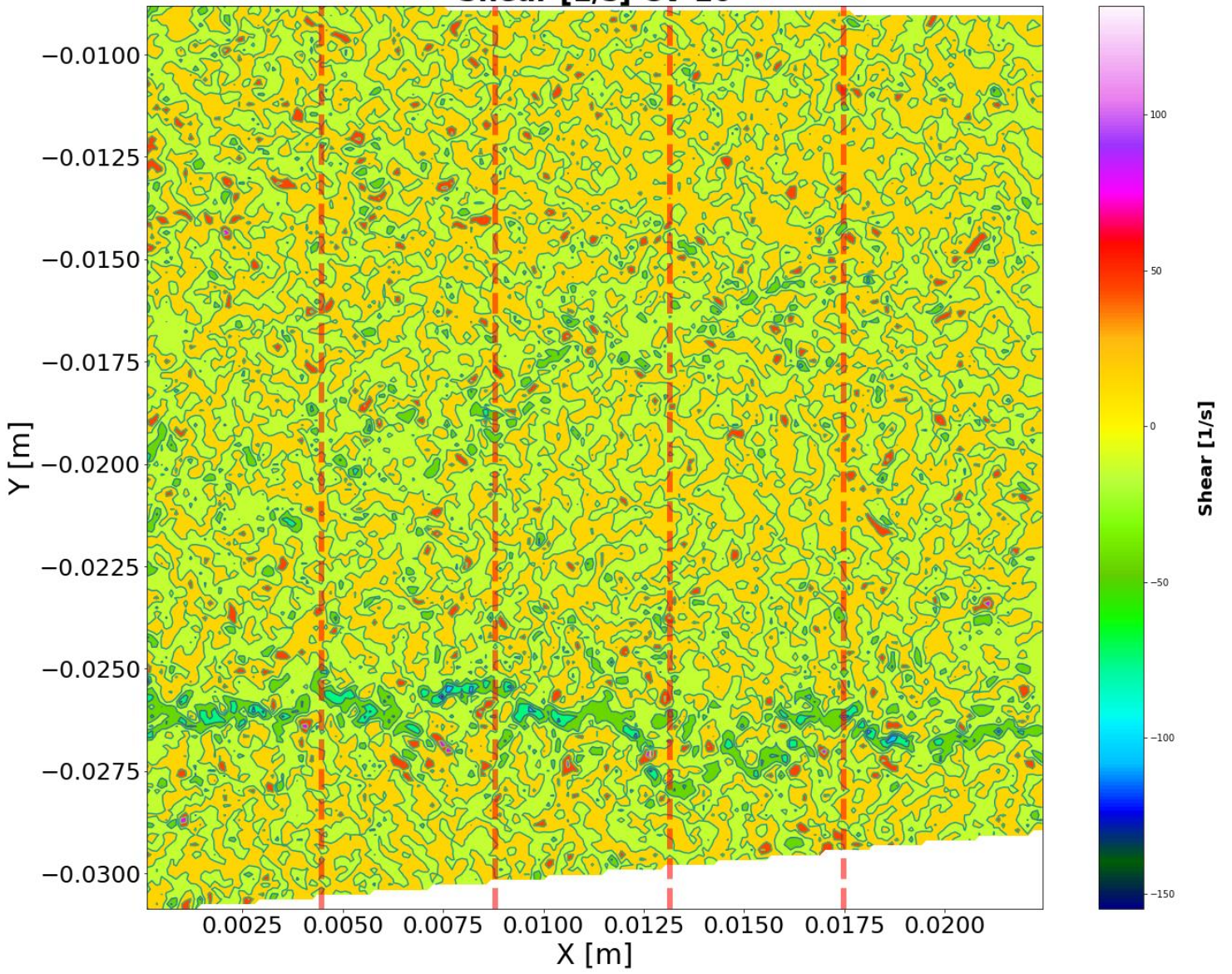
Shear [1/s] CV 8



Shear [1/s] CV 9

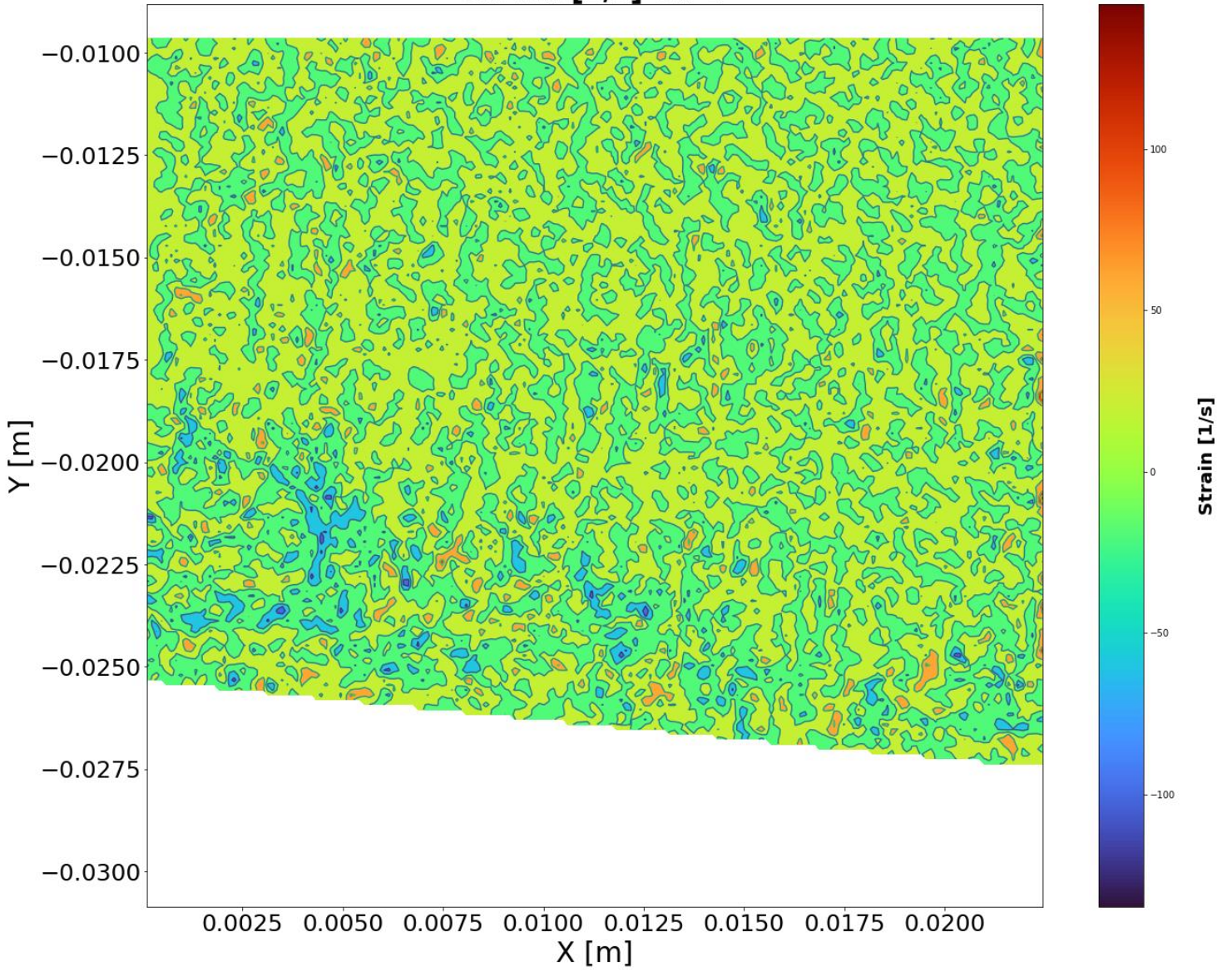


Shear [1/s] CV 10

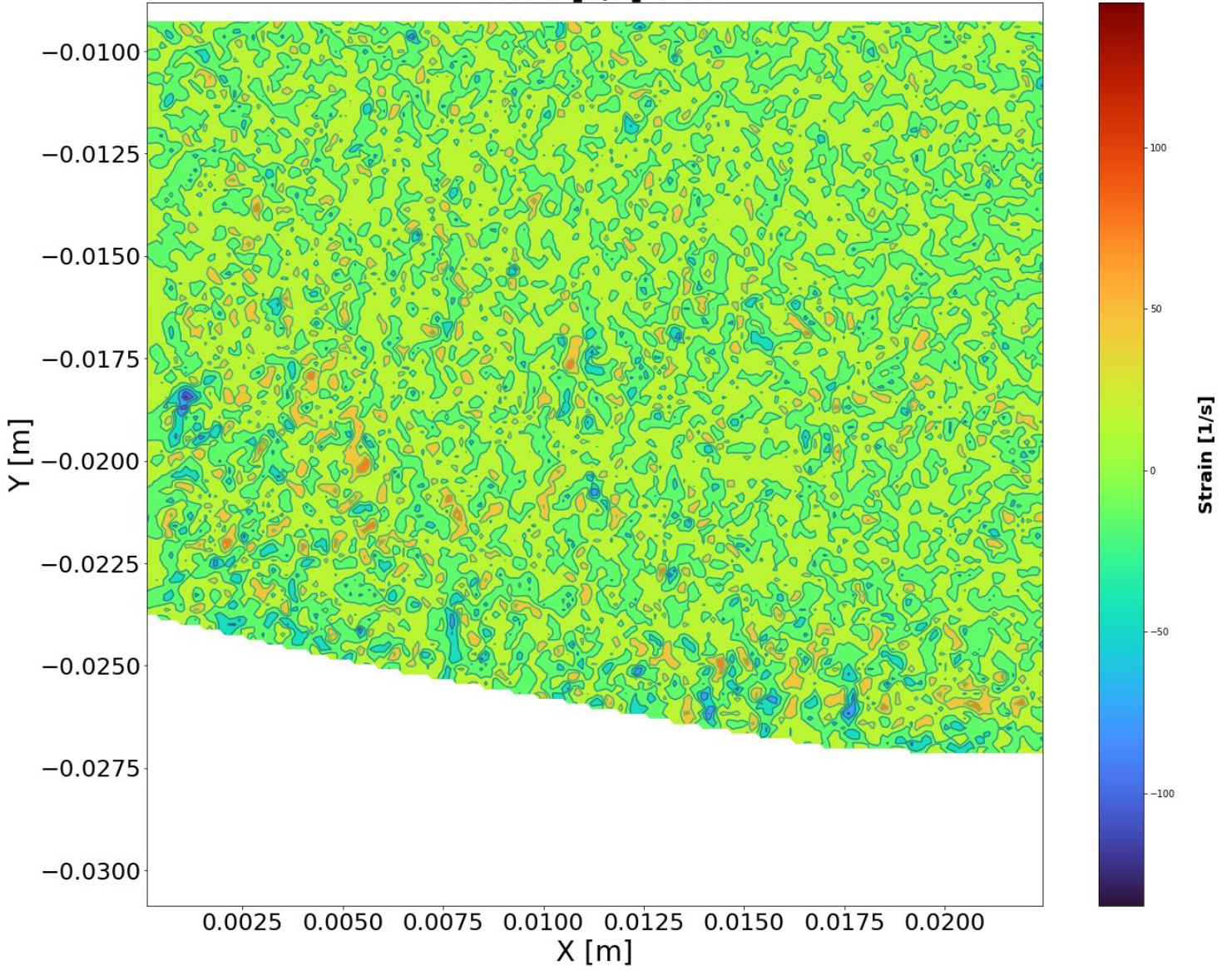


APPENDIX C: STRAIN RATE

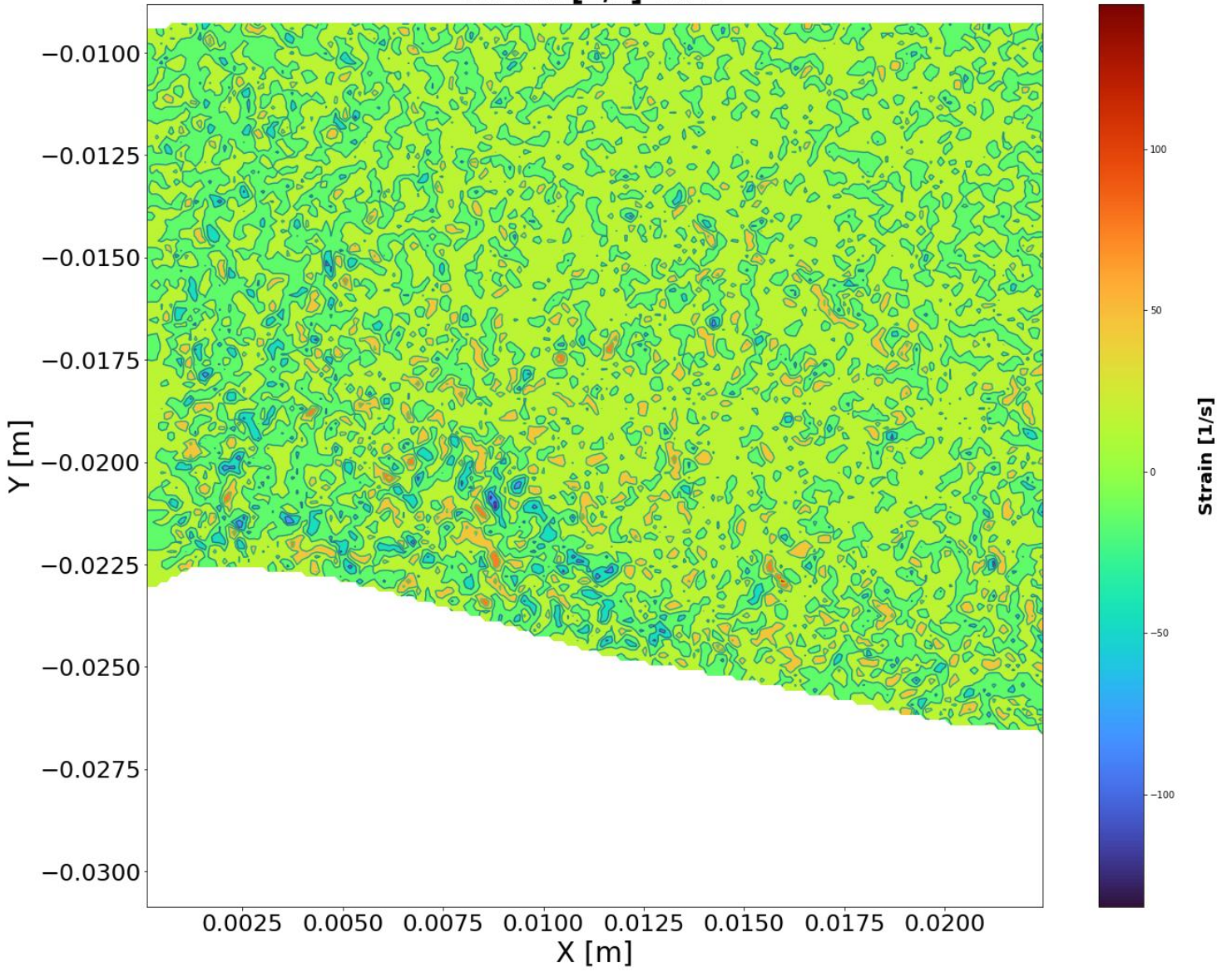
Strain [1/s] CV 1



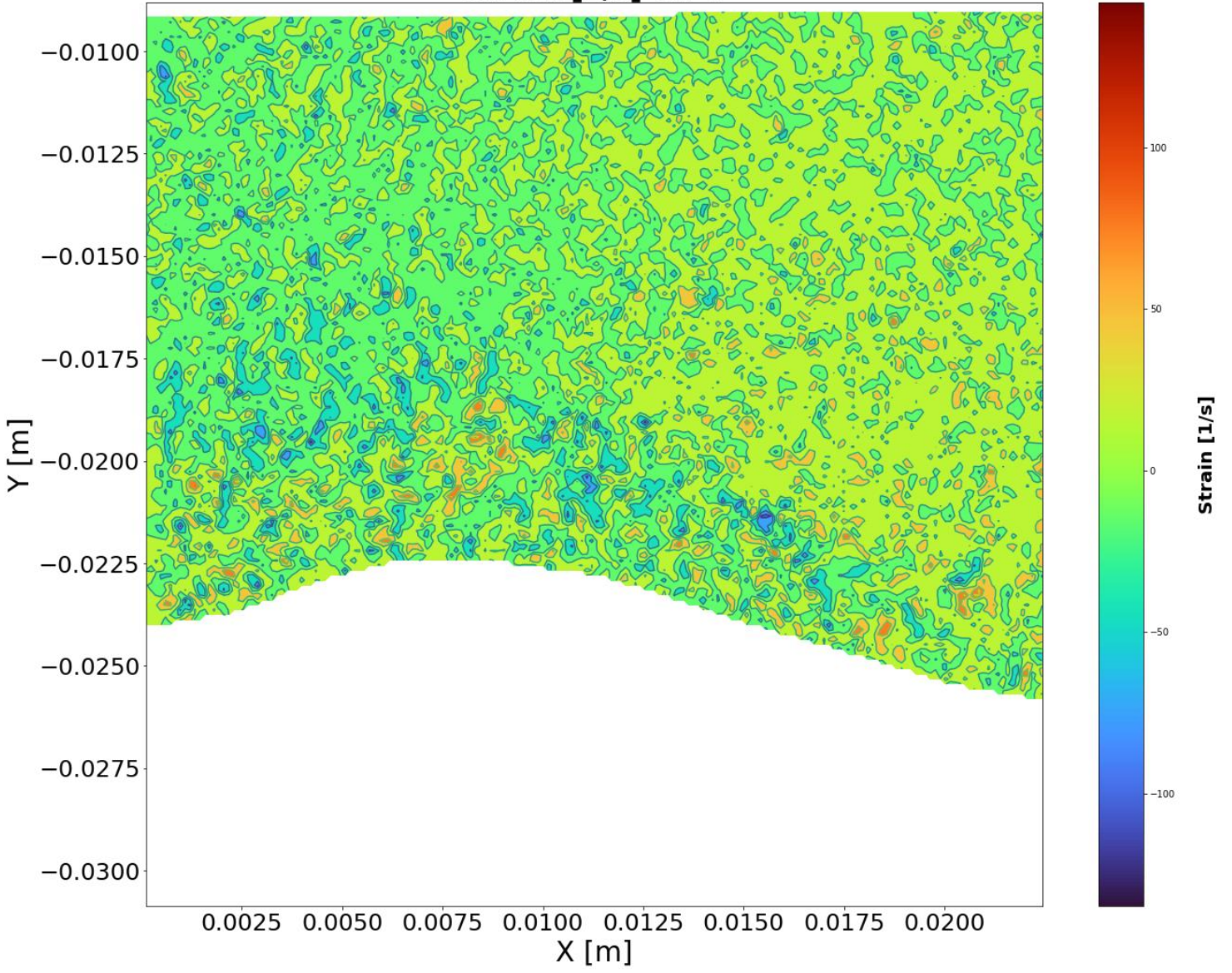
Strain [1/s] CV 2



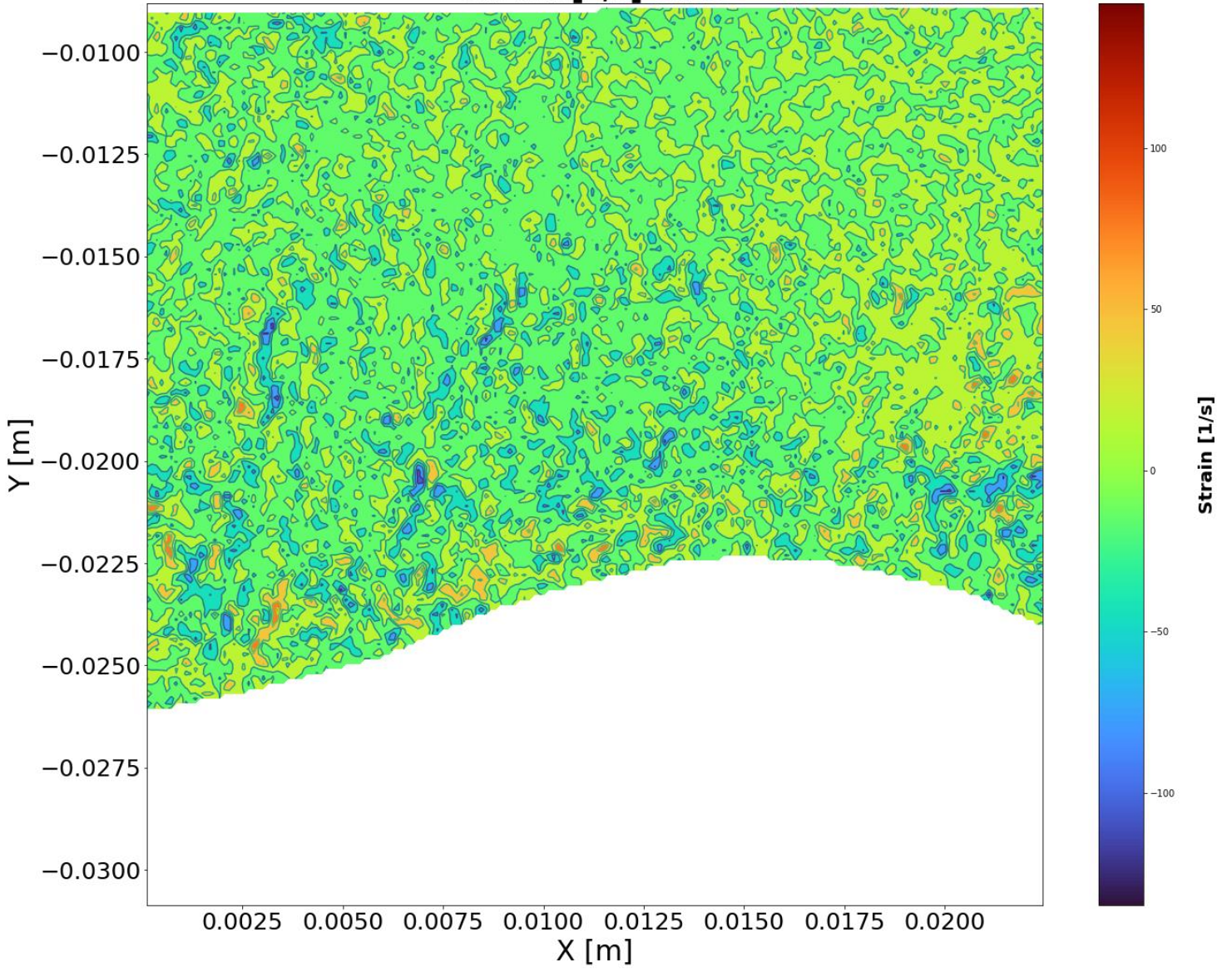
Strain [1/s] CV 3



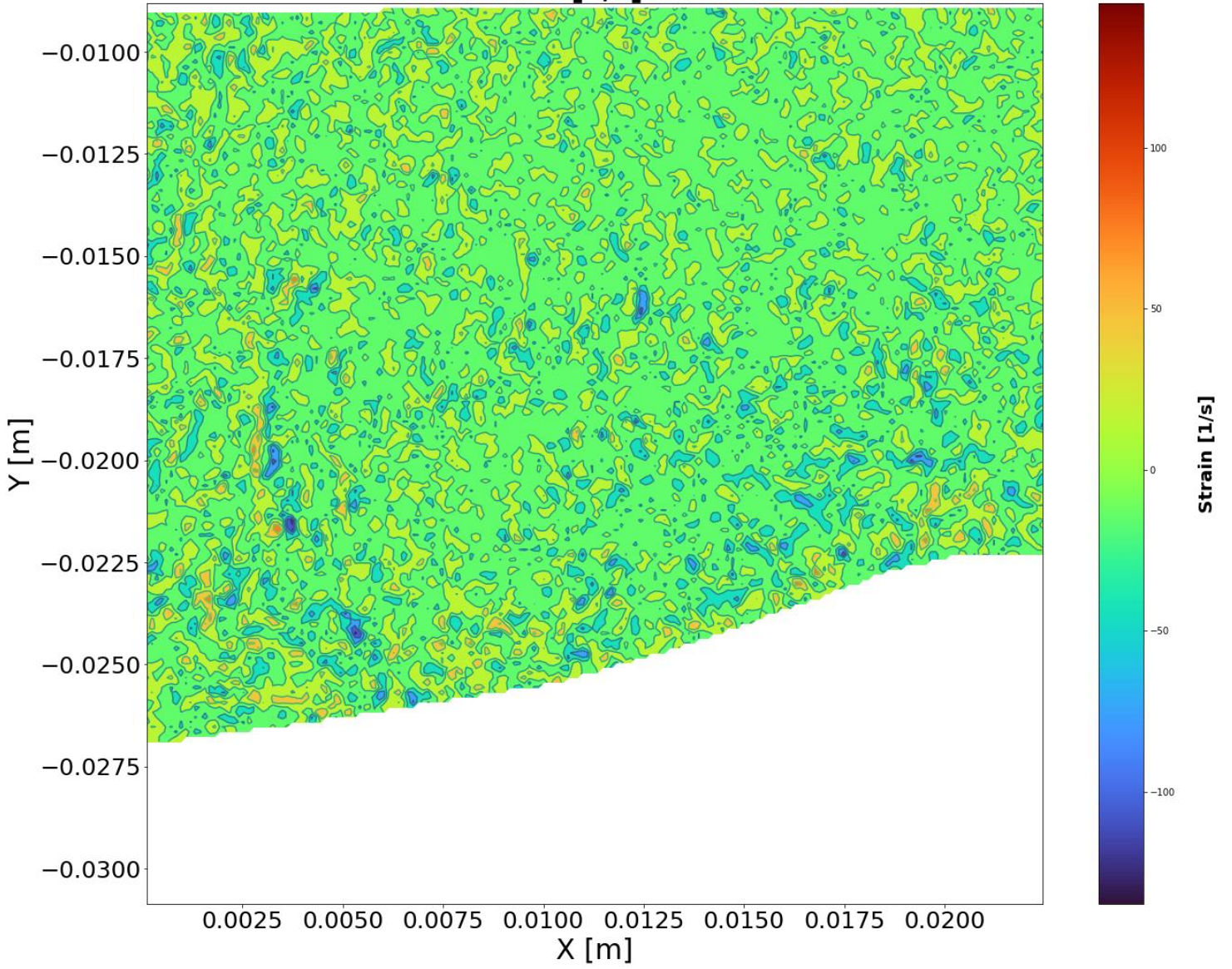
Strain [1/s] CV 4



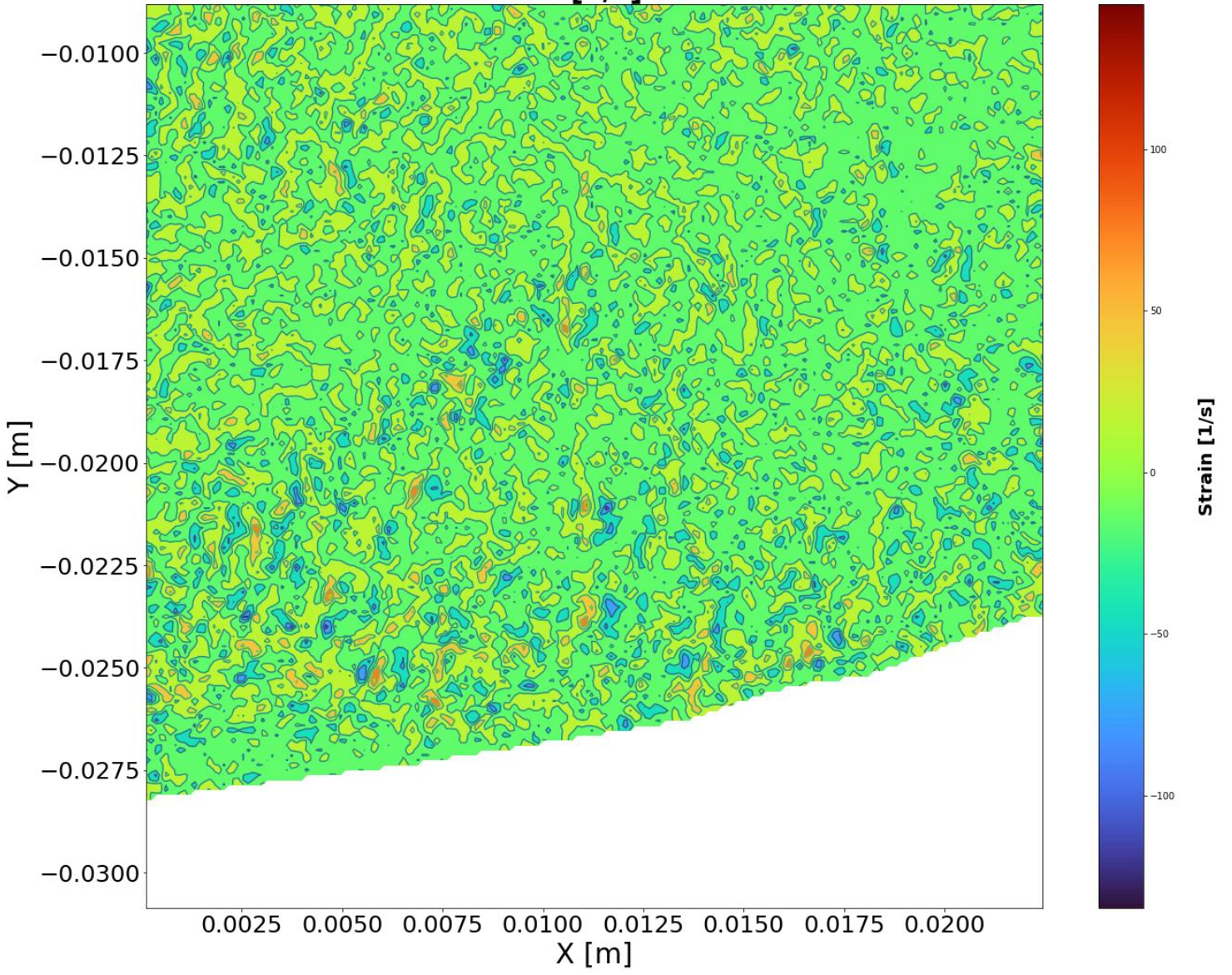
Strain [1/s] CV 5



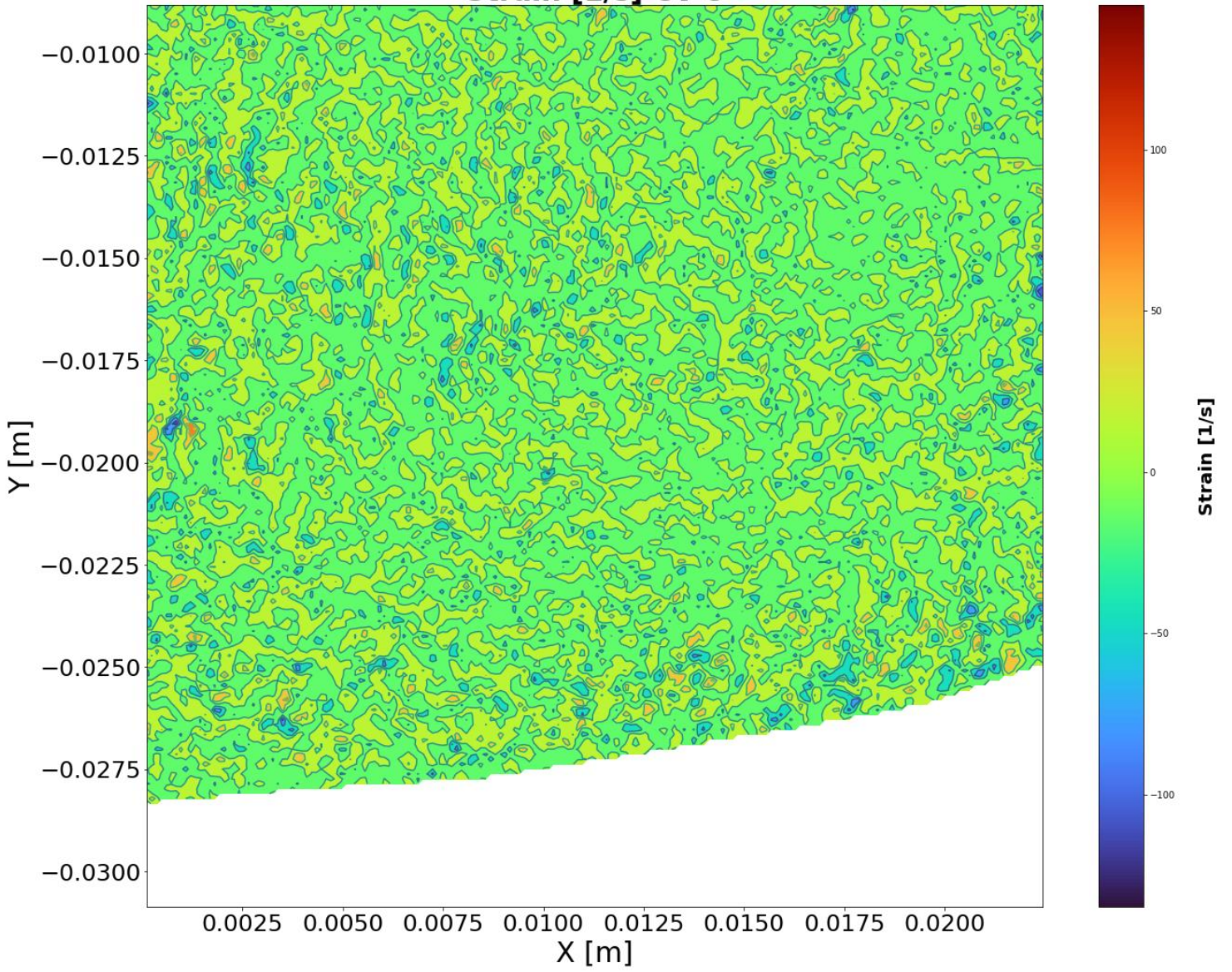
Strain [1/s] CV 6



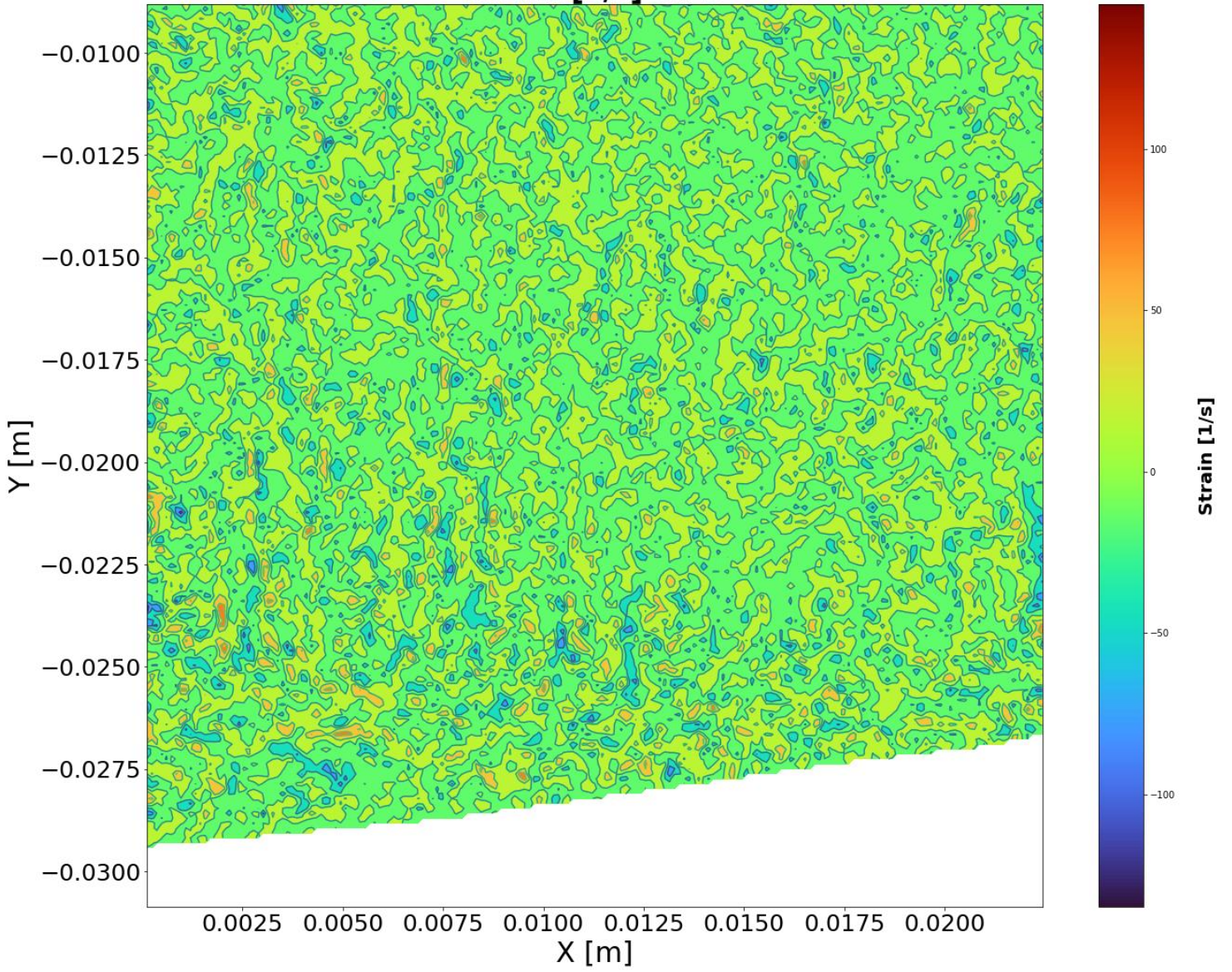
Strain [1/s] CV 7



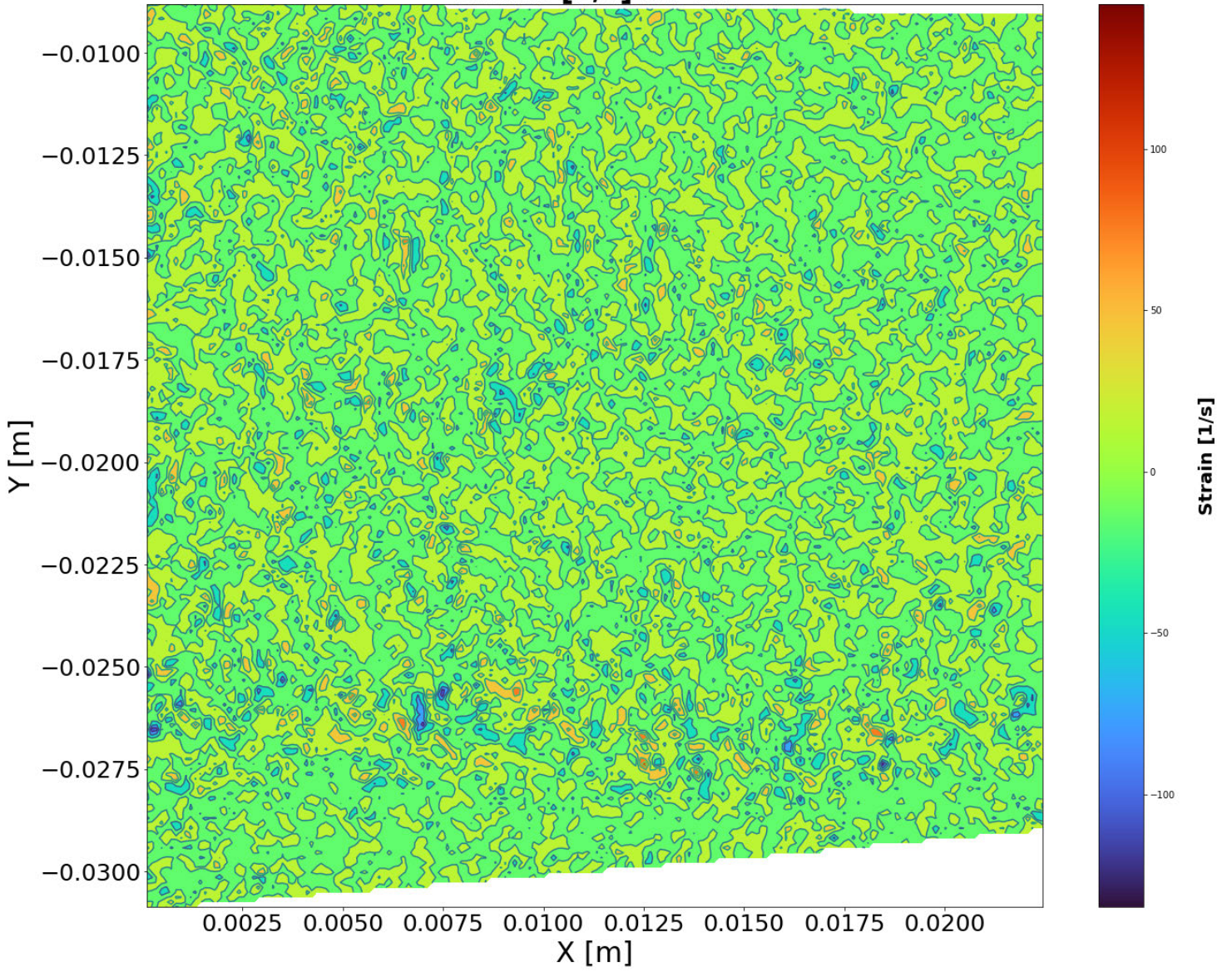
Strain [1/s] CV 8



Strain [1/s] CV 9

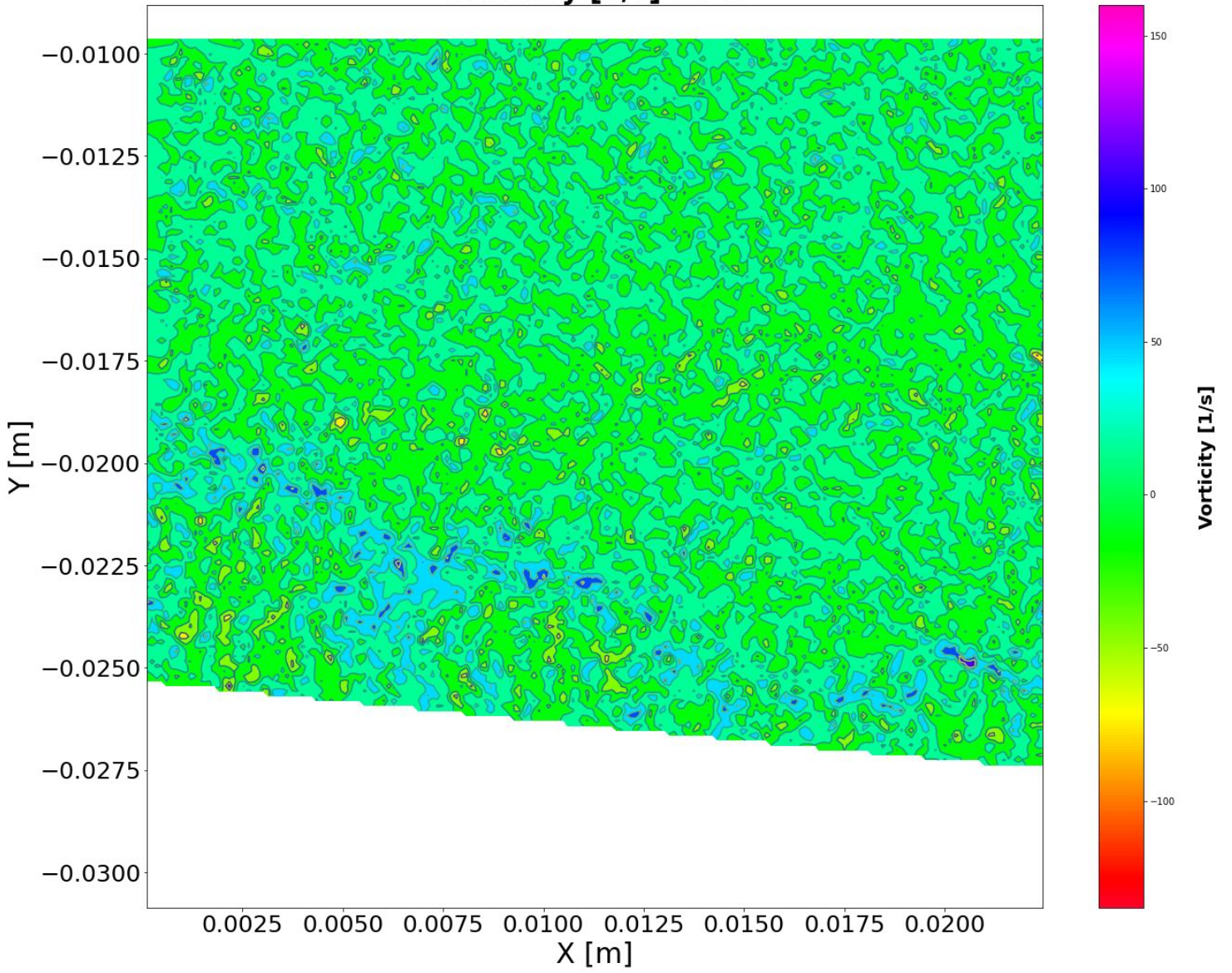


Strain [1/s] CV 10

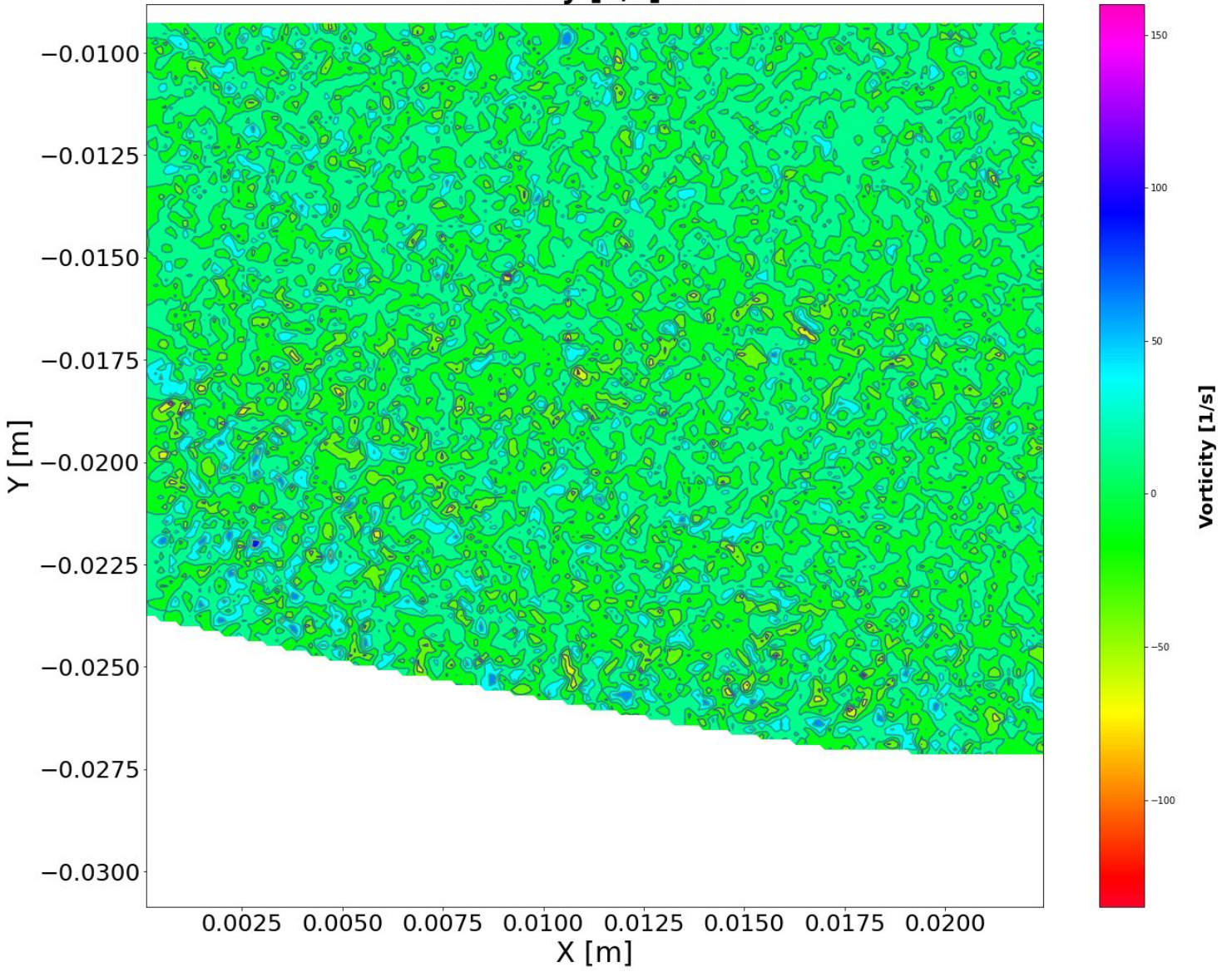


APPENDIX D: VORTICITY

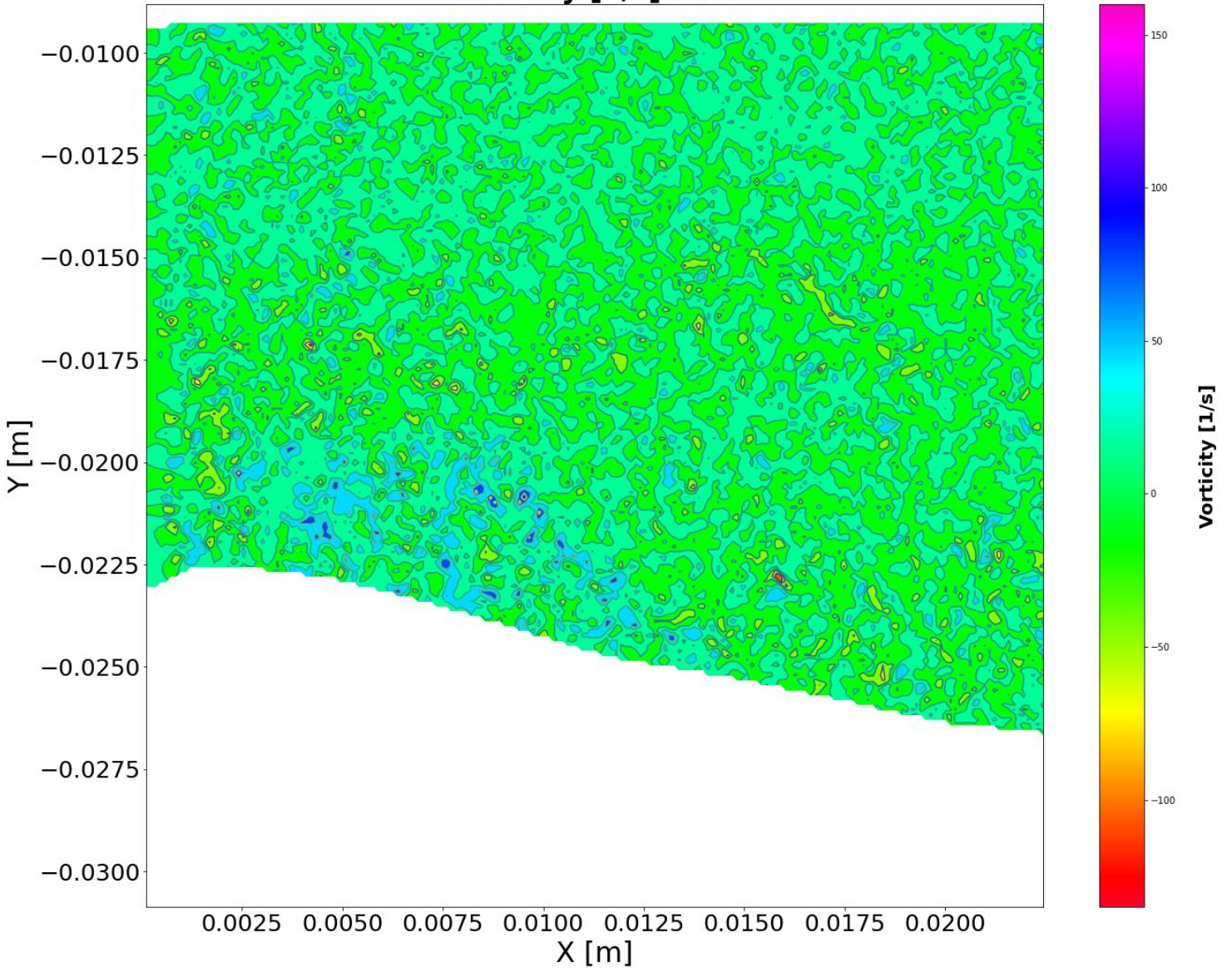
Vorticity [1/s] CV 1



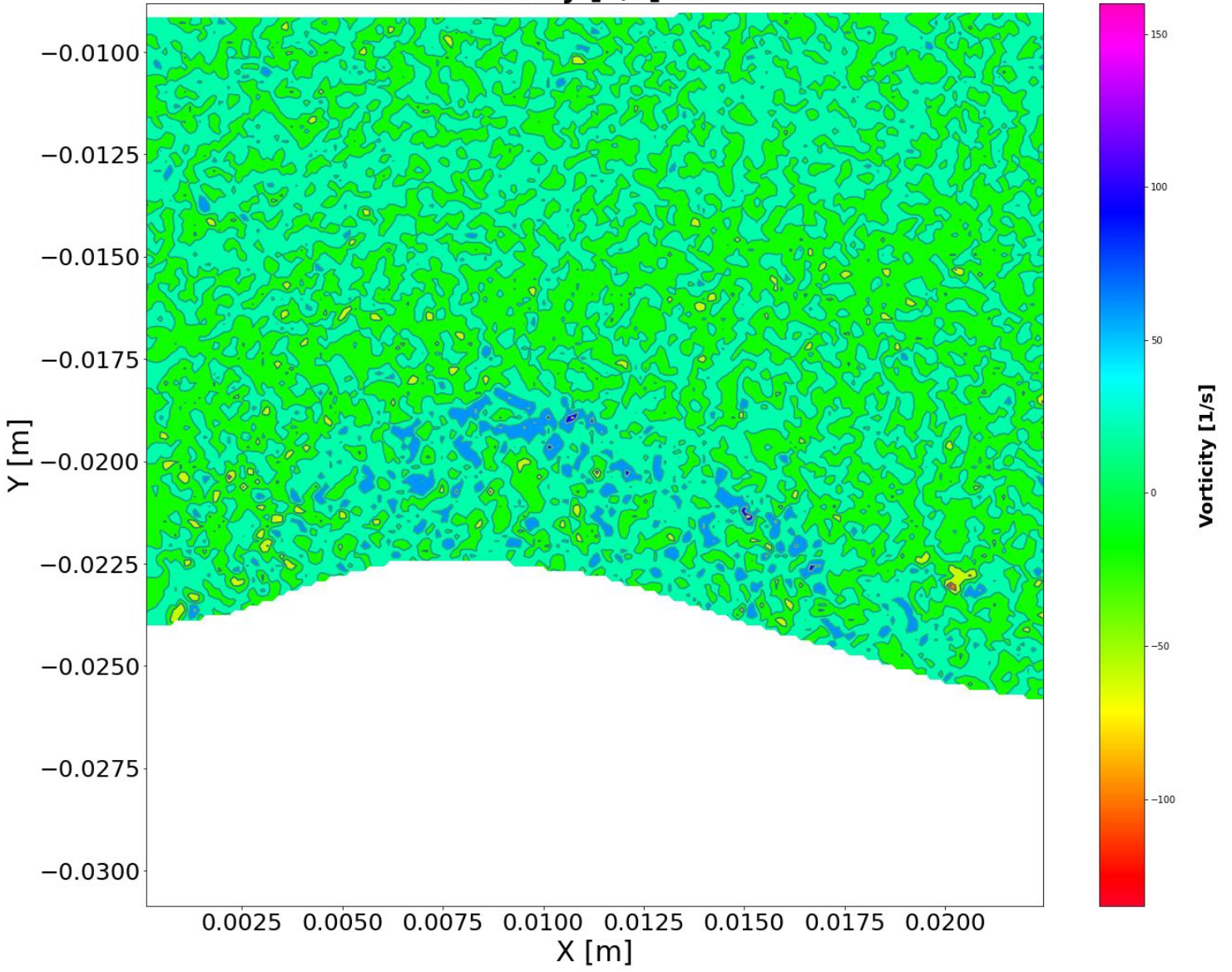
Vorticity [1/s] CV 2



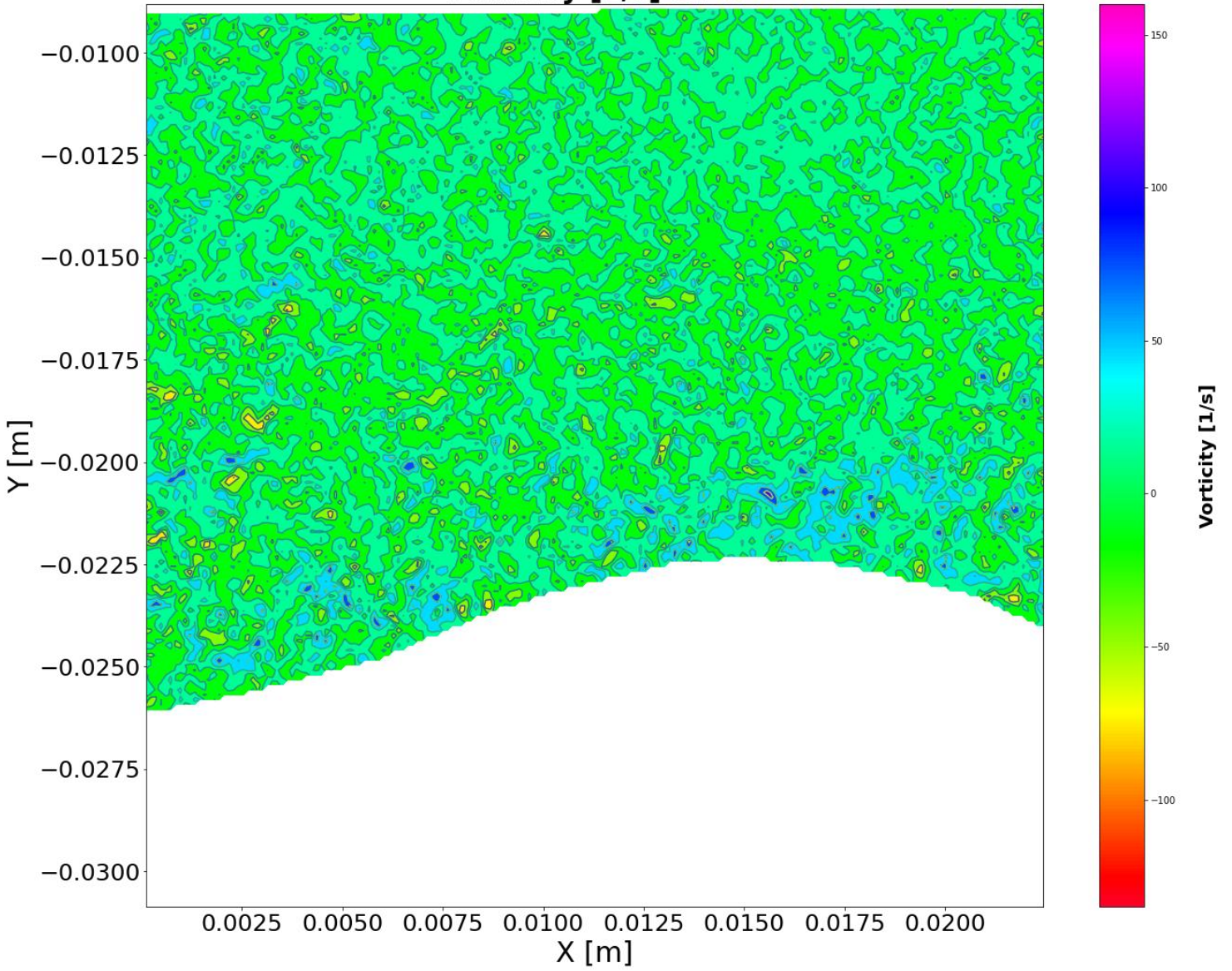
Vorticity [1/s] CV 3



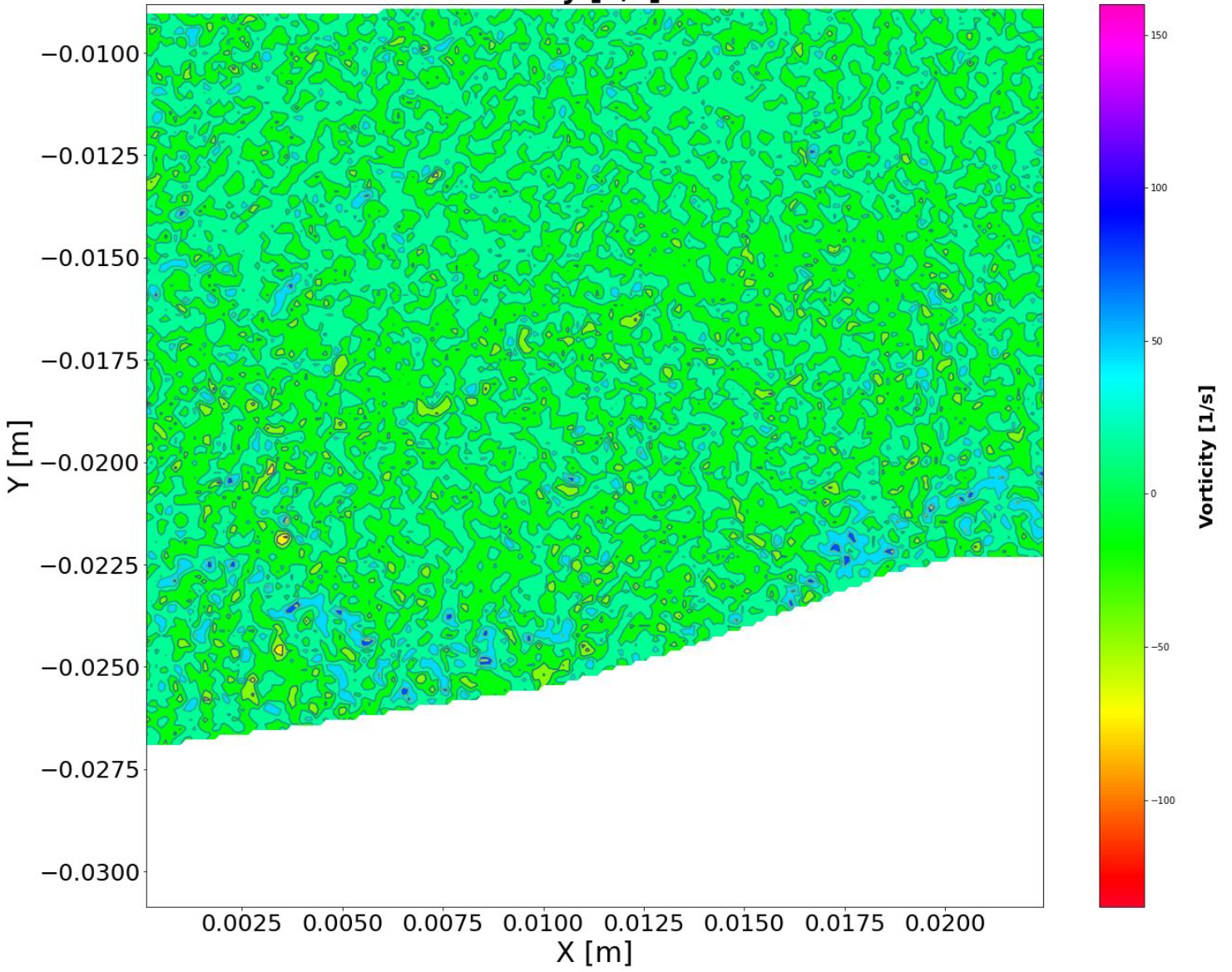
Vorticity [1/s] CV 4



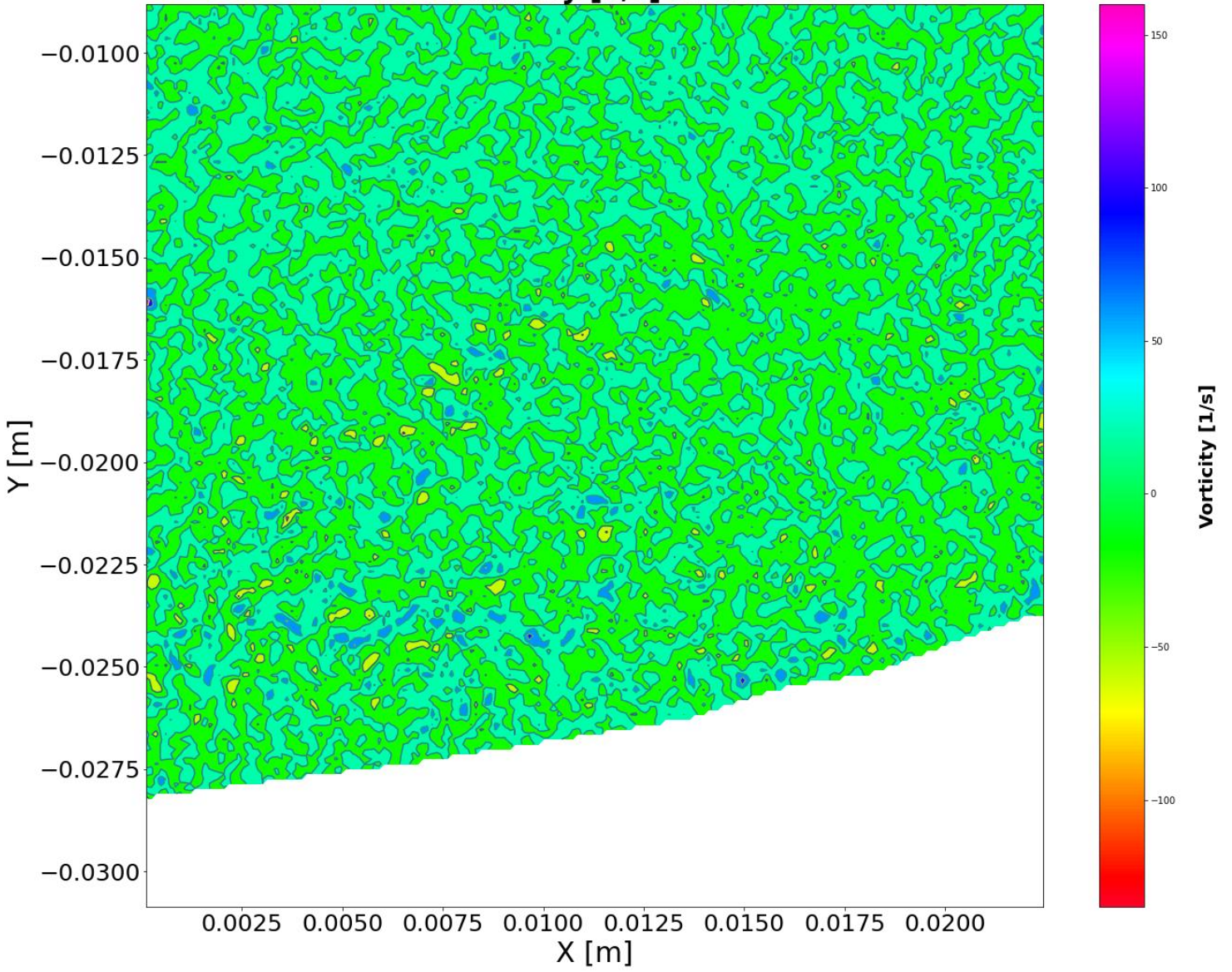
Vorticity [1/s] CV 5



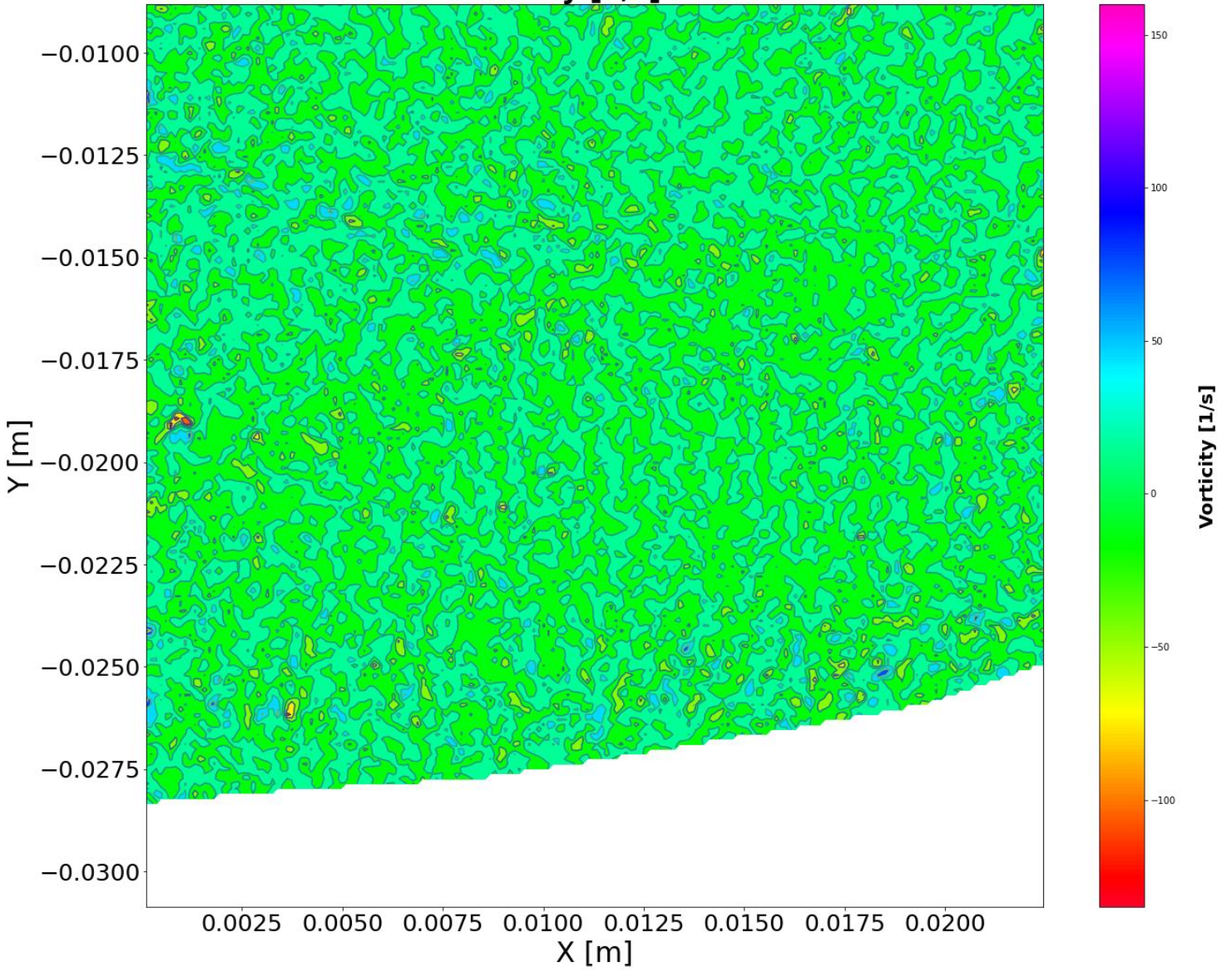
Vorticity [1/s] CV 6



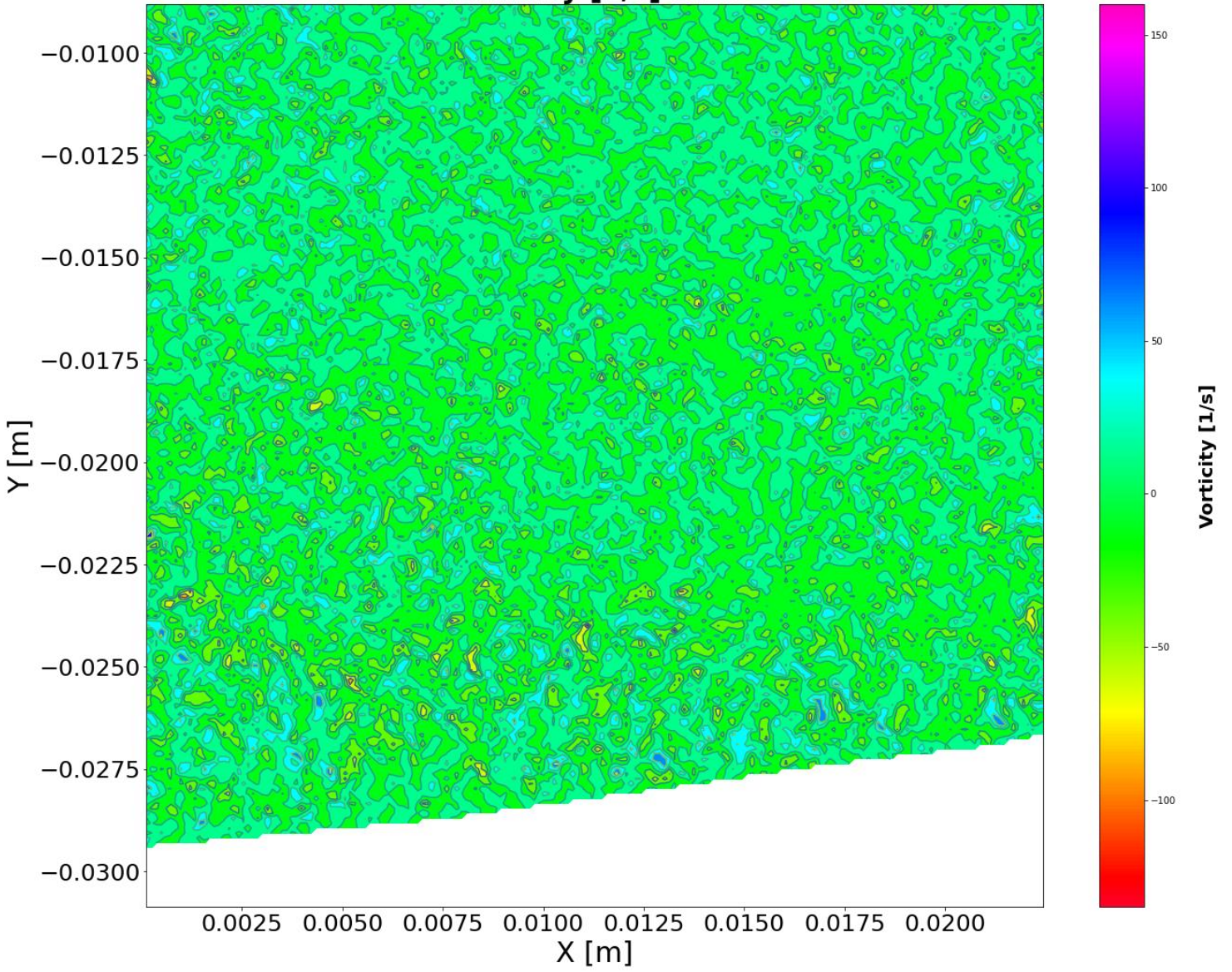
Vorticity [1/s] CV 7



Vorticity [1/s] CV 8



Vorticity [1/s] CV 9



Vorticity [1/s] CV 10

